Low Complexity Hybrid Precoding and Combining for Millimeter Wave Systems

Mohamed Alouzi

Thesis submitted to the University of Ottawa
in Partial Fulfillment of the requirements for the
Doctor of Philosophy

School of Electrical Engineering and Computer Science
Faculty of Engineering
University of Ottawa

ABSTRACT

The evolution to 5G and its use cases is driven by data-intensive applications requiring higher data rates over wireless channels. This has led to research in massive multiple input multiple output (MIMO) techniques and the use of the millimeter wave (mm wave) band. Because of the higher path loss at mm wave frequencies and the poor scattering nature of the mm wave channel (fewer paths exist), this thesis first proposes the use of the sphere decoding (SD) algorithm, and the semidefinite relaxation (SDR) detector to improve the performance of a uniform planar array (UPA) hybrid beamforming technique with large antenna arrays. The second contributions of this thesis consist of a low-complexity algorithm using the gradient descent for hybrid precoding and combining designs in mm wave systems. Also, in this thesis we present a low-complexity algorithm for hybrid precoding and combining designs that uses momentum gradient descent and Newton's Method for mm wave systems which makes the objective function converge faster compared to other iterative methods in the literature; the two proposed low-complexity algorithms for hybrid precoding and combining do not depend on the antenna array geometry, unlike the orthogonal matching pursuit (OMP) hybrid precoding/combining approach. Moreover, these algorithms allow hybrid precoders/combiners to yield a performance very close to that of the optimal unconstrained digital precoders and combiners with a small number of iterations. Simulation results verify that the proposed hybrid precoding/combining scheme that uses momentum gradient descent and Newton's Method outperforms previous methods that appear in the literature in terms of bit error rate (BER) and achievable spectral efficiency with lower complexity. Finally, an iterative algorithm that directly converts the hybrid precoding/combining in the full array (FA) architecture to subarray (SA) architecture is proposed and examined in this thesis. It is called direct conversion of iterative hybrid precoding/combining from FA to SA (DCIFS) hybrid precoding/combining. The proposed DCIFS design takes into consideration the matrix structure of the analog and baseband precoding and combining in the design derivation. Moreover, it does not depend on the antenna array geometry, unlike other techniques, such as the orthogonal matching pursuit (OMP) hybrid precoding/combining approach, nor does it assume any other constraints. Simulation results show that the proposed DCIFS hybrid design, when compared to the FA hybrid designs counterpart, can provide a spectral efficiency that is close to optimum while maintaining a very low complexity and better spectral efficiency than the conventional SA hybrid design with the same hardware complexity.

Acknowledgments

From the bottom of my heart, I would like to express my gratitude in a myriad of ways to the following people, without whom I would not have made it through my doctoral degree.

I would like to express my gratitude to my supervisor Professor Claude D'Amours and my co-supervisor Francois Chan for their guidance on this journey, patience, and care. I am very grateful to the advisory committee members for their time, constructive feedback, and encouragement during the thesis proposal. My thanks also go to anonymous reviewers of different papers that have arisen from this work, whose feedback played a significant role in shaping its current state.

To my family, I am eternally indebted to my father and my siblings' unwavering support, whom I look up to. It is from them that I gather my passion for higher education and the pursuit of knowledge. I am forever grateful to my wife, without whom I would not have crossed the finish line. Your love and encouragement are ever-present throughout the good times and the most stressful of times. To my children. You made me stronger, better, and fuller than I'd ever dreamed. I beg their pardon for missing out on some moments of their childhood while working towards my Ph.D. In remembrance of my mother, Mom, your wish came true. I made it.

There are always people who make success possible and rewarding. My friends who stayed with me on happy and sad days during this journey, the ones who helped me when I needed it the most. I would also like to express my special thanks to my colleagues and the faculty members at the University of Ottawa.

Mohamed Alouzi

Table of Contents

LIST OF FIGURES

LIST OF ALGORITHMS

LIST OF TABLES

LIST OF ABBREVIATIONS

ADC analog to digital converter

AOA angle of arrival

AOD angle of departure

AWGN additive white Gaussian noise

BS base station

CI models close-in free space reference distance models

CSI channel state information

DAC digital to analog converter

dB decibels

LOS line of sight

MIMO multiple-input multiple-output

ML maximum likelihood

MMSE minimum mean-squared error

MM wave millimeter wave bands

MM wave massive MIMO millimeter wave massive multiple-input multiple-output

MRC maximum ration combining

MRT maximum ratio transmission

MS mobile station

NLOS non-line of sight

PLE path loss exponent

QAM quadrature amplitude modulation

RF chains radio-frequency chains

SD sphere decoding

SDR semidefinite relaxation

SISO single-input single-output

SNR signal-to-noise-ratio

SV model saleh valenzuela model

SVD singular value decomposition

UPAs uniform planar arrays

VBLAST vertical bell laboratories layered space-time

ZF zero-forcing

LIST OF SYMBOLS

α - Normalization constant chosen to satisfy the power constraint

α_l - Complex gain of the l^{th} path of mm wave channel

θ_l - Azimuth angle of arrival

$\emptyset_l$ - Azimuth angle of departure

$a_{MS}(\theta_l)$ - Antenna array response vectors at the MS

$a_{BS}^{H}(\emptyset_l)$ - Antenna array response vectors at the BS

λ - Wavelength of the mm wave signal

σ^2- Variance of the noise

$\mathcal{A}$ - Set of possible RF precoders based on phase shifters

$\mathbf{W_{RF}}$ - Analog combiner

$\mathbf{W_{BB}}$ - Baseband (digital) combiner

$\mathbf{W}$ - Hybrid combiner

$\mathbf{W_{opt}}$ - Unconstrained optimum digital combiner

$\mathbf{W}$- Massive MIMO linear detection matrix

C - Capacity of MIMO Channels

d_k - Complex large-scale fading coefficients

$FSPL(f, 1\ m)$ - Free space path loss in dB at separation distance of 1m

$\mathbf{F_{BB}}$ - Baseband (digital) precoder

F - Hybrid precoder

$\mathbf{F_{opt}}$ - Unconstrained optimum digital precoder

$\mathbf{F_{RF}}$ - Analog precoder

$\frac{E_b}{N_0}$ – Signal-to-noise ratio relative to each uncoded information bit

G_t - Transmitter antenna gains measured in dBi

G_r - Receiver antenna gains measured in dBi

$g_{k,n}$ - Complex small-scale fading coefficients

H- MIMO channel matrix

L - Number of paths at mm wave channel

n - Complex Gaussian variable used to represent the AWGN

N_t - Number of transmit antennas

N_r - Number of receive antennas

N_{BS} - Number of base station antennas

N_{MS} - Number of mobile station antennas

N_{RF} - Number of RF chains

N_s - Number of data streams

P_u - Uplink transmission power

P_d - Downlink transmission power

$PL^{CI}(f, d)$ - Close-in (CI) free space reference distance path loss model at frequency f and separation distance d

P_r - Received power P_r measured in dBm

P_t - Transmit powerP_r measured in dBm

$\overline{P_R}$ - Average power gain

R - Maximum achievable sum-rate or the spectral efficiency

$SINR_k$ - received signal-to-interference-plus-noise ratio (SINR) of the kth user

X_σ^{CI} - The shadow fading gain describing large-scale fluctuation about the mean path loss over distance, and it is modeled by the log-normal distribution with 0 dB mean and standard deviation σ measured in dB

CHAPTER 1: INTRODUCTION

1.1. MIMO (Multiple-Input Multiple-Output) Evolution

Wireless networks have continued to develop, and their use has significantly grown. Cellular phones are now part of huge wireless network systems and people use mobile phones on a daily basis in order to communicate with each other and exchange information.

MIMO (Multiple-Input Multiple-Output) is a wireless technique that utilizes an array of antennas to transmit a signal over a given frequency band, and another array of antennas at the receiver to receive the signal. There are two techniques in MIMO to transmit data across a given channel that consists of different propagation paths [1]. The first technique, called spatial diversity, improves the reliability of the system by sending the same data across different propagation paths. The second technique increases the data rate of the system by transmitting different portions of the data stream on different propagation paths. This is called spatial multiplexing and it provides a multiplexing gain or degree of freedom.

In MIMO systems operating in rich scattering environments, space-time codes (STC) were developed to provide diversity gains, while the Vertical Bell Laboratories Layered Space-Time Architecture (V-BLAST) was introduced to increase spectral efficiency through spatial multiplexing. Accurate estimates of channel state information at the receiver are crucial for V-BLAST, while for STC, these estimates should be available to either the transmitter or the receiver [1]. A high data rate can be achieved by increasing the number of transmit antennas without increasing the transmission power and required bandwidth. The motivation behind increasing the data rate or user capacity of a cellular system is to meet the demand for high data traffic in the upcoming years.

Massive MIMO [2] [3] has been proposed for 5G networks to achieve high capacity by using a very large number of transmit and/or receive antennas with transmit precoding and receive combining. In addition, significant improvement in communications quality of service (QOS), energy efficiency and in cost reduction is expected in massive MIMO. The simple linear precoding schemes, such as zero forcing (ZF), Maximum-Ratio Transmission (MRT) and Minimum Mean-Square Error (MMSE) can be successfully implemented in massive MIMO. The same linear schemes can be used in the receiver. The data transmission is done by following the Uplink or Downlink scenarios. In the downlink, the Base Station (BS) uses precoding matrices to precode the data symbols that are transmitted to a Mobile Station (MS) in the case of a single-user transmission or to several MSs for multi-user transmission. In the uplink the users send the data to the BS in their own cell where the data can be recovered by using linear processing techniques.

Although massive MIMO is considered a good technique to achieve a high capacity, in practice, channel estimation has to be performed, similarly to classical MIMO [2] . One way to estimate the channel state information in massive MIMO is to use orthogonal pilot sequences. However, pilot contamination, where different users in different cells use the same orthogonal pilots because of the limited available spectrum, is one of the challenging problems that needs to be solved.

Another method to increase the data rate in cellular systems is the use of the Millimeter Wave (mm wave) band [4] [5]. Systems operating in the mm wave band are able to transmit gigabits per second by taking advantage of the large bandwidth available at these frequencies. Mm wave communications is a promising technology for future outdoor cellular systems. The path loss at mm wave frequencies makes it difficult to implement these systems [6]; however, large antenna arrays can be packed into small chips at mm wave frequencies and can therefore be used to direct the transmitted signal towards the receiver to compensate for the high path loss [7]. Moreover, large antenna arrays help the design of beamforming techniques to direct the signal in a certain direction, hence reducing the path loss problem [6],[8], [9]. By using a baseband (digital) beamforming architecture, a high gain can be achieved, enabling multi-stream multi-user communications. However, large arrays of antennas make the baseband beamforming impractical because of the huge number of antennas, each requiring a power hungry RF chain. As a result, a digital beamforming architecture is difficult to implement as it leads to high power consumption and an increase of hardware complexity. Moreover, implementing baseband beamforming is based on the knowledge of the complete channel state information. The authors in [10] consider low Radio-Frequency (RF) complexity for the full digital transmit beamforming. Another beamforming design is Radio-Frequency (RF) beamforming, where both the precoder and combiner are implemented in the RF stage. Compared to digital beamforming, there are implementation advantages in terms of lower power consumption and lower hardware complexity because of the significantly reduced number of RF chains. Analog beamforming controls the phase of the transmitted signal at each antenna element via a network of analog phase shifters and is implemented in the RF domain. Analog beamforming is less complex than its digital counterpart, but the single RF chain can only support a single-user's single-stream transmission Moreover, analog beamforming is subject to additional constraints. For example, the phase shifters might be digitally controlled and have quantized phase values. These constraints limit the potential of analog only beamforming solutions compared to digital beamforming.

Hybrid beamforming architectures [11] - [16] overcome the limitation of analog beamforming by dividing the process between the analog and digital domains and using a number of RF chains that is much lower than the antenna array size. Single user hybrid precoding was specially designed for mm wave communications in [8] to exploit the limited scattering nature of the mm wave channel with the presence of large antenna arrays. In addition, some energy-efficiency devices such as low-resolution analog-to-digital converters (ADCs) and digital-to-analog converters (DACs) can also be adopted to reduce the power consumption [17] - [19]. In [8], the authors employ an algorithm based on the simultaneous orthogonal matching pursuit (SOMP) technique [20], [21] where the precoding and combining are done in both the baseband and RF domains. A hybrid precoder and combiner based on the SOMP algorithm can yield a performance close to that of an optimal digital beamformer while considerably decreasing the number of RF chains and hence, $N_{RF} < N_t$, where N_{RF} and N_t are the numbers of RF chains and transmit antennas, respectively. However, the main limitation of solving the sparse optimization problem is the high computational complexity and the need to assume known array geometries for both transmitter and receiver. In [22], the technique was refined, which reduced the computational complexity of the technique discussed in [8] while maintaining the same performance. The work in [22] does not address the channel array geometry limitations of [8]. The same approach was used in [23] to approximate the minimum mean squared error for the hybrid solution although the computational complexity is high. In [24], multiple antenna arrays with independent beamforming were employed to obtain diversity gains in mm wave systems. However, this work does not exploit the sparse nature of mm wave channels. An iterative hybrid design that approaches the performance of the digital precoder was proposed in [25], but the computational complexity is high due to the large number of entries that need to be updated. The low complexity Greedy hybrid precoding/combining, which avoids any assumption on the array geometry or channel structure, is proposed in [26]. Although this method provides good experimental results, no theoretical proof is provided for its performance.

The authors of [27] demonstrate that additional performance gains in hybrid precoding/combining can be obtained by optimizing the RF precoder/combiner without restricting them to predefined codebooks. However, this approach comes with higher computational complexity. Several hybrid precoding and combining algorithms were proposed in [28]. One of them, the Hybrid Design by Alternate Minimization (HD-AM) method, achieves high spectral efficiency with medium computational complexity, but it can only work in the special case where the number of data streams equals the number of RF chains. Another algorithm, the Fast Unitary Matching design, requires that the precoders and combiners are dictionary-based. Although its complexity is low, the spectral efficiency is lower than that of the other algorithms. The other algorithms do not make any assumption on the structure of the precoders/combiners, but the computational complexity is high [28]. Several algorithms alternately optimizing the digital precoder and the analog precoder were developed in [29]. The Manifold Optimization Based Hybrid Precoding (MO-AltMin) algorithm provides high spectral efficiency, but requires high computational complexity. A low-complexity algorithm for the fully-connected structure (PE-AltMin algorithm) was also deployed with lower complexity. Its spectral efficiency is close to that of MO-AltMin when the number of RF chains equals the number of data streams, but there is a performance gap compared to MO-AltMin when the number of RF chains increases [29]. Sohrabi and Yu [30] provide a heuristic hybrid beamforming design that achieves good performance, but the technique's computational complexity is relatively high compared to other solutions. In [31] and [32], the Euclidean distance between the hybrid precoding matrix and full-digital precoding matrix is minimized by developing a gradient projection algorithm for hybrid beamforming design and solving the matrix factorization problem using gradient and Hessian information, respectively. Although it is a good approach to improve the performance, the main limitation of these techniques is the high computational complexity. An iterative hierarchical hybrid precoding (HHP-Iterative) that divides the optimization problem into analog and digital parts has been proposed in [33]. It can achieve a spectral efficiency close to that of PE-AltMin, but the high computational complexity is the main limitation of this solution [33]. Furthermore, in multi-user scenarios, the digital beamformer is designed to eliminate inter-user interference and the analog precoder/combiner is designed by maximizing the user's signal power [34] - [37]. Hybrid beamforming with dynamic sub-connected structure and distributed architecture has been investigated in [38] - [45].

1.2. Aim

The aim of this research is to develop effective, novel methods to minimize the bit error rate (BER) performance of mm wave massive MIMO systems by using sphere decoding, and a semidefinite relaxation (SDR) detector. To the best of our knowledge, no previous work used theses detection methods in mm wave massive MIMO systems. Moreover, we have focused on hybrid beamforming algorithm design which plays an important role in maximizing the capacity and minimizing the BER of mm wave massive MIMO systems. We managed to solve the nonconvex cost functions by an iterative solution. Thus, we propose three novel algorithms for hybrid precoding and combining designs in mm wave massive MIMO systems in order to minimize the BER and achieve high spectral efficiency with lower complexity. Chapters 3, 4, 5, and 6 describe our research contributions with the purpose of proposing solutions to mm wave massive MIMO systems.

1.3. Contributions

In our first contribution, we apply the SD and SDR algorithms to the problem of sparse hybrid beamforming for outdoor uniform planar arrays (UPAs) used in mm wave massive MIMO systems. Here we consider transmission in the downlink with multiple data streams transmitted to a single user and we examine the effect of using these algorithms on the BER performance of the communication system. To the best of our knowledge, no previous work in the literature has used theses detection schemes with the sparse hybrid beamforming for mm wave massive MIMO systems. Because of the limited scattering characteristics of mm wave massive MIMO channel (few paths exist) in outdoor scenarios, the number of data streams N_s should be close to the number of dominant channel paths in mm wave [4]. Therefore, we use the SD algorithm and the SDR algorithm to improve the performance of UPAs sparse hybrid beamforming mm wave systems with a very low number of RF chains and assuming perfect mm wave channel state information at the MS and BS. By considering the case where there is only one BS and one MS in a single cell, the user can then use the effective channel and decode the transmitted information. To the best of our knowledge, the error performance of the SD and SDR algorithms in mm wave systems with UPAs hybrid beamforming is not available in the literature. Computer simulations show that SD and SDR can improve the performance by more than 10 dB and more than 6 dB, respectively compared to zero-forcing (ZF) or minimum mean-square error (MMSE) systems, which will allow the range of mm wave massive MIMO to be extended.

In our second contribution, we propose a new low-complexity hybrid precoding/ combining design using the gradient descent method for mm wave systems. Additionally, the proposed method provides near-optimal performance in terms of achievable spectral efficiency and BER. The main advantage of the proposed algorithms is that there is no need to make any assumption on the antenna array geometry or for any other constraints while maintaining low computational complexity. Specifically, we optimize the analog and the digital precoders/ combiners separately. Based on the history of the normalized analog precoders/combiners and by updating the digital precoders/combiners, the performance of the proposed hybrid design is close to that of the fully unconstrained digital one.

In our third contribution, we extend our work in order to improve the performance of hybrid precoding/combining design by using gradient descent with momentum and Newton's Method. Additionally, the proposed method in this thesis provides near optimal performance in terms of the achievable spectral efficiency and BER. Our results show that gradient descent with momentum and Newton's Method can significantly improve the performance of the proposed hybrid design and reduce the objective function with only a small number of iterations K compared to the proposed hybrid design in our second contribution. The proposed algorithms still has the same advantage as our second contribution, i.e, there is no need to make any assumption on the channel array geometry or channel structure while maintaining a low computational complexity.

In our second and third contributions, it is guaranteed that the proposed approaches converge to a local optimum point. Simulation results verify that the two proposed hybrid precoding/combining schemes outperform the other popular schemes and achieves a much better performance in terms of the achievable spectral efficiency and BER with low complexity.

In the fourth contribution, an iterative algorithm that directly converts the hybrid precoding/combining in the full array (FA) architecture to subarray (SA) architecture is proposed and examined. It is called direct conversion of iterative hybrid precoding/combining from FA to SA (DCIFS). The proposed DCIFS design does not depend on the antenna array geometry while maintaining a low computational complexity. Simulation results demonstrate that the proposed

DCIFS hybrid design, when compared to the FA hybrid designs counterpart, can provide spectral efficiency that is close to optimum while maintaining a very low hardware complexity and better spectral efficiency than the conventional SA hybrid design with the same hardware complexity.

1.4. Thesis Organization

The following chapters of this thesis are organized as follows:

- Chapter 2 will provide some background on classical MIMO, spatial multiplexing and receiver design, and the capacity of multi-antenna channels. The section on massive MIMO will describe massive MIMO, and examine the linear detection schemes and maximum achievable sum-rate. The section on mm wave massive MIMO systems will explore the characteristics of mm wave channels, examine the path loss model, mm wave channel model and beamforming design. The section on Numerical optimization schemes for minimization of a general function will describe the gradient descent with and without momentum.
- In Chapter 3, we propose the use of sphere decoding and semidefinite relaxation for sparse hybrid beamforming millimeter wave systems to improve the overall error performance, and compare them in terms of BER with ML, ZF, and MMSE.
- In Chapter 4, we explain the methodology of the proposed low complexity hybrid precoding and combining using the gradient descent method for millimeter wave systems, analyze the complexity of the proposed hybrid beamforming, and evaluate the performance of the proposed algorithm.
- In Chapter 5, we explain the methodology of the proposed low complexity hybrid precoding and combining by using gradient descent with momentum and Newton's Method for

millimeter wave systems, analyze the complexity of the proposed hybrid beamforming, and evaluate the performance of the proposed algorithm.

- In Chapter 6, we explain the methodology of the proposed low complexity direct conversion of hybrid precoding from full array architecture to subarray architecture for mm wave MIMO systems, analyze the complexity and the performance of the proposed DCIFS design.
- Chapter 7 concludes the thesis and describes the proposed future work.

1.5. Publications

The main results presented in Chapter 3 have been reported in [47] and [48]. The main results of Chapter 4 have been reported in [46]. The results of Chapter 5 have been submitted to IEEE Access [50]. Finally, the results of Chapter 6 have been published in [49]

CHAPTER 2: BACKGROUND

2.1. Classical MIMO

In wireless communication, a channel may be affected by fading which will impact the performance of the system. To mitigate this, it was proposed in the previous chapter to use the diversity technique, i.e., to provide the receiver with multiple versions of the same signal. The principle of diversity guarantees that the probability that multiple versions of a given signal are affected by fading at the same time is considerably reduced [1]. Therefore, diversity helps to improve the performance and reduce the error rate.

Several diversity methods can be applied and provide a number of advantages. These methods are described as follows [1].

1. Time diversity: Using time diversity, a message may be transmitted at different times by using a channel code.
2. Frequency diversity: This form of diversity uses different frequencies. It is applied by using different channels, or a technology such as Orthogonal Frequency Division Multiplexing (OFDM).
3. Spatial Diversity (Antenna Diversity): Spatial diversity is one of the most popular forms of diversity used in wireless communication systems. Multiple and spatially separated antennas are employed to transmit or receive uncorrelated signals. Antenna separation should be at least half of the carrier wavelength to ensure sufficiently uncorrelated signals at the receiver.

In the past, fading or multiple paths were considered as an interference; however, by using the MIMO technique, these multiple paths can be turned to our advantage. They can be used to improve the signal-to-noise ratio or to increase the data rate [51].

In a wireless communication environment with fading channels, a Line-of-Sight (LoS) radio propagation path will often not exist between the transmitter and receiver because of natural and man-made obstacles situated between the transmitter and receiver. As a result, the signal propagates via reflection, diffraction and scattering [1].

A MIMO system typically consists of N_t antennas at the transmitter and N_r antennas at the receiver as shown in Figure 2.1 [52] where each antenna not only receives the direct signal path (Line-of-Sight), but also a fraction of signal (Non-Line-of-Sight) due to the scattering, diffraction and reflection. The fading path between antenna 1 at the transmitter and antenna 1 at the receiver is represented by the channel response h_{11}. The channel response of the path formed between antenna 1 at the transmitter and antenna 2 at the receiver is denoted as h_{21}, and so on. Therefore, the dimension of the channel transmission matrix **H** is $N_r \times N_t$, where N_r is the number of receive antennas and N_t is the number of transmit antennas.

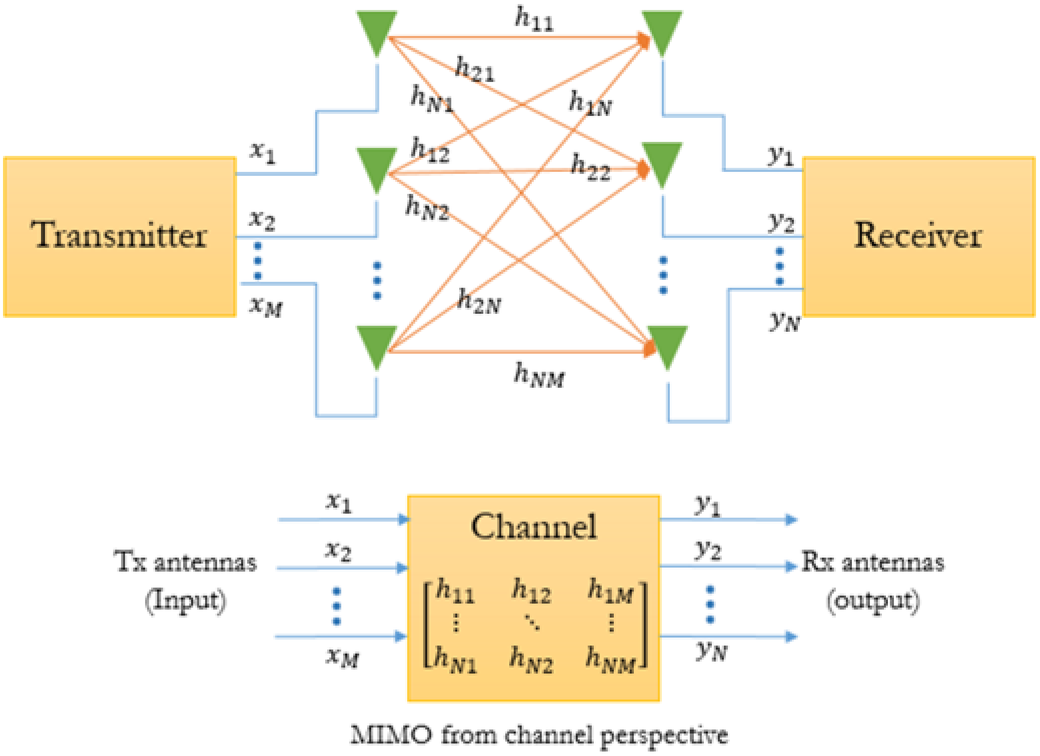

Figure 2. 1. Multiple Input Multiple Output (MIMO) systems [52]

The channel matrix is modeled by large-scale and small-scale fading [1]. The large-scale model or path loss model, which is caused by the path loss of the signal as a function of distance, and shadowing by large objects such as buildings and hills, is used to predict the received signal strength [1]. Small-scale fading, which is caused by the constructive and destructive interference of the multiple signal paths between the transmitter and receiver can be classified into two types [1]:

1. Flat fading: The bandwidth of the signal is smaller than the coherence bandwidth B_c of the channel and therefore, the channel can be treated as flat.
2. Frequency selective fading: This occurs when the bandwidth of the signal is larger than the coherence bandwidth B_c of the channel.

A flat fading signal, commonly assumed in wireless communication, follows the Rician distribution (LOS) or Rayleigh distribution (NLOS) [1].

The received vector y is expressed in terms of the channel transmission matrix **H** as follows

$$\mathrm{y} = \mathbf{H}\mathrm{x} + \mathrm{n} \qquad (2.1)$$

where x is the transmitted symbols vector, n is the vector of receiver noise whose elements are considered as zero-mean additive white Gaussian noise (AWGN) with variance σ^2, and **H** is the fading channel matrix.

There are two main functions for a MIMO system [1]:

- Spatial diversity: The same information-bearing signals are transmitted or received from multiple antennas, thereby improving the reliability of the system. Spatial diversity always refers to transmit and receive diversity.
- Spatial multiplexing: In this form of MIMO, the multiple independent data streams are simultaneously transmitted by many transmit antennas to achieve a higher transmission speed and increase the data rate of the system.

There are many technologies in MIMO that implement these two functions. In the following sections, we will focus on the spatial multiplexing function.

2.1.1. Spatial Multiplexing and Receiver Design

The data rate of a MIMO system can be increased by transmitting different copies of the data streams on different propagation paths. This is called spatial multiplexing and it provides a multiplexing gain for the MIMO system. Thus, the multiple independent data streams are transmitted at the same time by many transmit antennas to achieve a higher speed and increase the data rate of the system [1].

In this thesis, we will focus on three algorithms at the receiver to detect the transmitted symbols $\hat{\mathrm{x}}$ in equation (2.1), which are linear detection schemes, Sphere Decoding (SD) algorithm and semidefinite relaxation (SDR) detector.

2.1.1.1. Linear Detection Schemes

For linear detection, the transmitted symbols $\hat{\mathrm{x}}$ can be detected by multiplying y with the linear detection matrix $\mathbf{W} \in C^{N_t \, X \, N_r}$ as follows [1]

$$\hat{\mathrm{x}} = \mathbf{W}\mathrm{y} \qquad (2.2)$$

The linear detection matrix **W** can be designed by using one of the following techniques [1]

1- Zero-Forcing Receiver:

Zero-forcing (ZF) receivers take the data streams interference into account, but neglect the effect of noise [1]. The ZF receiver matrix **W** is the left or right pseudo-inverse of the channel matrix **H**. If an $N_r \times N_t$ matrix **H** is full rank, then it possesses a left pseudo-inverse of the form [1]

$$\mathbf{W} = (\mathbf{H}^{\mathbf{H}}\mathbf{H})^{-1}\mathbf{H}^{\mathbf{H}} \text{ if } N_r > N_t \qquad (2.3)$$

where the superscript H denotes the transpose conjugate, and it possesses a right pseudo-inverse of the form [1]

$$\mathbf{W} = \mathbf{H}^{\mathbf{H}}(\mathbf{H}\mathbf{H}^{\mathbf{H}})^{-1} \text{ if } N_r < N_t \qquad (2.4)$$

Moreover, if **H** is a square and full rank (non-singular) matrix, then [1]

$$\mathbf{W} = (\mathbf{H}\ )^{-1} \quad \text{if} \quad N_r = N_t \qquad (2.5)$$

and we get the same results as before. Neglecting the effect of noise makes the performance of ZF suboptimal. The ZF decoder's complexity is essentially determined by finding the pseudo-inverse of the matrix H.

2- Minimum Mean-Square Error Receiver:

The linear minimum mean-square error (MMSE) receiver aims to minimize the mean-square error between the estimated vector $\hat{x} = \mathbf{W}y$ and the transmitted vector x [1]. Therefore, the MMSE receiver matrix is [1]

$$\mathbf{W} = (\mathbf{H}^{\mathbf{H}}\mathbf{H} + \sigma^2\, \mathbf{I}_{\mathbf{Nr}})^{-1}\, \mathbf{H}^{\mathbf{H}} \qquad (2.6)$$

where $\mathbf{I}_{\mathbf{Nr}}$ is the identity matrix and σ^2 is the variance of the i.i.d noise vector. As we can see from (2.6), the MMSE receiver matrix works as ZF at high SNR. Also, at low SNR, it minimizes the effect of noise. Thus, the performance of MMSE is better than ZF because it takes the noise effect into consideration and minimizes it. As a result, the MMSE's complexity is higher than that of ZF because the noise variance is involved.

If the Hermitian matrix $\mathbf{H}^{\mathbf{H}}\mathbf{H}$ is low rank, MMSE is still able to inverse it when the limit of the noise variance σ^2 goes to zero (very large SNR). Let us define

$$\mathbf{A} = \mathbf{H}^{\mathbf{H}}\mathbf{H}$$

where **A** is a positive definite (or semi-definite) Hermitian matrix. Then **A** can be diagonalized as follows

$$\mathbf{A} = \mathbf{U^H \Lambda U}$$

where $\mathbf{U}$ is a unitary matrix and $\mathbf{\Lambda} = \mathrm{diag}\ (\lambda_i), \mathrm{i} = 1,2, \dots, N_r$. Notice that λ_i are the eigenvalues of $\mathbf{A}$ or the square of the singular values of $\mathbf{H}$. Also, the values of λ_i have to be real and non-negative. Substituting the matrix $\mathbf{A}$ in the MMSE detector equation and taking the limit as the noise variance goes to zero yield

$$\mathbf{W} = \ (\mathbf{U^H \Lambda U}\ +\ \lim_{\sigma^2 \to 0} \sigma^2\, \mathbf{I_{Nr}})^{-1}\ \mathbf{H^H} \qquad (2.7)$$

$$\mathbf{W} = \ \mathbf{U^H}(\ \mathbf{\Lambda}\ +\ \lim_{\sigma^2 \to 0} \sigma^2\, \mathbf{I_{Nr}}\ )^{-1} \mathbf{U}\ \mathbf{H^H}$$

Because the diagonal matrix $\mathbf{\Lambda}$ has non- negative values and the noise variance entries as well, the inverse of the above matrix exists.

2.1.1.2. Semidefinite Relaxation

To avoid complex-valued variables, (2.1) is rewritten as

$$\mathrm{y} = \mathbf{H}\mathrm{x} + \mathrm{n} \qquad (2.8)$$

or

$$\begin{bmatrix} \mathrm{Re(y)} \\ \mathrm{Im(y)} \end{bmatrix} = \begin{bmatrix} \mathrm{Re}(\mathbf{H}) & -\,\mathrm{Im}(\mathbf{H}) \\ \mathrm{Im}(\mathbf{H}) & \mathrm{Re}(\mathbf{H}) \end{bmatrix} \begin{bmatrix} \mathrm{Re(x)} \\ \mathrm{Im(x)} \end{bmatrix} + \begin{bmatrix} \mathrm{Re(n)} \\ \mathrm{Im(n)} \end{bmatrix}$$

At the receiver, the ML detector for 16-QAM modulation can be implemented as follows [53] - [55]

$$\mathrm{ML:}\ \min_{\mathrm{x}} \|\mathrm{y} - \mathbf{H}\mathrm{x}\|^2 \qquad (2.9a)$$

$$\mathrm{s.t.}\ \ \mathrm{x_i} \in \{\pm 1, \pm 3\}, \quad \mathrm{i} = 1, \dots, 2N_t \qquad (2.9b)$$

The ML detector performs an exhaustive search over the whole set of possible symbols $\mathrm{x_i} \in \mathrm{X}$ in order to choose the one that minimizes the Euclidean distance between the received signal y and the reconstructed signal $\mathbf{H}\mathrm{x}$ [53], [55]. Since there are 2^{KN_t} possibilities, where K is the number of bits per symbol, the ML detector is optimum, but its complexity grows exponentially. Clearly, as K or N_t increases, ML detection is a hard problem and becomes impractical [53] - [55]. Thus, ML detection is approximated using semidefinite relaxation.

To derive the SDR detector, first the alphabet constraint (2.9b) is expressed as [53], [54]

$$(\mathrm{x_i}-1)(\mathrm{x_i}+1)(\mathrm{x_i}-3)(\mathrm{x_i}+3)=0, \quad \mathrm{i}=1,\ldots,2N_t$$

Thus, for 16-QAM the ML problem (2.9) can be expressed as [53], [54]

$$\mathrm{ML}: \min_{\mathbf{x}} \|\mathrm{y}-\mathbf{H}\mathrm{x}\|^2 \qquad (2.10)$$

$$\text{s.t.} \qquad 1 \leq \mathrm{x_i}^2 \leq 9 \qquad (2.10a)$$

$$\mathrm{x_i}^2+4\mathrm{x_i}+3 \geq 0 \qquad (2.10b)$$

$$\mathrm{x_i}^2-4\mathrm{x_i}+3 \geq 0, \quad \mathrm{i}=1,\ldots,2N_t \qquad (2.10c)$$

The ML problem can be rewritten as follows

$$\|\mathrm{y}-\mathbf{H}\mathrm{x}\|^2 = \mathrm{x}^{\mathrm{T}}\mathbf{H}^{\mathbf{T}}\mathbf{H}\mathrm{x} - 2\mathrm{y}^{\mathrm{T}}\mathbf{H}\mathrm{x} + \|\mathrm{y}\|^2 \qquad (2.11)$$

$$= \mathrm{s}^{\mathrm{T}}\mathbf{L}\mathrm{s}$$

where

$$\mathbf{L} = \begin{bmatrix} \mathbf{H}^{\mathbf{T}}\mathbf{H} & -\mathbf{H}^{\mathbf{T}}\mathrm{y} \\ -\mathrm{y}^{\mathrm{T}}\mathbf{H} & \mathrm{y}^{\mathrm{T}}\mathrm{y} \end{bmatrix}, \text{ and } \mathrm{s} = \begin{bmatrix} \mathrm{x} \\ 1 \end{bmatrix}$$

Then, we define a rank-1 semidefinite matrix $\mathbf{S}$, $s^T\mathbf{L}s$= $\text{tr}(s^T\mathbf{L}s)$ =tr(SL), where $\mathbf{S} = ss^T$. Also, denote $\mathbf{S}_{i,j}$ for i,j=1,2, the (i,j)th sub-block of appropriate size inside S, where $\mathbf{S}_{1,1} = xx^T$, $\mathbf{S}_{1,2} = x$, $\mathbf{S}_{2,1} = x^T$, and $\mathbf{S}_{2,2} = 1$. Thus the detection problem in (2.10) is equivalent to [54]

$$\min_{\mathbf{S}} \text{tr}(\mathbf{SL}) \tag{2.12}$$

$$\text{s.t.} \quad 1 \preccurlyeq \text{diag}(\mathbf{S}_{1,1}) \preccurlyeq 9 \tag{2.12a}$$

$$\text{diag}(\mathbf{S}_{1,1}) + 4\mathbf{S}_{1,2} + 3 \cdot 1 \succcurlyeq 0 \tag{2.12b}$$

$$\text{diag}(\mathbf{S}_{1,1}) - 4\mathbf{S}_{1,2} + 3 \cdot 1 \succcurlyeq 0 \tag{2.12c}$$

$$\text{rank}(\mathbf{S}) = 1 \tag{2.12d}$$

$$\mathbf{S} \succcurlyeq 0 \tag{2.12e}$$

$$\mathbf{S}_{2,2} = 1 \tag{2.12f}$$

Please note that 1 and 9 are vectors in (2.12a), (2.12b), and (2.12c). The problem in (2.12) is not convex due to the rank-1 constraint. By dropping this constraint, the solution of this relaxation is the lower bound of the original problem (2.12). Finally, we obtain the following convex relaxation (SDR detector)

$$\text{SDR:} \quad \min_{\boldsymbol{S}} \text{tr}(\mathbf{SL}) \tag{2.13}$$

$$\begin{aligned} \text{s.t.} \quad & 1 \preccurlyeq \text{diag}(\mathbf{S}_{1,1}) \preccurlyeq 9 \\ & \text{diag}(\mathbf{S}_{1,1}) + 4\mathbf{S}_{1,2} + 3 \cdot 1 \succcurlyeq 0 \\ & \text{diag}(\mathbf{S}_{1,1}) - 4\mathbf{S}_{1,2} + 3 \cdot 1 \succcurlyeq 0 \\ & \mathbf{S} \succcurlyeq 0 \end{aligned}$$

$$\mathbf{S}_{2,2} = 1$$

where $\mathbf{S} \succcurlyeq 0$ means that $\mathbf{S}$ is positive semi-definite. The problem in (2.13) is a semi-definite program and any SDP solver, such as SeDuMi [56], based on interior-point methods, can be used to solve it in polynomial time.

If the optimal result $\mathbf{S}^*$ of SDR has rank one, then the relaxation is tight, and the ML solution of x is the first $2N_t$ elements of the last column of $\mathbf{S}$ [53] [54]

$$\widehat{\mathrm{x}}_\mathrm{i} = \mathrm{quantize}\left(\mathbf{S}^*_{\mathrm{i},2\mathrm{Ns}+1}\right), \ \mathrm{i} = 1, \dots, 2N_t$$

Otherwise, the optimal result $\mathbf{S}^*$ of SDR is only an approximation of ML and can be solved using eigenvalue decomposition. Let v and λ be the eigenvector and eigenvalue of $\mathbf{S}^*$ [53]

$$\mathbf{S}^* = \sum_{i=1}^{2N_t+1} \lambda_\mathrm{i} \mathrm{v}_\mathrm{i} \mathrm{v}_\mathrm{i}^\mathrm{T}$$

Then, we select the eigenvector corresponding to the maximum eigenvalue of $\mathbf{S}^*$ to be the solution of x [53]

$$\hat{\mathrm{x}} = \mathrm{quantize}\left(\sqrt{\lambda_{max}}\mathrm{v}_{\mathrm{max}}\right)$$

2.1.1.3. Sphere decoding method

The third scheme is Sphere decoding (SD), which is initially designed to decrease the high detection complexity of the Maximum Likelihood Detection method (ML) [57], and achieves a performance close to ML detection. In the ML detector, the search is between all the points in the constellation diagram and the solution that has the smallest distance to the received vector is selected; however, in the SD method, the search procedure is only inside a sphere of radius d

focused at the received signal y as shown in Fig 2.2. The ML is an optimal algorithm, but its computational complexity increases exponentially with the number of transmitting antennas and the modulation order [57].

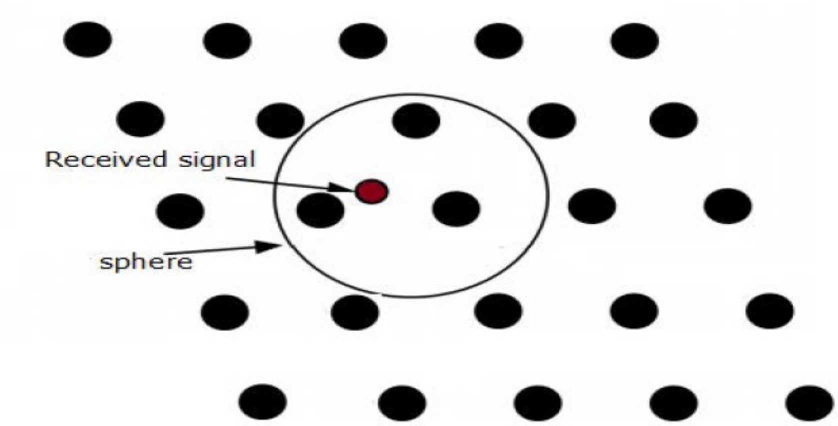

Figure 2. 2. Sphere Decoding Idea [57]

The points in the space which are placed outside the sphere are not considered. So, the number of points examined by the SD algorithm depends on the initial radius of the sphere. If the radius is large, there is a huge number of points inside the sphere and it will result in a high computational complexity. If the initial radius is very small, there may be no point inside the sphere [57]. In general, the SD works by finding all the symbols (points) of the transmitted vector within a radius d by going from the lower layer and up until it reaches the dimension of the transmitted vector at the same radius d. Moreover, the SD algorithm makes a tree of different branches with level k^{th} and each level corresponds to the points inside the sphere of radius d as shown in Fig 2.3 [57]

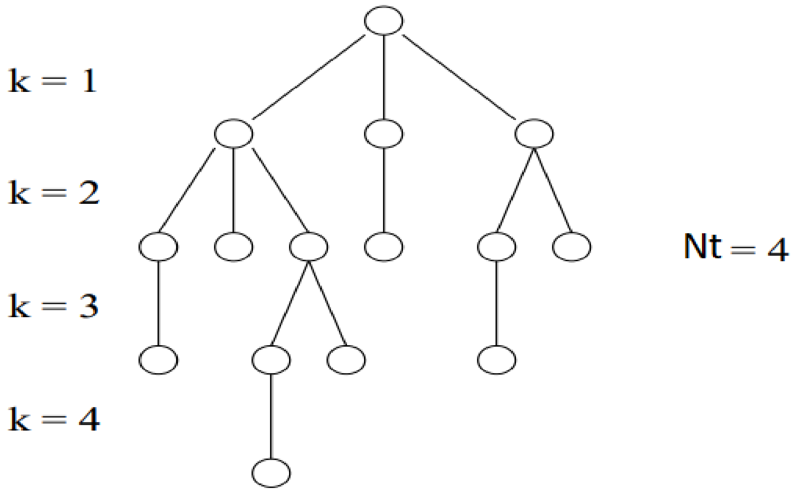

Figure 2. 3. Sample tree generated to determine lattice points in a 4-dimensional sphere [57]

The key objective of the SD is to find the solution $\hat{x}$ with the smallest Euclidean distance from the received signal. Also, the SD accomplishes the search of whole points within the sphere of the dimension of the transmitted vector, that can be found for the case of $N_r = N_t$ as follows [57]

$$\|\mathrm{y} - \mathbf{H}\mathrm{x}\|^2 \le d^2 \qquad (2.14)$$

which means that **H**x lies inside the sphere of radius d.

To solve this problem, QR factorization of the matrix **H** is used as follows [57]

$$\|\mathrm{y} - \mathbf{QR}\mathrm{x}\|^2 \le d^2$$

where **R** is an $N_t \times N_t$ upper triangular matrix and **Q** is an $N_r \times N_t$ orthogonal matrix where $\mathbf{QQ^H} = \mathbf{Q^HQ} = \mathbf{I}$. Please note that if $N_r \lesseqgtr N_t$, the matrix **Q** is semi-unitary in this case. The equation above can be written as [57]

$$\|\mathbf{Q}(\mathbf{Q^H}\mathrm{y} - \mathbf{R}\mathrm{x})\|^2 \ \leq \ d^2$$

The unitary matrices **Q** are rotations; thus, the above equation has the same length as the following one [57]

$$\|\mathrm{u} - \mathbf{R}\mathrm{x}\|^2 \ \leq \ d^2$$

where $\mathrm{u} = \mathbf{Q^H}\mathrm{y}$. The left side of the above equation can be expressed as [57]

$$\dots\dots. + (u_{Nt-1} - r_{Nt-1,Nt}x_{Nt} - r_{Nt-1,Nt-1}x_{Nt-1})^2 + (u_{Nt} - r_{Nt,Nt}x_{Nt})^2 \ \leq \ d^2$$

(2.15)

First, the SD detector proceeds by finding x_{Nt} that makes $(u_{Nt} - r_{Nt,Nt}x_{Nt})^2 \ \leq \ d^2$, then finding the second symbol x_{Nt-1} which is inside the sphere by satisfying the following condition

$$(u_{Nt-1} - r_{Nt-1,Nt}x_{Nt} - r_{Nt-1,Nt-1}x_{Nt-1})^2 \ \leq \ d^2 - \ (u_{Nt} - r_{Nt,Nt}x_{Nt})^2,$$

and so on until x_1 is estimated, then the radius is updated and the algorithm is repeated again taking into account the trajectories used for the first estimated transmitted vector to make sure only new points need to be visited. After many iterations, the final transmitted vector x with the smallest distance to the received vector is estimated. Moreover, the complexity of such an algorithm will depend on the initial radius passed to the SD and on the size of the tree, i.e., on the number of points visited by the algorithm in different dimensions to detect the transmitted symbols. We will show later that SD decoding performs better than the linear detection schemes (ZF and MMSE), although it is more complex depending on the number of points in the sphere. The complexity of SD can be reduced by efficiently selecting the radius as we will show later. Moreover, there are some works done to decrease the complexity for the SD algorithm by improving the selection of the radius for conventional MIMO [58] - [60].

2.1.2. Capacity of Multi-Antenna Channels

MIMO technology offers very high capacity with increasing SNR for a large number of antennas at both transmitter and receiver. In the case of independent Rayleigh or Rician fading paths between antenna elements at both transmitter and receiver, the expression of the general capacity C for known channel state information (CSI) at the transmitter is [1] [61]

$$C = \log_2 \det\left(\mathbf{I}_{\mathbf{N_r}} + \left(\frac{SNR}{N_t}\right).\ \mathbf{H}.\mathbf{H}^{\mathbf{H}}\right) \quad \text{bps/HZ} \qquad (2.16)$$

where N_r is the number of receive antennas, N_t is the number of transmit antennas, small **H** stands for transpose conjugate, and $\mathbf{I_m}$ is the m x m identity matrix.

In general, the capacity of a MIMO channel increases linearly with the number of antennas.

2.2. Massive MIMO

In upcoming years, the amount of data traffic in wireless communication will increase considerably; therefore, a new generation network, 5G, has to be deployed to increase the data capacity 1000 times compared to current 4G systems [4]. Energy efficiency and lower latency are also expected in the future network [4]. In order to increase the spectral efficiency, we need to have one of the following options

1- Very large number of base station antennas [2], [3], [62] - [64].
2- Small cells [63].
3- In order to support more users, increasing the bandwidth by using the high frequency bands (millimeter Wave) is a very good choice.

In massive MIMO for example, the industry is trying to increase the number N_t of BS antennas to 100 or more in order to simultaneously serve a large number of users K, say tens, with single or multiple antennas, in the same frequency band [62]. In addition, small cells are also expected in massive MIMO [4], [63]. The channel state information **H** is the channel propagation matrix between the K users and BS antennas array. In general, the channel propagation is modeled as a Rayleigh or Rician fading channel. In practice, the channel matrix has to be estimated by using orthogonal pilot sequences in the uplink transmission [4]. After estimating the channel state information in the uplink transmission, the BS uses the estimated channel in downlink transmission to precode the data streams to all users.

Consider a Massive MU-MIMO BS with N_t antennas that serves K single-antenna or multiple-antennas users. Denote the channel coefficient from the k^{th} user to the n^{th} antenna of the BS as $h_{k,n}$ in the uplink case, which is equal to a complex small-scale fading factor times an amplitude factor that accounts for geometric attenuation and large-scale fading [2], [65]:

$$h_{k,n} = g_{k,n}\sqrt{d_k} \qquad (2.17)$$

where $g_{k,n}$ and d_k represent the complex small, and large-scale fading coefficients, respectively. The small-scale fading coefficients are assumed to be independent for each user, while the large-scale ones are the same for all the N_t antennas but depend on the user's position [65]. Then, the channel matrix experienced by all the K users in the uplink scenario can be expressed as [2], [65]

$$\begin{pmatrix} h_{1,1} & \cdots & h_{K,1} \\ \vdots & \ddots & \vdots \\ h_{1,N_t} & \cdots & h_{K,N_t} \end{pmatrix} = \mathbf{G}\sqrt{\mathbf{D}} \tag{2.18}$$

where

$$\mathbf{G} = \begin{pmatrix} g_{1,1} & \cdots & g_{K,1} \\ \vdots & \ddots & \vdots \\ g_{1,N_t} & \cdots & g_{K,N_t} \end{pmatrix}$$

$$\mathbf{D} = \begin{pmatrix} d_1 & \cdots & \dots \\ \vdots & \ddots & \vdots \\ \dots & \cdots & d_K \end{pmatrix}$$

In a massive MIMO setup, as $N_t \gg K$, there are two system protocols, which are frequency-division duplex (FDD) or time-division duplex (TDD) used for data transmission [62]. The TDD scheme uses the same frequency band for uplink and downlink communication whereas FDD uses separate frequency bands for uplink and downlink communication. The TDD scheme is more efficient than FDD because the channel estimation in TDD is reciprocal, which means that the estimated channel in the uplink case is the same as the downlink. Therefore, the estimated channel can be used by BS to precode the data streams. However, in FDD case, the channel estimation is not reciprocal [62] [64].

The data transmission in massive MIMO as mentioned above is done by implementing the uplink or downlink techniques. Uplink transmission is the scenario where the K users transmit signals to the BS. Let s_k be the transmitted signal from the k^{th} user. Since the K users share the same time-frequency resources, the N_tx1 received signal vector at the BS is modeled as follows [2], [62], [64]

$$\mathrm{y_u} = \sqrt{P_u}\,\mathbf{H}\mathrm{s} + \mathrm{n_u} \qquad (2.19)$$

where P_u is the uplink transmission power, $\mathrm{s} \in C^{KX\,1}$ is the transmitted symbols from K users, $\mathrm{n_u} \in C^{N_t x1}$ is the additive white noise vector with independent components, and $\mathbf{H} \in C^{N_t X\,K}$ is the channel matrix.

With linear detection schemes at the BS, the transmitted symbols $\hat{\mathrm{s}}$ can be detected by multiplying $\mathrm{y_u}$ with the linear detection matrix $\mathbf{W} \in C^{N_t\,X\,K}$ as follows [2], [64]

$$\hat{\mathrm{s}} = \mathbf{W}^{\boldsymbol{H}}\mathrm{y}_u \qquad (2.20)$$

Therefore, the received signal-to-interference-plus-noise ratio (SINR) of the kth stream is given by [64]

$$SINR_k = \frac{P_u\left|\mathrm{w}_k^{\mathrm{T}^*}\mathrm{h}_k\right|^2}{P_u\sum_{k'\neq k}^{K}\left|\mathrm{w}_k^{\mathrm{T}^*}h_{k'}\right|^2 + \sigma^2\|\mathrm{w}_k\|^2} \qquad (2.21)$$

where $\mathrm{w_k}$ denotes the k^{th} column of matrix $\mathbf{W}$.

Then, the maximum achievable sum-rate is given by [64]

$$R = \sum_{k=1}^{K}\{log_2(1 + SINR_k)\} \qquad (2.22)$$

The linear detection matrix $\mathbf{W}$ can be designed by using one of the following techniques [64]

1- Maximum-Ratio Combining receiver (MRC):

We set $\mathbf{W}$ equal to $\mathbf{H}^{*}$, which is the complex conjugate of $\mathbf{H}$. At low SNR, MRC can achieve the same array gain as in the case of a single-user system, but it performs poorly in multiuser interference.

2- Zero-Forcing Receiver:

In contrast to MRC, ZF receivers take the multiuser interference into account. The ZF receiver matrix is the pseudo-inverse of the channel matrix **H**. With ZF, we have

$$\mathbf{W} = \mathbf{H}(\mathbf{H}^{\mathbf{H}}\mathbf{H})^{-1} \qquad (2.23)$$

where the superscript H is the transpose conjugate.

3- Minimum Mean-Square Error Receiver:

The linear minimum mean-square error (MMSE) receiver aims to minimize the mean-square error between the estimate $\mathbf{W}^{\mathbf{H}}\mathrm{y}_{\mathrm{u}}$ and the transmitted signal s. Therefore, the MMSE receiver matrix is

$$\mathbf{W} = \mathbf{H}(\mathbf{H}^{\mathbf{H}}\mathbf{H} + \sigma^{2}\mathbf{I}_{\mathbf{K}})^{-1} \qquad (2.24)$$

where $\mathbf{I}_{\mathbf{K}}$ is the identity matrix, and σ^{2} is the variance of the noise. MMSE receiver matrix works as MRC at low SNR and as ZF at high SNR.

In the downlink transmission scenario, the BS transmits data to all K users. Let $\mathrm{x} \in C^{Kx1}$ be the transmitted symbols vector intended for all K users. Then by using linear precoding technique, the precoding vector $\mathrm{x_F}$ [2], [64] is

$$\mathrm{x}_F = \sqrt{\alpha}\mathbf{F}\mathrm{x} \qquad (2.25)$$

where $\mathbf{F} \in C^{N_t\, x\, K}$ is the precoding matrix, and α is a normalization constant chosen to satisfy the power constraint $E\{\|\mathrm{x}_F\|^2\} = 1$. Thus [64],

$$\alpha = \frac{1}{\{tr(\mathbf{FF^H})\}} \qquad (2.26)$$

Therefore, the received signal at K users is given by [64]

$$\mathrm{y_d} = \sqrt{P_d}\mathbf{H^H}\mathrm{x}_F + \mathrm{n_d} \qquad (2.27)$$

where P_d is the downlink transmission power, $\mathrm{n_d} \in \mathbb{C}^{KX1}$ is a Gaussian noise vector, and $\mathbf{H^H} \in \mathbb{C}^{KxN_t}$ is the channel matrix.

By implementing the precoding techniques above, the $SINR_k$ is given as follows [64]

$$SINR_k = \frac{\alpha P_d \left|\mathrm{h}_k{}^*\mathrm{f}_k\right|^2}{\alpha P_d \sum_{k' \neq k}^{K} \left|\mathrm{h}_k{}^*\mathrm{f}_{k'}\right|^2 + \sigma^2} \qquad (2.28)$$

where $\mathrm{f_k}$ denotes the k^{th} column of matrix $\mathbf{F}$. Thus, the maximum achievable sum-rate in the downlink scenario is given by [64]

$$R = \sum_{k=1}^{K} \{log_2(1 + SINR_k)\} \qquad (2.29)$$

The three linear precoders are maximum-ratio transmission (MRT) (also called conjugate beamforming), ZF, and MMSE precoders; similarly, the precoding techniques have similar operational properties as MRC, ZF, and MMSE. The equations for these precoders are as follows [2], [64]

$$\mathbf{F} = \left\{ \begin{array}{ll} \mathbf{H}, & \text{for MRT} \\ \mathbf{H}(\mathbf{H^H H})^{-1}, & \text{for ZF} \\ \mathbf{H}(\mathbf{H^H H} + \frac{K}{P_d}\mathbf{I_K})^{-1}, & \text{for MMSE} \end{array} \right\} \qquad (2.30)$$

Although massive MIMO is promising for 5G networks, it has some drawbacks. As we know, the existing MIMO systems (such as LTE) are implemented with a small number of BS antennas N_t (between 1 and 10) [4]. In this case, the number of RF (Radio-Frequency) chains, DACs (Digital-to-Analog converters), and ADCs (Analog-to-Digital converters), which are the most expensive and power-hungry parts of a wireless transceiver [4], can be the same as the number of BS antennas N_t. In addition, this small network has a light load, so a small number of active users is served at each time instant. Therefore, the problem of pilot contamination is not a big issue [4]. However, in a massive MIMO system with 100 or more BS antennas N_t, having N_t RF chains is practically unfeasible because of the increasing cost and energy consumption. Specifically, when the transmission bandwidth is very large, the energy consumption of ADCs would be unacceptably high. Thus, there is ongoing research in utilizing hybrid beamforming, which uses a small number of RF chains, and using it in the channel estimation. In addition, in massive MIMO, a large number of active users is served at each time instant resulting in an increased number of orthogonal pilot sequences [4]. As a result, the system load becomes very high, and that causes the problem of pilot contamination, which is still an open research problem.

2.3. Millimeter Wave Massive MIMO Systems

Because massive MIMO has some drawbacks as we mentioned above, it is being considered in conjunction with millimeter wave (mm wave) frequencies (i.e. carrier frequency > 28 GHz), where many antennas can be packed into small chips. In addition, this new system offers a higher bandwidth (gigabits per second) and supports applications that require low latency by using mm wave systems compared to the current communication system (4G) [5]. As a result, a mm wave massive MIMO system is able to meet the data rate demands in the upcoming years. It is particularly promising for future outdoor 5G systems [5].

The mm wave frequency bands have different characteristics from the lower ones, so the new system needs different standards and modeling. For example, the mm wave path loss is much higher than the low frequency's path loss, especially for NLOS paths [6]; however, using directional antennas can mitigate this higher path loss with 200 m distance separation between the transmitter and receiver [7]. In addition, the need for directional antennas in mm wave systems makes the delay spread, which is the difference between the time of arrival of the earliest significant multipath components and the time of arrival of the latest ones, much lower compared to low frequency bands [7]. Penetration losses also are much higher in indoor-to-outdoor scenarios, so the indoor users should not communicate with the outdoor base stations [6]. The advantage of packing many antennas in small chips and using directional antennas make the mm wave channel model different [6], [8]. Mm wave channels are often sparse in the angular and time domain [6],

[8], [9], with a few scattering clusters and each of them with several rays (a few paths exist including LOS path). Because of the smaller wavelength, a signal at mm wave frequencies experiences the reflection and scattering in NLOS paths, but the diffraction is much lower. Therefore, mm wave signals are attenuated by smaller objects such as human body, glass, trees and rain. The penetration loss caused by a human body is measured between 20 and 30 dB [6]. Finally, some properties that are true for low frequency systems such as multi-path delay spread, angle spread and Doppler shift are used again in mm wave channel models [66].

2.3.1. Path Loss Model in Outdoor Scenario

As we mentioned above, the mm wave antenna arrays have to be directional to overcome the higher path loss with 200m distance separation between the transmitter and receiver [7] [67]. Therefore, it is critical to develop new models for system design. The large-scale propagation path loss at mm wave is generated by different models; however, the close-in (CI) free space reference distance model is very popular, especially for outdoor environments [68], [69]. The CI model is given as follows [68]:

$$PL^{CI}(f,d)[dB] = FSPL(f,1\,m)[dB] + 10n\,log_{10}(d) + X_{\sigma}^{CI} \qquad (2.31)$$

where n denotes the path loss exponent (PLE) with reference distance 1 m, X_{σ}^{CI} is the shadow fading gain describing large-scale fluctuation about the mean path loss over distance and it is modeled by the log-normal distribution with 0 dB mean and standard deviation σ measured in dB, d is the separation distance between the transmitter and receiver, and $FSPL(f,1\,m)$ denotes the free space path loss in dB at a separation distance of 1 m and is given by [68]

$$FSPL(f, 1\ m)[dB] = 20log_{10}(\frac{4\pi f}{c}) \qquad (2.32)$$

where c is the speed of light and f is the carrier frequency. The separation distance between receiver and transmitter can range up to 200 m in outdoor scenarios. For a larger distance (> 200 meters), the receiver signal strength becomes difficult to capture [67], [68].

The received power P_r measured in dBm, given the transmit power P_t, can be expressed as follows [66]

$$P_r[dBm] = P_t[dBm] + G_t[dBi] + G_r[dBi] - PL^{CI}(f, d)[dB] \qquad (2.33)$$

where G_t and G_r are the transmitter and receiver antenna gains in dBi, respectively.

2.3.2. Channel Model and Beamforming Design

Due to the small wavelength of signals at mm wave frequency bands, it is mentioned above that large arrays can be used at both the transmitter and receiver to direct a beam in a certain direction in order to get the strongest received power [7]. Therefore, beamforming schemes can be exploited to mitigate the high path loss. As a result, the channel models are different for mm wave massive MIMO systems [6].

A- Channel Model:

The widely used Saleh-Velenzuela (SV) model is used to represent the limited spatial selectivity or scattering characteristic caused by the high path loss of a mm wave channel in outdoor scenarios [2] - [17], [66], [70]. Therefore, in this thesis we adopt the narrowband clustered channel which is given by [17] - [30]

$$\mathbf{H} = \sqrt{N_{BS}N_{MS}/N_{cl}N_{ray}} \ \times \sum_{i,l} \alpha_{il}\Lambda_{\mathrm{r}}(\emptyset^{\mathrm{r}}_{il}, \theta^{\mathrm{r}}_{il})\Lambda_{t}\ (\emptyset^{\mathrm{t}}_{il}, \theta^{\mathrm{t}}_{il})\mathsf{a}_{\mathrm{r}}(\emptyset^{\mathrm{r}}_{il}, \theta^{\mathrm{r}}_{il})\mathsf{a}_{t}(\emptyset^{\mathrm{t}}_{il}, \theta^{\mathrm{t}}_{il})^{*} \quad (2.34)$$

where $N_{BS}, N_{MS}, N_{cl}, N_{ray}$ are the number of BS, MS antennas, the number of scattering clusters, and the number of propagation paths respectively. α_{il} is the complex gain of the l^{th} path and the i^{th} cluster and it is assumed to be Rayleigh distributed, i.e., $\alpha_{il} \sim$ i.i.d. $C\aleph(0,\overline{P_{\alpha,l}})$ with $\overline{P_{\alpha,l}}$ the average power of the i^{th} cluster, and $\emptyset^{\mathrm{t}}_{il}\ (\theta^{\mathrm{t}}_{il}), \emptyset^{\mathrm{r}}_{il}\ (\theta^{\mathrm{r}}_{il})$ are the l^{th} path's azimuth (elevation) angles of departure and arrival (AODs/AOAs) in the i^{th} cluster, respectively, with uniform distribution. Also, $\Lambda_{\mathrm{t}}\ (\emptyset^{\mathrm{t}}_{il}, \theta^{\mathrm{t}}_{il})$ and $\Lambda_{\mathrm{r}}(\emptyset^{\mathrm{r}}_{il}, \theta^{\mathrm{r}}_{il})$ correspond to the transmit and receive antenna element gain at their departure and arrival angles. In this paper, it is assumed that each antenna element has unity gain. Finally, $\mathsf{a}_{\mathrm{t}}(\emptyset^{\mathrm{t}}_{il}, \theta^{\mathrm{t}}_{il})^{\mathrm{H}}$ and $\mathsf{a}_{\mathrm{r}}(\emptyset^{\mathrm{r}}_{il}, \theta^{\mathrm{r}}_{il})$ are the antenna array response vectors at their azimuth and elevation angles of departure and arrival at the BS and MS respectively. They are usually applied to uniform planar arrays (UPAs), but can be applied to different antennas arrays as well [2], [6], [8], and [9]. For a UPA [8]

$$\mathsf{a}_{\mathrm{t}}(\emptyset, \theta) = \frac{1}{\sqrt{N_{BS}}}[1, e^{j\left(\frac{2\pi}{\lambda}\right) d\ (m\ sin(\emptyset)\sin(\theta)+n\cos(\theta))}, \ldots, e^{j\left(\frac{2\pi}{\lambda}\right) d\ ((W-1)sin(\emptyset)\sin(\theta)+(H-1)\cos(\theta))}]^{T}$$

(2.35)

where $0 \leq m < w$ and $0 \leq n < h$ are the width and height indices of an antenna element respectively and the antenna array size is wh. Also, λ is the wavelength of the mm wave signal, and d is the distance between the antenna elements, typically $d = \frac{\lambda}{2}$. The array response vector $\mathsf{a}_{\mathrm{r}}(\emptyset, \theta)$ for MS can also be obtained as above.

B- **Beamforming Designs**:

The small wavelength of signals in the mm wave frequency bands allows a large number of antenna elements (32 or more) to be packed in a small physical space [66] [71]. In order to generate a beam, one needs to control the phase of the signal that is transmitted or received by each antenna element to achieve a high antenna gain in certain direction and low gain in the other directions [71]. In addition, creating a beam between the transmitter and receiver can be done by obtaining the best received power signal or maximum data rate [6]. There are different beamforming designs in mm wave MIMO systems as described below.

1- Digital Beamforming

Although digital beamforming is hard to implement in practice [66], [72] as we will explain later, it shows its strength when it is combined with analog beamforming. In digital beamforming, all the signal processing is done at baseband [6], [66], [72], where each RF chain is connected to each antenna element, with $N_{RF} = N_t$ as shown in Figure 2.4 (a) [6]. In digital beamforming, the transmitter can transmit a single data stream or multiple data streams N_s to one receiver or spatially multiplexed into different receivers [72]. The precoding and combining matrices are optimum in digital beamforming which are created by using channel state information (CSI) **H** [66], but digital beamforming is very sensitive to imperfect CSI [72]. On the other hand, there are hardware constraints that make digital beamforming unfeasible in practice [6], [66]. These limitations, which are caused by large antenna elements, high carrier frequencies at mm wave bands, and large signal bandwidth are summarized as follows [6], [66]

- An RF chain to each antenna of a mm wave massive MIMO system increases the power consumption and the cost of the system.
- The very small separation between all antenna elements makes it hard to use a complete RF chain for each antenna.

Because of these hardware constraints, analog beamforming design and Hybrid Beamforming design have been proposed to comply with these constraints.

2- Analog Beamforming

In analog beamforming, all the signal processing is done in the RF domain [6], [66]. As shown in Figure 2.4 (b) [6], phase shifters are connected to each antenna element. In addition, all phase shifters are applied to a single RF chain to transmit a single data stream [72]. The phase shifter weights are controlled digitally to direct the beam to a certain direction based on the best received signal power and maximum data rate [66], [72].

Let us consider the downlink scenario, where BS transmits a symbol s to a user by using analog beamforming. In this case, we have only one analog beam $\mathrm{f_{RF}}$ directed to the user. The best beam gives the best received signal power at the user. Then, the transmitted vector y is given by [6]

$$\mathrm{y} = \mathrm{f_{RF}}\,\mathrm{s} \qquad (2.36)$$

where the analog precoder $\mathrm{f_{RF}}$ is implemented by limited quantized phase shifters [6], [66], [72]. As a result, $\mathrm{f_{RF}}$ is written as follows [6]

$$\mathrm{f_{RF}} = \frac{1}{\sqrt{N_{BS}}}\left[1, e^{j\emptyset_1}, \dots, e^{j\emptyset_{N_{BS}}}\right] \qquad (2.37)$$

which is equal to the array response vector in the strongest direction [73] and $\emptyset_n, n = 1, \dots.N_{BS}$ are designed to direct a beam in a certain direction maximizing the received signal power. Channel estimation can be exploited in analog beamforming by using beam training. Using a codebook of beam patterns with different resolutions is very common for mm wave channel estimation [6] [72].

Although analog beamforming meets the hardware constraint of mm wave massive MIMO systems and is not sensitive to the imperfect mm wave channel [72], it is limited by the quantized phase shifters controlled digitally [6] [66]. In addition, based on the results in [72], analog beamforming's performance is not achievable at NLOS and LOS in the case of increasing number of RF chains because of the problem of interference and phase shifter errors respectively. Therefore, an analog beamforming transmitter should support a single receiver with a single RF chain transmitting a single data stream. These drawbacks in analog beamforming have led to the need to design Hybrid beamforming.

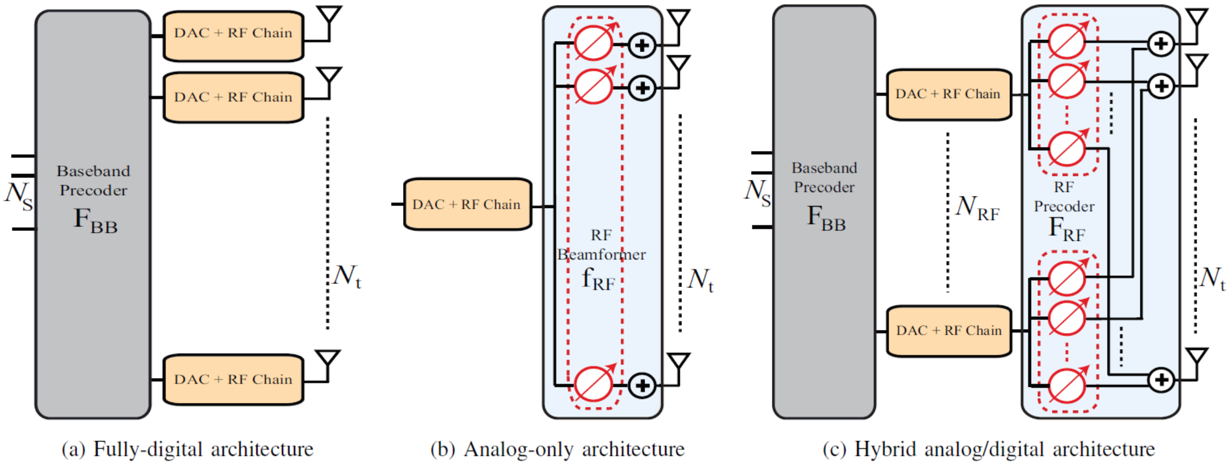

Figure 2. 4. This figure shows a transmitter having N_t antennas with a fully-digital, analog-only, or hybrid analog/digital architecture. In the hybrid architecture, $N_{RF} \ll N_t$ RF chains are deployed [8].

3- Hybrid Beamforming Solutions

Hybrid beamforming consists of both digital and analog beamforming design [8] [66]. Therefore, its design is implemented in the analog and digital domain and that offers a good performance with lower hardware complexity. In addition, its performance is close to the unconstrained digital beamforming [66]. As we can see in Figure 2.4 (c) [66], the hybrid precoding is implemented in the digital and analog domain giving $\mathbf{F_{BB}}$ (baseband precoder) and $\mathbf{F_{RF}}$ (RF precoder) respectively. In hybrid precoding, the number of RF chains is larger than one and smaller than the number of transmitter antennas N_t. This allows the transmitter to communicate with one receiver by multiple data streams or communicate with multiple receivers by a single data stream for $N_s \leq N_{RF} \ll N_t$ [66]. Therefore, hybrid beamforming achieves spatial multiplexing gains [66].

Consider the hybrid beamforming scheme implemented by BS and MS with N_{RF} RF chains as shown in Figure 2.5 [8]. Assume BS with N_{BS} antennas communicate with a single MS with N_{MS} antennas. The BS and MS communicate using N_s data streams with $N_s \leq N_{RF} \ll N_{BS}$ in the BS, and $N_s \leq N_{RF} \ll N_{MS}$ in the MS. The BS applies an N_{RF} x N_s baseband precoder $\mathbf{F_{BB}}$ followed by an N_{BS} x N_{RF} RF precoder $\mathbf{F_{RF}}$. As a result, N_{BS} x N_s hybrid precoder $\mathbf{F}$ is equal to $\mathbf{F_{RF}}\ \mathbf{F_{BB}}$. The hybrid combiner $\mathbf{W} \in C^{N_{MS}\,\mathrm{x}\,N_s}$ is also equal to $\mathbf{W}_{RF}\ \mathbf{W}_{BB}$ [8].

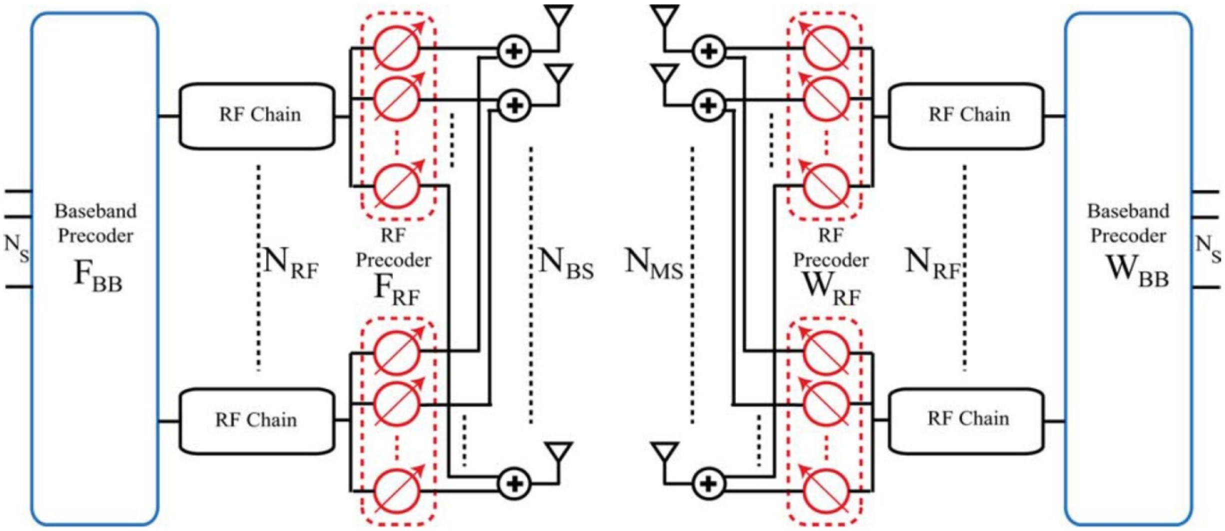

Figure 2. 5. Block diagram of BS-MS transceiver that uses RF and baseband beamformers at both ends [8].

The RF precoder/combiner is implemented by phase shifters, so they are normalized to have the same amplitude with different phase only such that $|\mathbf{F_{RF}}|^2 = \frac{1}{N_{BS}}$ and $|\mathbf{W_{RF}}|^2 = \frac{1}{N_{MS}}$ [8], where $|.|$ is element wise magnitude. In addition, the baseband precoder/combiner is normalized to satisfy the total power constraint such that $||\mathbf{F_{RF}}\mathbf{F_{BB}}||_F^2 = N_S$, and $||\mathbf{W_{RF}}\mathbf{W_{BB}}||_F^2 = N_S$ [8].

In this thesis, I consider a narrowband block-fading channel model. Then, the received signal y is combined at the MS as follows [8]

$$y = \mathbf{W^H}(\sqrt{P_r}\mathbf{HF}\mathrm{s} + \mathrm{n}) \qquad (2.38)$$

where $\mathbf{H}$ is the N_{MS} x N_{BS} mm wave channel matrix in the downlink transmission between BS and MS, $\mathrm{s} \in \mathbb{C}^{N_s \mathrm{x} 1}$ are the transmitted symbols, where $E[\mathrm{ss}^*] = \frac{1}{N_s} I_{N_s}$, where $\mathbf{I_{N_s}}$ is the $N_s\ by\ N_s$ identity matrix, P_r is the average received power, and n is a N_{MS} x 1 Gaussian noise vector with zero mean and variance σ^2. The uplink transmission can be done in the same way, with $\mathbf{H} \in \mathbb{C}^{N_{BS} \,\mathrm{X}\, N_{MS}}$ but switching the roles of the precoders and combiners.

In this thesis, we assume perfect channel state information at the BS and MS as explained later, and the sub-channels at the MS are given as follows

$$\mathbf{H_{eff}} = \mathbf{W^H HF} \qquad (2.39)$$

to detect the transmitted data streams using the ZF, MMSE detectors and sphere decoding as we will explain later. Note that the dimension of these sub-channels is much less than the original mm wave channel matrix **H**, depending on the rank of the mm wave channel. These sub-channels can be generated by MS using the mm wave channel.

Hybrid beamforming can achieve spatial multiplexing by transmitting multiple data streams [66]. That is why hybrid beamforming is preferred compared to analog and its performance is close to the unconstrained digital beamforming.

Finally, the spectral efficiency achieved by hybrid beamforming is given by [8]

$$R = log_2 \left| \mathbf{I_{N_s}} + \frac{P_r}{N_s} \mathbf{R_n^{-1} W^H H F F^H H^H W} \right| \qquad (2.40)$$

where $\mathbf{R_n} = \sigma^2\ \mathbf{W^H W}$ is the noise covariance matrix after the combining.

In this thesis, we analyze a single user mm wave system with multiple data streams and hybrid precoders/combiners, as we will describe next.

2.3.3. Single Data Stream and Single User by Using Analog Beamforming

When BS and MS use analog beamforming, they use the antenna array to communicate with each other by a single data stream. Assume $\mathrm{f_A}$ and $\mathrm{w_A}$ are the analog precoder and analog combiner respectively, then the receiver SNR is given by [6]

$$SNR = \frac{|\mathrm{w_A^* h f_A}|^2}{\sigma^2} \qquad (2.41)$$

Therefore, the goal of analog precoders/combiners is to maximize this received SNR. Because of the limited scattering characteristics in outdoor mm wave channels, it becomes easier to direct a beam with higher gain in a strongest/desired direction $\emptyset_s$.

It is found that making the beamforming weights match the array response vector in the desired direction is the best way to generate analog precoders/combiners [6]. That means, set $\mathrm{w_A} = \mathrm{a_{MS}(\theta_s)}$ and $\mathrm{f_A} = \mathrm{a_{BS}(\emptyset_s)}$ in the case of MS and BS respectively. The beampattern, pointed to the desired direction, with main-lobe gain G_{BS}, and side-lobe gain g_{BS} is shown in Figure 2.6 [6].

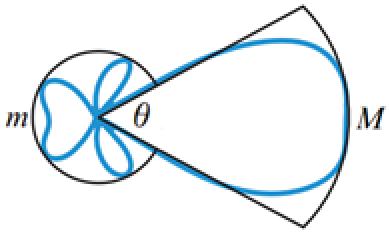

Figure 2. 6. Approximated sectored-pattern antenna model with main-lobe gain G_{BS}, and side-lobe g_{BS} [6].

2.3.4. Multiple Data Streams and Single User by Using Hybrid Design

Sparse hybrid precoders/combiners or SOMP based-designs maximize the spectral efficiency R as defined in (7), taking into account the RF precoders/combiners constraint and baseband power constraint [8]. The multiuser scenario is outside the scope of this thesis. As mentioned in the previous section, mm wave channels are sparse and low rank channels; thus, sparse hybrid precoders/combiners are built to approximate the unconstrained optimum digital precoder/combiner $\mathbf{F_{opt}}/\ \mathbf{W_{opt}}$ [8].

Designing the unconstrained optimum digital precoders/combiners, $\mathbf{F_{opt}}\ /\ \mathbf{W_{opt}}$, is usually done by using the channel singular value decomposition (SVD) defined by [2] [6] [8] [9]

$$\begin{aligned}[\mathbf{U}\,\mathbf{\Sigma}\,\mathbf{V^H}] &= \mathrm{SVD}(\mathbf{H}) \\ &= [\mathbf{U_1}\ \ \mathbf{U_2}]\begin{bmatrix}\mathbf{\Sigma_1} & \mathbf{0}\\ \mathbf{0} & \mathbf{\Sigma_2}\end{bmatrix}\begin{bmatrix}\mathbf{V_1^H}\\ \mathbf{V_2^H}\end{bmatrix} \qquad (2.42)\\ &= \mathbf{U_1}\,\mathbf{\Sigma_1}\mathbf{V_1^H} + \mathbf{U_2}\,\mathbf{\Sigma_2}\mathbf{V_2^H}\end{aligned}$$

where $\mathbf{\Sigma_1} = (\sigma_1, \dots, \sigma_{N_s})$ is a diagonal matrix with the largest N_s singular values of $\mathbf{H}$ in decreasing order. Taking the left N_s columns of semi-unitary matrices $\mathbf{U} \in \mathbb{C}^{N_{MS}\ X\ N_{MS}}$ and $\mathbf{V} \in \mathbb{C}^{N_{BS}\ X\ N_{BS}}$ yields

$$\mathbf{F_{opt}} = \mathbf{V_1} \in \mathbb{C}^{N_{BS}\,\mathrm{x}\,N_S} \qquad (2.43)$$

$$\mathbf{W_{opt}} = \mathbf{U_1^H} \in \mathbb{C}^{N_S\,\mathrm{x}\,N_{MS}}$$

which are the fully digital precoders and combiners, respectively. Therefore, the sparse hybrid precoder is found by approximating the unconstrained optimal precoder $\mathbf{F_{opt}}$ as follows [8]

$$(\mathbf{F_{BB}}) = \arg\min_{\tilde{\mathbf{F}}_{\mathbf{BB}}} \left\| \mathbf{F_{opt}} - \mathbf{A_{BS}} \mathbf{F_{BB}} \right\|_F \qquad (2.44)$$

$$\text{s.t.} \qquad \left\| \text{diag}(\mathbf{F_{BB}} \mathbf{F^H_{BB}}) \right\|_{\mathbf{0}} = N_{BS}^{RF}$$

$$\| \mathbf{A_{BS}} \mathbf{F_{BB}} \|_F^2 = N_S$$

where $\mathbf{A_{BS}}$ is the set of feasible quantized RF precoding codebooks with constant-magnitude entries which can be implemented in the RF circuitry using analog phase shifters. The design of RF precoding/combining codebooks $\mathbf{A_{BS}}$ have the same form of the array response of the mm wave channel and thus can be quantized in the azimuth and elevation angles with angular resolution L, where $L = 2^{N_\emptyset + N_\theta}$, and $N_\emptyset$ and N_θ are the numbers of azimuth and elevation quantization bits, respectively [8]. The analog combining codebook $\mathbf{A_{MS}}$ can be defined in the same way. However, to build the quantized RF precoding codebooks, some assumptions on the mm wave channel structure and array geometry have to be made. The sparsity constraint $\left\| \text{diag}\left(\mathbf{F_{BB}} \mathbf{F^H_{BB}}\right) \right\|_{\mathbf{0}} = N_{BS}^{RF}$ states that $\mathbf{F_{BB}}$ cannot have more than N_{BS}^{RF} non-zero rows, where $\|\mathrm{x}\|_{\mathbf{0}}$ is defined to be the number of nonzero entries in x. Equation (2.44) can be solved by the well-known concept of orthogonal matching pursuit (OMP) (see Appendix B) [8] and it is given in algorithm 2.1. It works by finding the vector in the RF precoding codebooks matrix $\mathbf{A_{BS}}$ along which the optimal precoder $\mathbf{F_{opt}}$ has the maximum projection. It then appends the selected column vector to the RF precoder $\mathbf{F_{RF}}$ matrix. After that, $\mathbf{F_{BB}}$ is calculated using the least squares solution and the contribution of the selected vector from $\mathbf{A_{BS}}$ is removed. The process continues until all N_{BS}^{RF} beamforming vectors have been selected from RF precoding codebooks matrix $\mathbf{A_{BS}}$. At the end of the N_{BS}^{RF} iterations, the RF precoding matrix $\mathbf{F_{RF}}$, and the baseband precoder $\mathbf{F_{BB}}$, which minimize $\left\| \mathbf{F_{opt}} - \mathbf{F_{RF}} \mathbf{F_{BB}} \right\|_F$, are found. Finally, $\mathbf{F_{BB}}$ is normalized so that the transmit power constraint is satisfied, and the sparse hybrid precoder $\mathbf{F} = \mathbf{F_{RF}} \mathbf{F_{BB}}$ is returned. The sparse hybrid combiner is designed by maximizing the data rate using $\mathbf{W}_{\mathbf{opt}}$ or minimizing the mean squared error between transmitted and received signals ($\mathbf{W}_{\text{MMSE}}$) [8].

The main drawback of the sparse hybrid design is the use of the set of feasible quantized RF precoding codebooks and the costly correlation operations. Moreover, the accuracy of the algorithm depends on the angular resolution L. Therefore, in this thesis we propose in Chapter 4 an algorithm to solve (2.44) without making any assumption on the array geometry or any other constraints such as the number of streams must be equal to the number of RF chains, and the baseband precoder/combiner is scaled unitary, while achieving a good spectral efficiency with low computational complexity compared to the other popular designs in the literature.

Algorithm 2. 1: Spatially Sparse Precoding via Orthogonal Matching Pursuit [8]

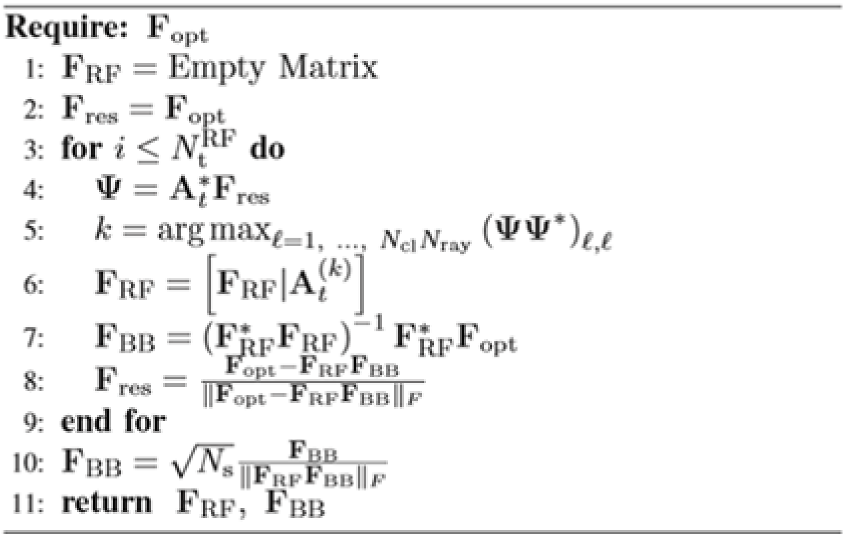

```
Require: $\mathbf{F}_{\text{opt}}$
$\mathbf{F}_{\text{RF}} = \text{Empty Matrix}$
$\mathbf{F}_{\text{res}} = \mathbf{F}_{\text{opt}}$
for $i \leq N_{\text{t}}^{\text{RF}}$ do
    $\mathbf{\Psi} = \mathbf{A}_{t}^{*}\mathbf{F}_{\text{res}}$
    $k = \arg\max_{\ell=1,\ \dots,\ N_{\text{cl}}N_{\text{ray}}} (\mathbf{\Psi}\mathbf{\Psi}^{*})_{\ell,\ell}$
    $\mathbf{F}_{\text{RF}} = \left[\mathbf{F}_{\text{RF}}|\mathbf{A}_{t}^{(k)}\right]$
    $\mathbf{F}_{\text{BB}} = \left(\mathbf{F}_{\text{RF}}^{*}\mathbf{F}_{\text{RF}}\right)^{-1}\mathbf{F}_{\text{RF}}^{*}\mathbf{F}_{\text{opt}}$
    $\mathbf{F}_{\text{res}} = \frac{\mathbf{F}_{\text{opt}}-\mathbf{F}_{\text{RF}}\mathbf{F}_{\text{BB}}}{\|\mathbf{F}_{\text{opt}}-\mathbf{F}_{\text{RF}}\mathbf{F}_{\text{BB}}\|_{F}}$
end for
$\mathbf{F}_{\text{BB}} = \sqrt{N_{\text{s}}}\frac{\mathbf{F}_{\text{BB}}}{\|\mathbf{F}_{\text{RF}}\mathbf{F}_{\text{BB}}\|_{F}}$
return $\mathbf{F}_{\text{RF}}$, $\mathbf{F}_{\text{BB}}$
```

CHAPTER 3: SPHERE DECODING AND SEMIDEFINITE RELAXATION FOR MILLIMETER WAVE MASSIVE MIMO

3.1 Proposed Method

In this chapter, we will explain in detail how to use the sphere decoding and semidefinite relaxation scheme for Millimeter Wave systems. First, we use the sparse hybrid precoders / combiners design shown in algorithm 2.1 with uniform planar arrays at both BS and MS to build the hybrid beamforming precoders and combiners [8]. After that, we use the ZF, MMSE detectors, sphere decoding, and semidefinite relaxation detections described in Chapter 2 to minimize the BER performance of mm wave massive MIMO systems.

In algorithm 2.1, we use the exact array response of the BS/MS that makes the mm wave channel as in (2.34). Note that in practice, we do not have the exact array response of mm wave channel, but we use a set of feasible quantized RF precoding codebooks with constant-magnitude entries which can be implemented in the RF circuitry using analog phase shifters.

Now, by approximating the hybrid beamforming precoders and combiners to the unconstrained optimal digital ones implemented by SVD, the received signal after combining is given as follows

$$\mathrm{y} = \sqrt{P_r}\mathbf{W^H}\mathbf{H}\mathbf{F}\mathrm{s} + \mathbf{W^H}\mathrm{n} \qquad (3.1)$$

$$\mathrm{y} \approx \sqrt{P_r}\mathbf{U_1^H}\mathbf{H}\mathbf{V_1}\mathrm{s} + \mathbf{U_1^H}\mathrm{n}$$

$$\mathrm{y} \approx \sqrt{P_r}\mathbf{\Sigma_1}\mathrm{s} + \mathbf{U_1^H}\mathrm{n}$$

For ZF, and MMSE detectors, it is known that for mm wave systems with perfect CSI, the effective channel given in (2.39) can be approximated by using the UPA hybrid precoder/combiner as follows

$$\mathbf{H_{efe}} = \mathbf{W^H H F} \approx \mathbf{\Sigma_1} \in \mathbb{C}^{N_S \, \mathrm{x} \, N_S} \qquad (3.2)$$

Since the dimension of $\mathbf{\Sigma_1}$is N_S X N_S , the ZF and MMSE detectors are implemented as follows

$$\mathbf{W_{ZF}} = (\mathbf{\Sigma_1}\ )^{-1} \quad \text{ZF Detector} \qquad (3.3)$$

$$\mathbf{W_{MMSE}} = (\mathbf{\Sigma_1}^{\mathrm{H}}\mathbf{\Sigma_1} + \sigma^2 \mathrm{I_{Nr}})^{-1}\,\mathbf{\Sigma_1}^{\mathrm{H}} \quad \text{MMSE Detector} \qquad (3.4)$$

where $\sigma^2 = P_r/SNR$. Thus, the transmitted symbols $\hat{s}$ can be detected by multiplying y the received signal in (3.1) with the linear detection matrix $\mathbf{W_{ZF}}$ and $\mathbf{W_{MMSE}} \in \mathbb{C}^{N_s\, X\, N_s}$ as follows

$$\hat{\mathrm{s}} = \mathbf{W_{ZF}}\mathrm{y} \qquad (3.5)$$

$$\hat{\mathrm{s}} = \mathbf{W_{MMSE}}\mathrm{y} \qquad (3.6)$$

The sphere decoding described in section 2.1.1.3 is implemented by using the diagonal $\mathbf{\Sigma_1}$ matrix to find the solution ŝ with the smallest Euclidean distance from the received signal within the sphere of the dimension of the transmitted vector, which means

$$\|\mathrm{y} - \mathbf{\Sigma_1}\mathrm{s}\|^2 \ \le\ d^2 \qquad (3.7)$$

For the semidefinite relaxation scheme, first we use the real-valued variables of (3.1) as follows

$$\begin{bmatrix}\mathrm{Re}(y)\\ \mathrm{Im}(\mathrm{y})\end{bmatrix} \approx \begin{bmatrix}\mathrm{Re}\left(\sqrt{P_r}\mathbf{\Sigma_1}\right) & -\,\mathrm{Im}(\sqrt{P_r}\mathbf{\Sigma_1})\\ \mathrm{Im}\left(\sqrt{P_r}\mathbf{\Sigma_1}\right) & \mathrm{Re}(\sqrt{P_r}\mathbf{\Sigma_1})\end{bmatrix}\begin{bmatrix}\mathrm{Re(s)}\\ \mathrm{Im(s)}\end{bmatrix} + \begin{bmatrix}\mathrm{Re}\left(\mathbf{U_1^H}n\ \right)\\ \mathrm{Im}\left(\mathbf{U_1^H}n\ \right)\end{bmatrix} \qquad (3.8)$$

Then we use the semidefinite algorithm described in section 2.1.1.2 which is solved using the SeDuMi package [56] to find the solution $\hat{s}$ of the transmitted symbols.

3.2 Performance Evaluation of ZF, MMSE, Sphere Decoding, and semidefinite relaxation for Multiple Data Streams $N_S = 3$.

In this section, we present the error performance of the ZF, MMSE, sphere decoding algorithms, and semidefinite relaxation detections for an outdoor hybrid beamforming mm wave massive MIMO system. For all detection algorithms, 16-QAM, and QPSK modulation schemes are used without any coding scheme. Also, for all cases, the mm wave channel remains constant during the transmission of one block of data.

In these simulations, we use the system architecture presented in Fig. 2.5. We consider the case where there is only one BS and one MS at a distance of 100 meters. The spacing between antenna elements is equal to $\lambda/2$. The system is assumed to operate at a 28 GHz carrier frequency in an outdoor scenario with a path loss exponent $n = 3.4$. The channel model is described in (2.34), with $\overline{\mathrm{P}_{\alpha,\iota}} = 1$ for all clusters, and the number of paths $L = 5$ which is equivalent to 5 clusters with an angular spread of zero for all simulations. The azimuth and elevation angles AoAs/AoDs of the rays within a cluster are assumed to be randomly Laplacian distributed. The AoAs/AoDs azimuths and elevations of the cluster means are assumed to be uniformly distributed. We use the AoD/AoA beamforming codebooks (exact array response of mm wave channel) at the BSs and MSs respectively for the sparse hybrid design. The SNR in all the plots is defined as $SNR = P_r/\sigma^2$. We assume perfect CSI at the BS and MS. For fairness, the same total power constraint is enforced on all precoding/combining solutions.

We use the sparse hybrid precoder to precode the data streams in the downlink transmission and the hybrid combiner to combine the received signal at the receiver side assuming a mm wave channel with perfect CSI at the BS and MS. We then use the effective channels described in (3.2) with the ZF, MMSE, sphere decoding algorithms, and semidefinite relaxation detections to detect the transmitted data streams N_s and then we show the simulation results of BER.

Fig. 3.1 displays the BER performance achieved in a 16-QAM, 256×16 UPAs system with $N_{RF}^{BS} = N_{RF}^{MS}$ =3 RF chains and $N_s = 3$ with the exact array response of mm wave channel for sparse hybrid design. In this simulation, we compare the BER performance of the SDR detector with that of the sphere decoding instead of the ML detector. For 16-QAM, it is much more complex to use the ML detector ($2^{4 \times 3}$ = 4096 vectors). In addition, the radius of SD varies depending on the SNR and is calculated from (3.7) by using the ZF detector. Fig. 3.1 shows that the SDR detector performs better than the ZF and MMSE detectors over the whole range of SNR. The MMSE detector performs a little bit better than the ZF detector over the entire range of SNR because it is taking into consideration the effect of noise. A bit error probability of 10^{-3} can be obtained with SNR $= -1$ dB using the SDR detector, whereas the ZF and MMSE detectors need about 5 dB to obtain the same BER, which represents a gain of 6 dB. The gain is even larger at a lower BER.

Although the SD detector outperforms the SDR, ZF, and MMSE detectors in the high range of SNR, its complexity increases exponentially with the number of data streams and with the modulation order, making it impractical and more complex than the other detectors.

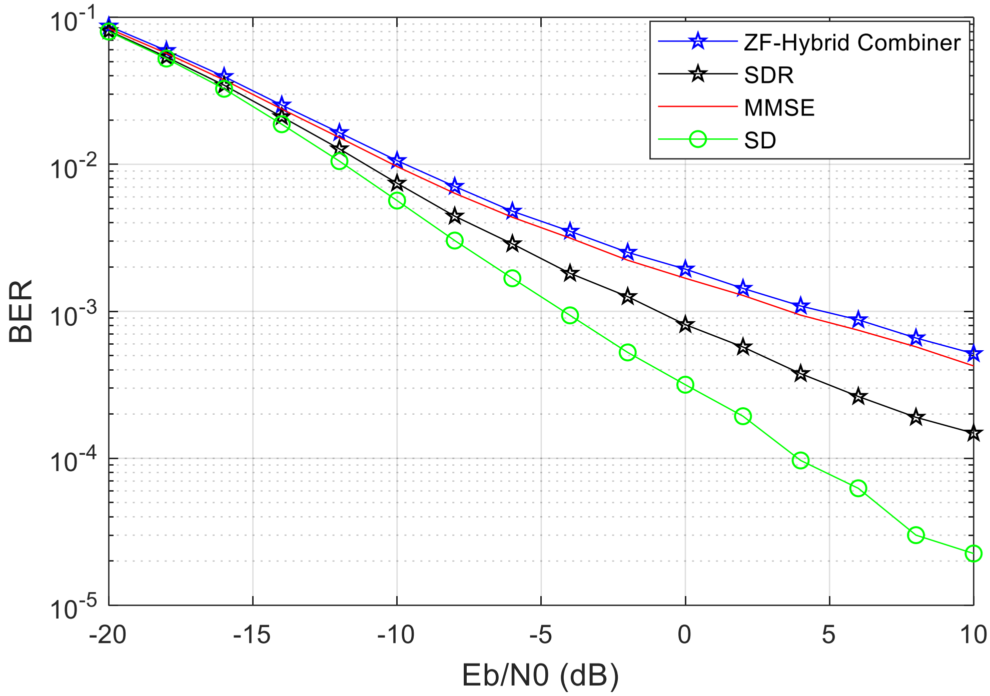

Figure 3. 1. BER performance for uncoded 16QAM single-cell hybrid beamforming mm wave massive MIMO system for $N_{BS} = 256$ and $N_{MS} = 16$ with 3 and 3 RF chains respectively, and $N_S = 3$ by using the exact array response of mm wave channel.

Fig. 3.2 shows the performance achieved in a QPSK 256×16 UPAs system with $N_{RF}^{BS} = N_{RF}^{MS}$ =3 RF chains and $N_s = 3$ with the exact array response of mm wave channel for sparse hybrid design. In this simulation, we compare the performance of the SDR detector with that of the ML detector because the number of possible vectors in the ML search ($2^{2 \times 3}$ = 64 vectors) is acceptable for QPSK modulation. Fig. 3.2 shows that the SDR detector still performs better than the ZF and MMSE detectors over the whole range of SNR . A bit error probability of 10^{-3}can be obtained with SNR $= -8$ dB using the SDR detector, whereas the MMSE and ZF detectors need about 0 dB to obtain the same BER, which represents a significant gain of 8 dB for the SDR detector. Furthermore, it can be seen that the performance of the SDR detector , SD method, and ML detector is the same over the entire range of SNR as expected for QPSK [53] [54]

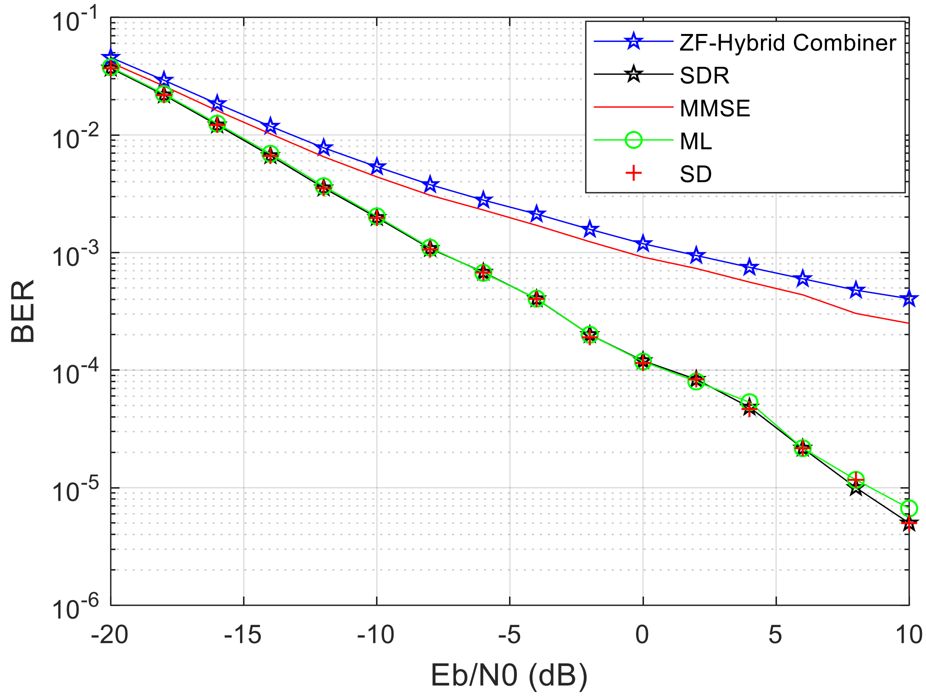

Figure 3. 2. BER performance for uncoded QPSK single-cell hybrid beamforming mm wave massive MIMO system for $N_{BS} = 256$ and $N_{MS} = 16$ with 3 and 3 RF chains respectively, and $N_S = 3$ by using the exact array response of mm wave channel.

Fig. 3.3 illustrates the average simulation running time of all detectors for different data streams in a 16-QAM, 256 x 16 UPAs system with different $N_{RF}^{BS} = N_{RF}^{MS} = N_s$, and different SNRs. All the results are obtained using the same computer with 10^6 iterations. The computer has i7 processor and the memory size is 8 gigabytes. For any SNR, we can see that the SDR detector requires a longer running time than the ZF, and MMSE detectors. As mentioned before, the complexity of sphere decoding increases with the number of data streams and modulation order; thus, sphere decoding requires a longer time than the SDR detector at -20 dB. However, the speed of sphere decoding (SD) increases in the high SNR region. Moreover, it is clear that the average running time of the SDR detector is essentially independent of SNR. Hence, SDR detection is a good alternative to sphere decoding for low or moderate SNRs, but it is outperformed by SD at high SNRs, where the detection problem becomes easier for SD.

The running time of SDR detector depends only on the constellation size and the number of data streams. Because we considered only data streams $N_s = 6$ up to 8, the running time of the SDR detector just changed slightly; the complexity would become higher with a much larger number of data streams and large constellation size.

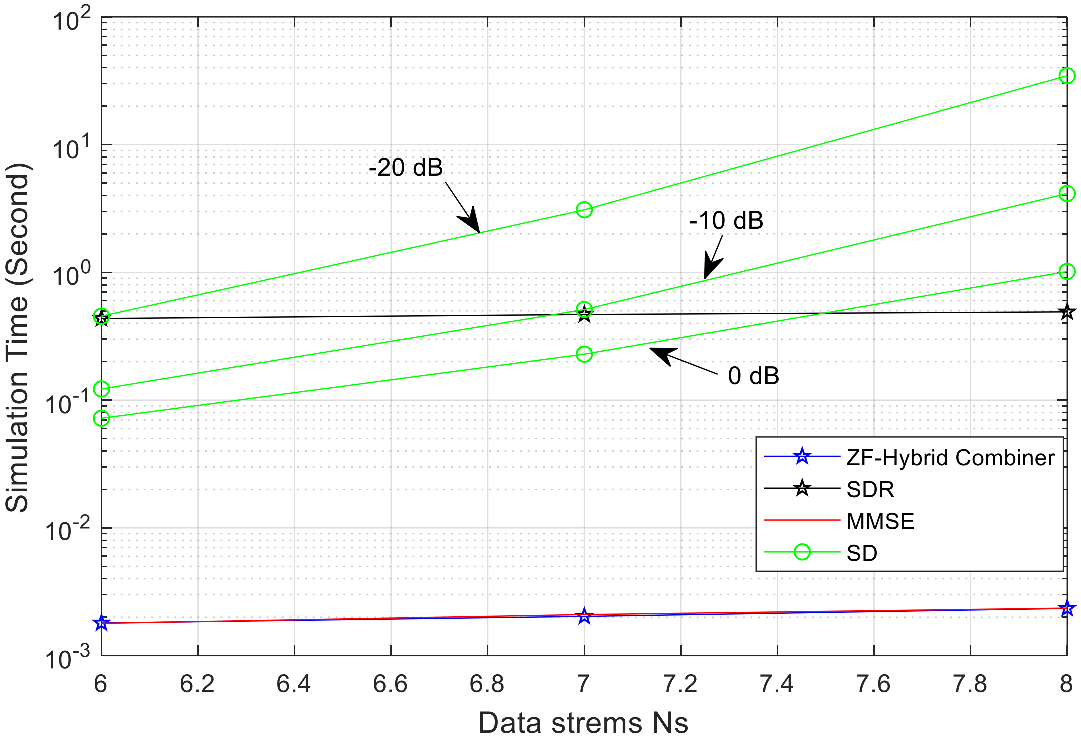

Figure 3. 3. Average running time for uncoded 16QAM single-cell hybrid beamforming mm Wave massive MIMO system for different SNRs and data streams, with $N_{BS} = 256$, $N_{MS} = 16$ and $N_{RF}^{BS} = N_{RF}^{MS}=N_S$, using the exact array response of mm Wave channel.

Table 3.1 shows the simulation times in seconds in a system similar to the one used in Fig. 3.2, but the radius of the SD algorithm is efficiently selected to have the smallest probability of error and accepted simulation time compared to the other detectors. All the results are obtained using the same computer with 10^6 iterations for different values of SNR. The computer has i7 processor and a memory size of 8 gigabytes. It is clear from Table 3.1 that the SD simulation time is smaller than the ML detector and close to the ZF and MMSE detectors for small number of data streams

$N_S = 3$; also, SD achieves the same bit error probability as the ML detector and a smaller probability than the ZF and MMSE detectors.

Table 3. 1 Simulation Times for the Three Detectors

QPSK Modulation				
SNR (dB)	SD radius	Detector	Simulation time in seconds	Bit error probability
-10	50	MMSE	6.71 X 10^{3}	4.4 X 10^{-3}
		ZF	6.73 X 10^{3}	5.2 X 10^{-3}
		ML	7.21 X 10^{3}	2 X 10^{-3}
		SD	6.87 X 10^{3}	3 X 10^{-3}
0	9	MMSE	6.71 X 10^{3}	9.3 X 10^{-4}
		ZF	6.73 X 10^{3}	1.2 X 10^{-3}
		ML	7.20 X 10^{3}	1.2 X 10^{-4}
		SD	6.86 X 10^{3}	1.2 X 10^{-4}
10	1	MMSE	6.70 X 10^{3}	2.4 X 10^{-4}
		ZF	6.73 X 10^{3}	3.2 X 10^{-4}
		ML	7.20 X 10^{3}	5.7 X 10^{-6}
		SD	6.84 X 10^{3}	5.8 X 10^{-6}

3.3 Summary

In this chapter, SDR detection allows a complexity vs. performance trade-off for mm awve massive MIMO. The SDR detector is much less complex than the SD and ML detectors for a large number of data streams or high modulation order, especially for low SNR regions, while yielding a BER between that of ML and ZF or MMSE. Moreover, for a small number of data streams and low modulation order, the SD achieves the same bit error probability as the ML detector and with low complexity which is close to the complexity of the linear detection schemes such as ZF and MMSE.

CHAPTER 4: PROPOSED LOW COMPLEXITY HYBRID PRECODING AND COMBINING FOR MILLIMETER WAVE SYSTEMS

4.1 Proposed Method

In this section, we propose a low complexity-precoding algorithm with equal power allocation per stream. In addition, we do not assume any constraint on the optimization problem, which is related to (2.44). The derivation of the combiner is similar. Assume BS with N_{BS} antennas communicate with a single MS with N_{MS} antennas. We note that the optimal unconstrained semi-unitary precoder for $\mathbf{H}$ is simply given by $\mathbf{F_{opt}} = \mathbf{V_1}$. Also, we need the hybrid precoder $\mathbf{F_{RF}}\mathbf{F_{BB}}$ to be sufficiently "close" to the optimal precoder $\mathbf{V_1}$ by using its digital precoder to construct linear combinations of the RF precoder vectors [8]. By formulating an optimization problem, we first need to find the baseband precoder $\mathbf{F_{BB}}$ that minimizes the Euclidean distance by using the initialization of the proposed RF precoder, which is calculated by taking the first N_s columns from $\mathbf{F_{opt}}$ and then normalizing them such that each entry has constant magnitude, i.e., $\mathbf{F_{RF}} = \mathbf{F_{opt}} \oslash \left(\left|\mathbf{F_{opt}}\right| \sqrt{N_{BS}}\right)$, where $\oslash$ stands for element-wise division. One should note that the element-wise normalization of $\mathbf{F_{RF}}$ satisfies the normalization constraint $\left|[\mathbf{F_{RF}}]_{i,j}\right|^2 = \frac{1}{N_{BS}}$ [8]. We then find the RF precoder $\mathbf{F_{RF}}$ such that the hybrid precoder $\mathbf{F_{RF}}\mathbf{F_{BB}}$ is sufficiently "close" to the optimal unconstrained digital precoder $\mathbf{V_1}$. Specifically, we propose an iterative solution to the optimization problem (2.44). First, we would like to solve the following optimization problem, which is related to (2.44):

$$(\mathbf{F_{BB}}) = \arg\min_{\mathbf{F_{BB}}} \left\|\mathbf{F_{opt}} - \mathbf{F_{RF}}\mathbf{F_{BB}}\right\|_F^2 \qquad (4.1)$$

The objective function can be expanded as follows

$$\left\|\mathbf{F_{opt}} - \mathbf{F_{RF}}\mathbf{F_{BB}}\right\|_F^2$$

$$= \mathrm{tr}\left(\mathbf{F_{opt}^H}\mathbf{F_{opt}}\right) - 2\mathrm{tr}\left(\mathbf{F_{opt}^H}\mathbf{F_{RF}}\mathbf{F_{BB}}\right) + \mathrm{tr}(\mathbf{F_{BB}^H}\mathbf{F_{RF}^H}\mathbf{F_{RF}}\mathbf{F_{BB}})$$

$$= N_S - 2\mathrm{tr}\left(\mathbf{F_{opt}^H}\mathbf{F_{RF}}\mathbf{F_{BB}}\right) + \mathrm{tr}(\mathbf{F_{BB}^H}\mathbf{F_{RF}^H}\mathbf{F_{RF}}\mathbf{F_{BB}}) \qquad (4.2)$$

To minimize over $\mathbf{F_{BB}}$, we set the derivative of (4.2) with respect to $\mathbf{F_{BB}}$ equal to zero, which yields the following minimized proposed baseband precoder $\mathbf{F_{BB}}$ (least squares solution)

$$\mathbf{F_{BB}} = \left(\mathbf{F_{RF}^H}\mathbf{F_{RF}}\right)^{-\mathbf{1}}\mathbf{F_{RF}^H}\mathbf{F_{opt}} \qquad (4.3)$$

Then, we keep $\mathbf{F_{BB}}$ fixed and solve the same optimization problem but now minimizing over $\mathbf{F_{RF}}$

$$(\mathbf{F_{RF}}) = \arg\min_{\mathbf{F_{RF}}}\left\|\mathbf{F_{opt}} - \mathbf{F_{RF}}\mathbf{F_{BB}}\right\|_F^2 \qquad (4.4)$$

Similarly to (4.1), expanding the objective function yields

$$\left\|\mathbf{F_{opt}} - \mathbf{F_{RF}}\mathbf{F_{BB}}\right\|_F^2$$

$$= N_S - 2\mathrm{tr}\left(\mathbf{F_{opt}^H}\mathbf{F_{RF}}\mathbf{F_{BB}}\right) + \mathrm{tr}(\mathbf{F_{BB}^H}\mathbf{F_{RF}^H}\mathbf{F_{RF}}\mathbf{F_{BB}}) \qquad (4.5)$$

We again set the derivative of (4.5) with respect to $\mathbf{F_{RF}}$ equal to zero, which yields the following

$$\mathbf{F_{RF}}\mathbf{F_{BB}}\mathbf{F_{BB}^H} = \mathbf{F_{opt}}\mathbf{F_{BB}^H} \qquad (4.6)$$

The problem in (4.6) is that $\mathbf{F_{BB}}\mathbf{F_{BB}^H}$ cannot be inverted when $N_S < N_{RF}^{BS}$. Thus, to solve it we add $\mathbf{F_{RF}}$ to both sides of (4.6) such that

$$\mathbf{F_{RF}} = \mathbf{F_{opt}}\mathbf{F_{BB}^H} - \mathbf{F_{RF}}\mathbf{F_{BB}}\mathbf{F_{BB}^H} + \mathbf{F_{RF}}$$

$$\mathbf{F_{RF}} = (\mathbf{F_{opt}} - \mathbf{F_{RF}}\mathbf{F_{BB}})\mathbf{F_{BB}^H} + \mathbf{F_{RF}}$$

$$\mathbf{F_{RF}} = \mathbf{F_{res}}\mathbf{F_{BB}^H} + \mathbf{F_{RF}} \qquad (4.7)$$

where the residual precoding matrix $\mathbf{F_{res}} = \mathbf{F_{opt}}$ - $\mathbf{F_{RF}}\mathbf{F_{BB}}$. Equation (4.7) yields an iterative solution for $\mathbf{F_{RF}}$ such that in the current iteration, the updated $\mathbf{F_{RF}}$ is equal to $\mathbf{F_{RF}}$ from the previous iteration plus $\mathbf{F_{res}}\mathbf{F_{BB}^{H}}$. Moreover, (4.7) satisfies the property of the gradient descent method (see Appendix A) with a step size equal to one. Thus, $\mathbf{F_{RF}}$ is guaranteed to converge to a feasible local optimal solution. This solution can also be applied when $N_S = N_{RF}^{BS}$. Note that when $N_S < N_{RF}^{BS}$, we need to complete the N_{BS} x N_{RF}^{BS} $\mathbf{F_{RF}}$ after the initialization. In each iteration, we add a column to $\mathbf{F_{RF}}$ which leads to the highest reduction of the residual. This column can be selected from the basis of the range of the residual, which is the element-wise normalization of the first singular vector of the residual.

The pseudo-code for the proposed hybrid precoder $\mathbf{F^{P}}$ solution is given in Algorithm 4.1. In a mm wave system using the hybrid precoding design, the BS or MS can support up to N_{RF} data streams, i.e., $N_S \leq \min(N_{RF}^{BS}, N_{RF}^{MS})$ [2] [3] [6] [9], and [8]. The inputs of the algorithm are $\mathbf{F_{opt}} \in \mathbb{C}^{N_{BS} \times N_S}$ and the maximum number of iterations K, where $K \geq N_{RF}^{BS}$ - N_S when $N_S < N_{RF}^{BS}$, in order to calculate the N_{BS} x N_{RF}^{BS} $\mathbf{F_{RF}}$ matrix, and $K \geq 1$ when $N_{RF}^{BS} = N_S$. In the general case of $N_S \geq 1$ where $N_S \leq N_{RF}^{BS}$, the algorithm starts by initializing $\mathbf{F_{RF}}$ with the element-wise normalization of the first N_s columns of $\mathbf{F_{opt}}$ i.e., $\mathbf{F_{RF}} = \mathbf{F_{opt}} \oslash \left(|\mathbf{F_{opt}}|\sqrt{N_{BS}}\right)$. Then, $\mathbf{F_{BB}}$ is computed using least squares in step 2. After that, the algorithm proceeds to calculate the residual precoding matrix $\mathbf{F_{res}}$ and the proposed RF precoder $\mathbf{F_{RF}}$ in steps 3 and 4 respectively. Step 5 ensures that the proposed RF precoder $\mathbf{F_{RF}}$ is satisfied exactly with constant-magnitude entries which can be applied at RF using analog phase shifters. In steps 7 and 8, when $N_S < N_{RF}^{BS}$, we need to complete the N_{BS} x N_{RF}^{BS} $\mathbf{F_{RF}}$, which can be done by adding the element-wise normalization of the first singular vector of the residual matrix $\mathbf{F_{res}}$ to $\mathbf{F_{RF}}$. After K iterations the process is completed and the algorithm will find the N_{BS} x N_{RF}^{BS} proposed RF precoding matrix $\mathbf{F_{RF}}$ and the optimal N_{RF}^{BS}x N_S baseband precoder $\mathbf{F_{BB}}$ such that $\left\|\mathbf{F_{opt}} - \mathbf{F_{RF}}\mathbf{F_{BB}}\right\|_F$ is minimized. In steps 12 and 13, we ensure that the transmit power constraint is satisfied and return the proposed hybrid precoder $\mathbf{F^P} = \mathbf{F_{RF}}\mathbf{F_{BB}}$. The proposed hybrid combiner $\mathbf{W_{RF}^P}$ can be calculated in the same way.

Remark 1 - Convergence of the Proposed Hybrid Precoder to Local Minimum Points: Note that when $N_S = N_{\boldsymbol{RF}}^{\boldsymbol{BS}}$ or $N_S < N_{\boldsymbol{RF}}^{\boldsymbol{BS}}$, $\mathbf{F_{BB}}$ is a square matrix that is approximately unitary $\mathbf{F_{BB}^H}\mathbf{F_{BB}} \approx \mathbf{F_{BB}}\mathbf{F_{BB}^H} \approx \mathbf{I_{N_S}}$ or a non-square matrix that is approximately semi-unitary $\mathbf{F_{BB}^H}\mathbf{F_{BB}} \approx \mathbf{I_{N_S}}$,respectively [8], [28]. Thus, each iteration in Algorithm 4.1 minimizes the objective function $\left\|\mathbf{F_{opt}} - \mathbf{F_{RF}}\mathbf{F_{BB}}\right\|_F$ and the error term decreases monotonically with each iteration. Since the objective function has a lower bound, the proposed method must converge to local optimum points. In Section 4.2, simulations results will confirm that the objective function decreases monotonically with each iteration, and it tends asymptotically to its lower bound.

```
Algorithm 4. 1 : Proposed Hybrid Precoding.

Input: The optimum unconstrained solution $\mathbf{F_{opt}} \in C^{N_{BS} \text{x} N_S}$ and the maximum number of iterations $K$.
Output: Analog $\mathbf{F_{RF}} \in C^{N_{BS} \text{x} N_{\boldsymbol{RF}}^{\boldsymbol{BS}}}$ with the element-wise normalization and baseband $\mathbf{F_{BB}} \in C^{N_{\mathbf{RF}}^{\mathbf{BS}} \text{x} N_S}$ such that $\left\|\mathbf{F_{opt}} - \mathbf{F^P}\right\|_F$ is reduced and $\left\|\mathbf{F^P}\right\|_F^2 = N_S$, where $\mathbf{F^P} = \mathbf{F_{RF}}\mathbf{F_{BB}}$.
```

```
Initialization: analog precoder $\mathbf{F_{RF}} = \mathbf{F_{opt}} \oslash \left(\left|\mathbf{F_{opt}}\right|\sqrt{N_{BS}}\right)$.
for $i = 1{:}K$ do
    Update: $\mathbf{F_{BB}} = \left(\mathbf{F_{RF}^H F_{RF}}\right)^{-\mathbf{1}} \mathbf{F_{RF}^H F_{opt}}$
    Update the residual: $\mathbf{F_{res}} = \mathbf{F_{opt}}$ - $\mathbf{F_{RF} F_{BB}}$
    Update: $\mathbf{F_{RF}} = \alpha \mathbf{F_{res} F_{BB}^H} + \mathbf{F_{RF}}$
    Element-Wise Normalization:
        $\mathbf{F_{RF}} = \mathbf{F_{RF}} \oslash \left(|\mathbf{F_{RF}}|\sqrt{N_{BS}}\right)$
    If $i \le N_{\boldsymbol{RF}}^{\boldsymbol{BS}}$ - $N_S$
        $\mathbf{F_{res}} = \mathbf{U}\,\boldsymbol{\Sigma}\,\mathbf{V^H}$
        Append the element-wise normalization of the first vector of U as a new column to
            $\mathbf{F_{RF}}$: $\mathbf{F_{RF}} = [\ \mathbf{F_{RF}}\ \ (\mathbf{U})_1 \oslash \left(|(\mathbf{U})_1|\sqrt{N_{BS}}\right)\ ]$
    end if
end for
$\mathbf{F_{BB}} = \left(\mathbf{F_{RF}^H F_{RF}}\right)^{-\mathbf{1}} \mathbf{F_{RF}^H F_{opt}}$
$\mathbf{F_{BB}} = \sqrt{N_S}\,\frac{\mathbf{F_{BB}}}{\left\|\mathbf{F_{RF}^P F_{BB}}\right\|_F}$
return $\mathbf{F^P} = \mathbf{F_{RF} F_{BB}}$
```

4.2 Simulation Results

This section presents the numerical results to show the performance advantages of the proposed hybrid precoders /combiners implemented as described in Algorithm 4.1. Specifically, we present the BER performance of the ZF, MMSE, ML, and sphere decoding. For all detection algorithms, the QPSK and 16-QAM modulation schemes are used without error-control coding. In addition, for all cases, the mm wave channel remains constant during the transmission of one block of data.

In these simulations, we use the system architecture presented in Fig. 2.5. We consider the case where there is only one BS and one MS at a distance of 100 meters. The spacing between antenna elements is equal to $\lambda/2$. The system is assumed to operate at a 28 GHz carrier frequency in an outdoor scenario with a path loss exponent $n = 3.4$. The channel model is described in (2.34), with $\overline{\mathrm{P}_{\alpha,\iota}} = 1$ for all clusters. The azimuth and elevation angles AoAs/AoDs of the rays within a cluster are assumed to be randomly Laplacian distributed. The AoAs/AoDs azimuths and elevations of the cluster means are assumed to be uniformly distributed. We use the AoD/AoA beamforming codebooks (exact array response of mm wave channel) at the BSs and MSs respectively for the sparse hybrid design [8]. The SNR in all the plots is defined as $SNR = P_r/\sigma^2$. We assume perfect CSI at the BS and MS. For fairness, the same total power constraint is enforced on all precoding/combining solutions.

In Fig. 4.1 and Fig. 4.2, the channel model has five paths which is equivalent to 5 clusters with an angular spread of zero. The AoAs/AoDs azimuths of the cluster means are assumed to be uniformly distributed in$[0,2\pi]$, while their AoAs/AoDs elevations are uniformly distributed in $[\frac{-\pi}{2},\frac{\pi}{2}]$. In Fig. 4.1, we evaluate the BER performance of the ZF, MMSE, and sphere decoding algorithms for a 16 QAM 256 x 16 UPAs mm wave systems with $N_{RF}^{BS} = N_{RF}^{MS}$ =3 RF chains and $N_S = 3$ data streams. Fig. 4.1 shows that the BER performance is significantly improved by using the proposed hybrid precoding/combining design with $K = 6$ compared to the BER performance of the sparse hybrid precoding/combining designs [8], and [47] [48]. Also, the performance gap between the sphere decoding algorithm and the ZF and MMSE detectors with the proposed hybrid precoding/combining over the whole range of SNR is considerably reduced compared to the performance gap of the same schemes with the sparse hybrid precoding/combining designs [8], and [47] [48]. The sphere decoding algorithm, ZF and MMSE detectors perform similarly over the whole range of SNR for the proposed hybrid beamforming design, but the ZF and MMSE detectors perform significantly worse than the SD when the sparse hybrid beamformer is used, especially for a BER below 10^{-2}. A bit error probability of 10^{-5} can be obtained with $SNR = 4\ dB$ using sphere decoding with the proposed hybrid precoding/combining design, whereas the ZF and MMSE detectors with the proposed hybrid precoding/combining design need about 6 dB to obtain the same BER, which represents a small difference of 2 dB. However, with the sparse hybrid precoding/combining design, the difference between sphere decoding and ZF or MMSE exceeds 15 dB to obtain a BER of 10^{-4}. Hence, the proposed beamformer allows the use of the ZF or MMSE detectors, which have a significantly lower computational complexity than SD [47] [48], without incurring the performance penalty observed with the sparse hybrid precoder/combiner.

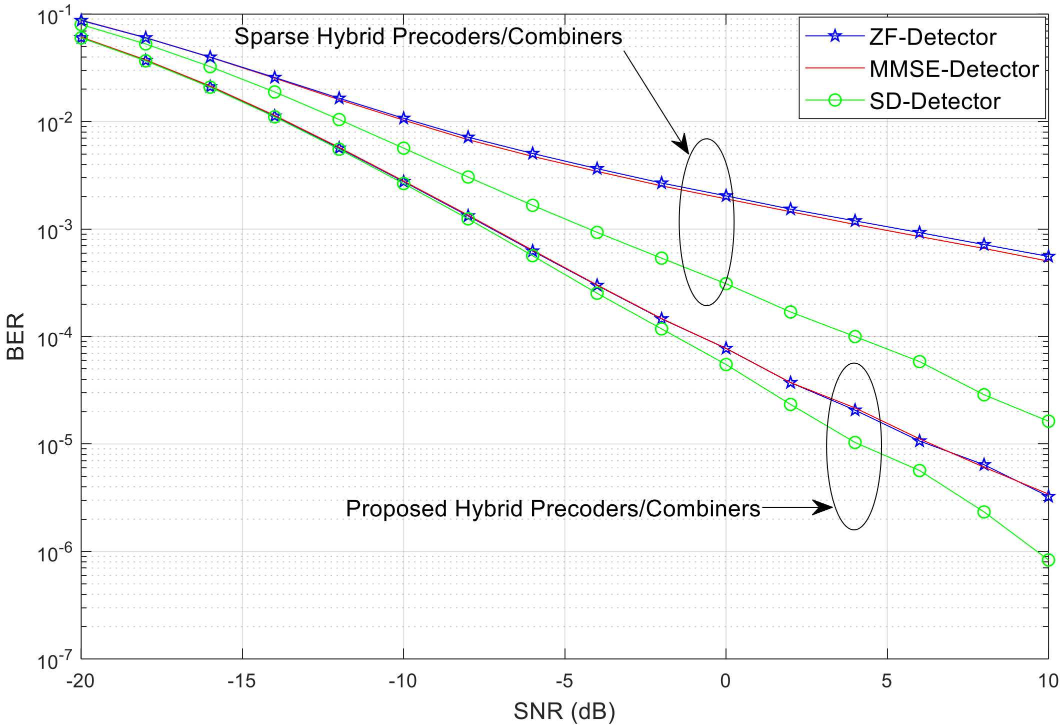

Figure 4. 1 BER performance for uncoded 16 QAM single-cell proposed hybrid precoders/combiners with $K = 6$ compared to the sparse hybrid precoders/combiners [8], and [47] [48] in mm wave systems for $N_{BS} = 256$ and $N_{MS} = 16$ with 3 and 3 RF chains respectively, and $N_S = 3$.

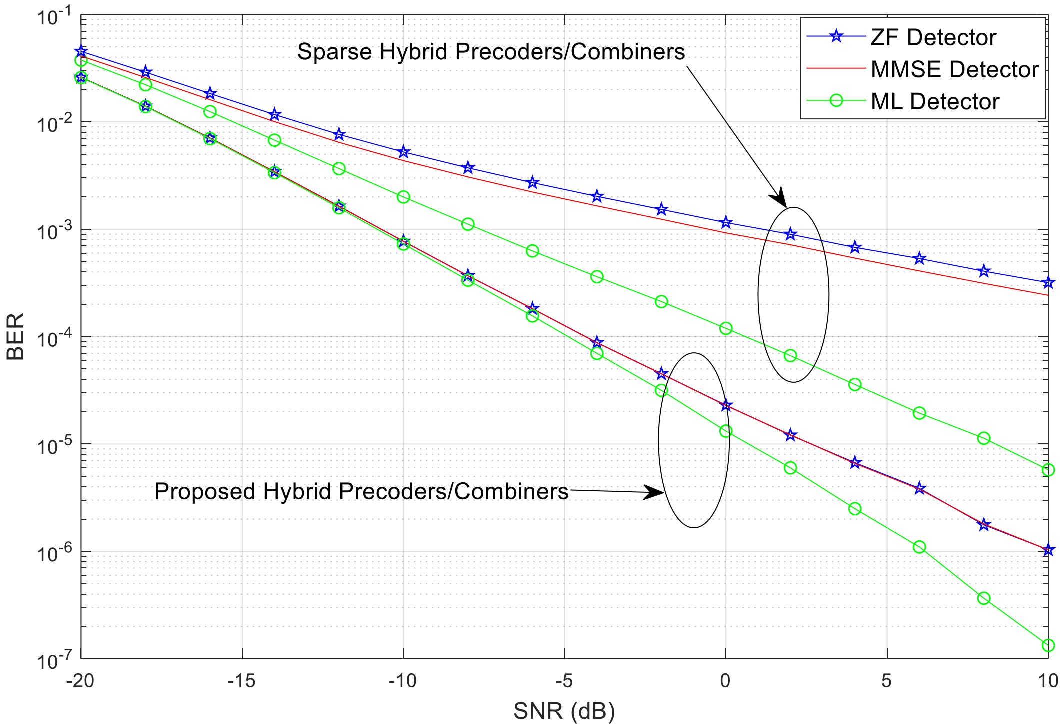

Figure 4. 2. BER performance for uncoded QPSK single-cell proposed hybrid precoders/combiners with $K = 6$ compared to the sparse hybrid precoders/combiners [8], and [47] [48] in mm wave systems for $N_{BS} = 256$ and $N_{MS} = 16$ with 3 and 3 RF chains respectively, and $N_S = 3$.

Fig. 4.2 shows the performance with the same system parameters used in Fig. 4.1, but with QPSK modulation and ML detection instead of sphere decoding. Similarly to Fig. 4.1, the proposed hybrid precoding/combining design with $K = 6$ significantly improves the BER performance compared to the sparse hybrid precoding/combining design [8], and [47] [48]. It can be seen from Fig. 4.2 that by using the proposed hybrid precoding/combining design with $K = 6$ the ZF and MMSE detectors can achieve almost the same performance as the ML detector for low SNRs, with a small degradation for high SNRs. In contrast, the performance gap between the ML detector and the ZF and MMSE detectors with the sparse hybrid precoding/combining design is significant and increases with SNR. Hence, the proposed hybrid precoding/combining design with $K = 6$ can reduce considerably the performance gap between the ML detector and the ZF and MMSE detectors compared to the sparse hybrid precoding/combining design. Furthermore, there is a small difference between the ZF and MMSE detectors with the sparse hybrid precoding/combining designs, whereas their performance is identical with the proposed hybrid precoding/combining designs. Notice that the complexity of sphere decoding increases with the number of data streams and modulation order. Although the speed of sphere decoding (SD) increases in the high SNR region, it still requires a considerably longer time compared to the low complexity ZF/MMSE detectors for any *SNR* [47] [48].

In Figs. 4.3 and 4.4, the channel model has $N_{cl} = 8$ clusters, and the number of rays $N_{ray} = 10$ per cluster with an angular spread of 7.5° which is the same at the transmitter and receiver. Also, the transmitter's sector angle is 60° wide in the azimuth domain and 20° wide in elevation, but the receivers have relatively smaller antenna arrays of omni-directional elements. In Fig. 4.3, we evaluate the BER performance of the ZF detector using the proposed hybrid precoders/combiners with different numbers of iterations K, the sparse hybrid precoders/combiners [8], the unconstrained digital precoders/combiners, and the greedy hybrid precoders/combiners [26] for a 16 QAM 64×16 UPAs mm wave systems with $N_{RF}^{BS} = N_{RF}^{MS} = 4$ RF chains and $N_S = 3$ data streams. Fig. 4.3 shows that the ZF detector with the proposed hybrid precoders/combiners achieves a BER, which is very close to that of the unconstrained digital precoders/combiners and performs better than the ZF detector with sparse hybrid precoders/combiners over the whole range of SNR. The ZF detector with the proposed hybrid precoders/combiners performs similarly to the ZF detector with the greedy hybrid precoders/combiners with the smallest number of iteration $K = N_{RF}^{BS}$ - $N_S = 1$, but outperforms the greedy hybrid precoders/combiners when K is increased. Moreover, as we can see from Fig. 4.3, a number of iterations $K = 6$ or 10 is sufficient to outperform the other hybrid designs and to achieve a performance very close to that of the unconstrained digital precoders/combiners. Furthermore, the performance improvement of the proposed hybrid precoders/combiners is noticeably fast by increasing K from 1 to 6, but it becomes slow after $K = 6$. Notice that the HD-AM [28] cannot be applied when the number of RF chains is greater than the number of data streams

Fig. 4.4 shows the BER performance of the ZF detector with the proposed hybrid precoders/combiners with different numbers of iterations K, ZF detector with the sparse hybrid precoders/combiners, ZF detector with the unconstrained digital precoders/combiners, ZF detector with the greedy hybrid precoders/combiners, and ZF detector with the HD-AM [28] with different numbers of iterations M for a 16 QAM 64 x 16 UPAs mm wave system with $N_{RF}^{BS} = N_{RF}^{MS} = 3$ RF chains and $N_S = 3$ data streams. For the sake of fairness, we use the same number of iterations for the proposed hybrid precoders/combiners and the HD-AM design, i.e., $K = M$. As we can see from Fig. 4.4, the ZF detector with the proposed hybrid design and the ZF detector with HD-AM are overlapped and outperform the ZF detector with sparse hybrid design and the ZF detector with greedy hybrid design by increasing the number of iterations K and M. The improvement over the sparse hybrid design is significant and exceeds 6 dB even with $K = M = 1$. In addition, the number of iterations K or M should be equal to 6 since the performance is improved compared to $K = M = 1$, but after $K = M = 6$ the performance of proposed hybrid precoders/combiners and HD-AM improves slowly.

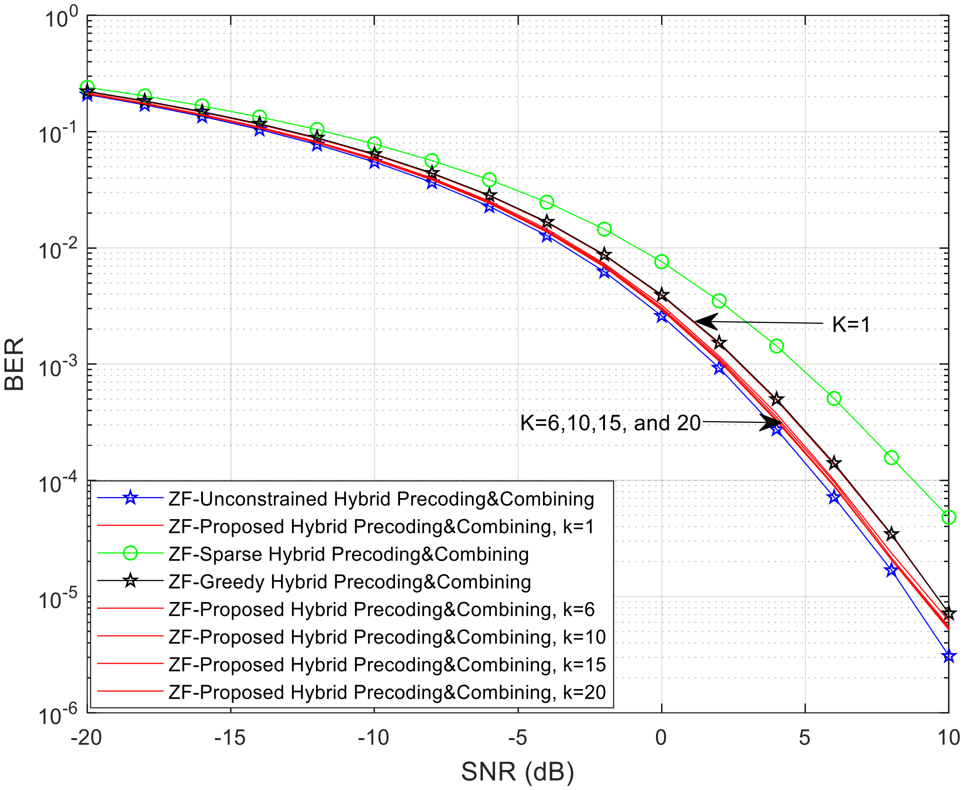

Figure 4. 3 BER performance achieved by the proposed design with different K compared to the sparse hybrid precoders/combiners [8], the optimal unconstrained digital precoders/combiners, and the greedy hybrid precoders/combiners [26] for ZF detector in uncoded 16 QAM single-cell in UPAs mm wave systems for $N_{BS} = 64$ and $N_{MS} = 16$ with 4 and 4 RF chains respectively, and $N_S = 3$.

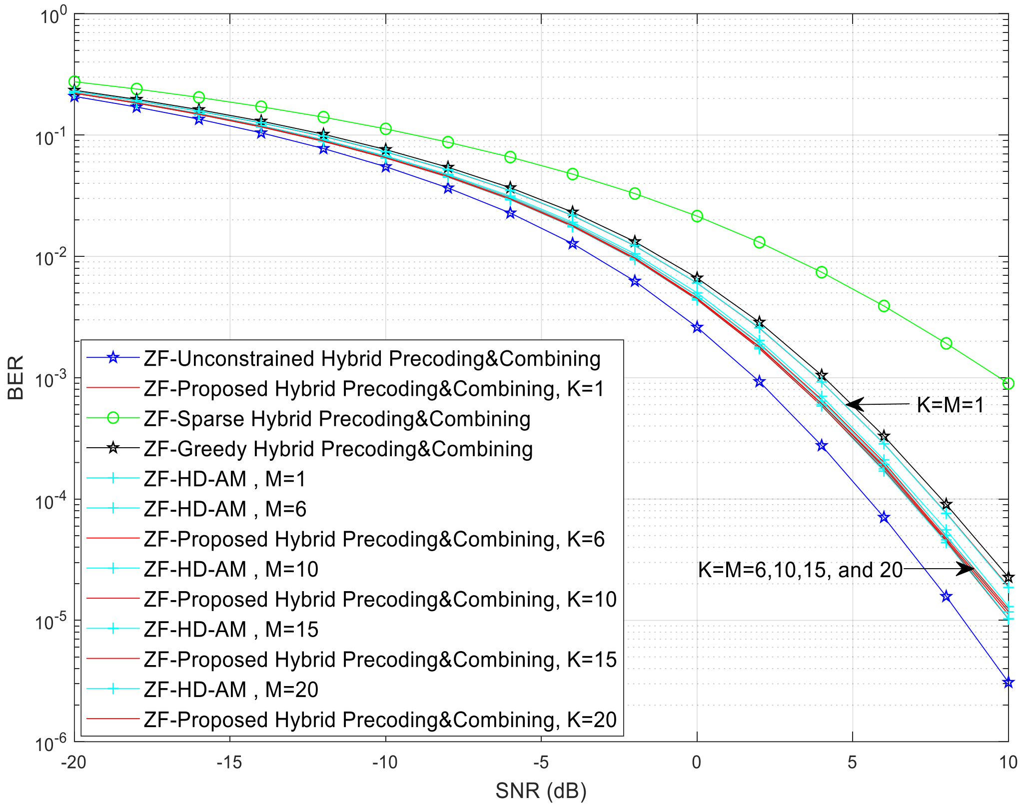

Figure 4. 4 BER performance achieved by the proposed design with different K compared to the sparse hybrid precoders/combiners [8], the optimal unconstrained digital precoders/combiners, the greedy hybrid precoders/combiners [26], and the HD-AM [28] with different M for for ZF detector in uncoded 16 QAM single-cell in UPAs mm wave systems for $N_{BS} = 64$ and $N_{MS} = 16$ with 3 and 3 RF chains respectively, and $N_S = 3$.

Figs. 4.5, 4.6, and 4.7 show the simulated sum rate of the proposed hybrid precoders/combiners with different number of iterations, sparse hybrid precoders /combiners, optimal unconstrained digital precoders/combiners, greedy hybrid design, and HD-AM with different number of iterations M. The channel model has $N_{cl} = 8$ clusters and the number of rays $N_{ray} = 10$ per cluster with an angular spread of 7.5° which is the same at the transmitter and receiver. Also, the transmitter's sector angle is 60° wide in the azimuth domain and 20° wide in elevation, but the receivers have relatively smaller antenna arrays of omni-directional elements.

Fig. 4.5 shows the spectral efficiency achieved by the proposed hybrid precoders/combiners, the sparse hybrid precoders /combiners, the optimal unconstrained digital precoders/combiners, greedy hybrid design in a 64 x 16 UPAs mm wave system for different SNR values with $N_S \in \{1,2\}$, and $N_{RF}^{BS} = N_{RF}^{MS} = 4$. The maximum number of iterations K for the proposed hybrid design is equal to N_{RF}^{BS} - N_S, which is 3 and 2 for $N_S = 1$ and 2 respectively. The proposed hybrid precoders/combiners and the greedy hybrid design outperform the sparse hybrid precoders /combiners for $N_S = 2$ and are almost similar for $N_S = 1$. The proposed hybrid design overlaps the greedy hybrid design for any number of data streams with the smallest number of iterations K and both achieve the optimal performance of the unconstrained digital precoder/combiner.

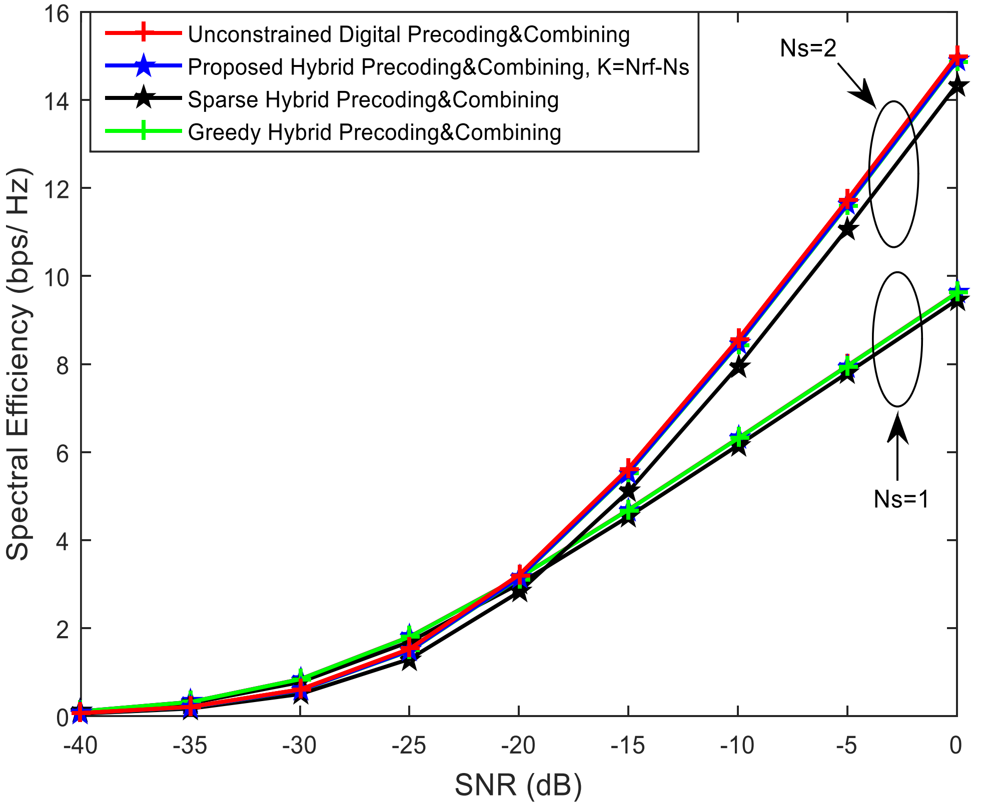

Figure 4. 5 Average spectral efficiency achieved by the proposed design with $K = N_{RF}^{BS}$ - N_S compared to the sparse hybrid precoders/combiners [8], the optimal unconstrained digital precoders/combiners, and the greedy hybrid precoders/combiners [26] for a 64 x 16 UPAs mm wave systems for different SNR values with $N_S \in \{1,2\}$, and $N_{RF}^{BS} = N_{RF}^{MS} = 4$.

When the number of RF chains equals the number of data streams, Fig. 4.6 shows the spectral efficiency achieved by the proposed hybrid precoders/combiners with different numbers of iterations K, the sparse hybrid precoders /combiners, the optimal unconstrained digital precoders/combiners, greedy hybrid design, and the HD-AM with different numbers of iterations M for different numbers of RF chains and data streams varying from 1 to 4 in a 64 x 16 UPAs mm wave system where $N_s = N_{RF}^{BS} = N_{RF}^{MS}$. The SNR is fixed to 0 dB for any number of RF chains. To make a fair comparison between the proposed hybrid design and the HD-AM, the number of iterations for both designs is the same, i.e., $K = M$. We can see that the proposed hybrid design and the HD-AM are overlapped and yield an improvement over the sparse hybrid design and the greedy hybrid design. Moreover, by increasing the number of iterations K and M, the overall performance of the proposed hybrid precoders/combiners and of the HD-AM is improved; the maximum number of iterations K and M for both designs should be between 1 and 6 because the performance improves slowly after $K = M = 6$.

Notice that the HD-AM can only be applied when $N_S = N_{RF}^{BS} = N_{RF}^{MS}$, but the proposed design, and the greedy hybrid design can be applied in the general case (the number of RF chains is greater than or equal to the number of data streams).

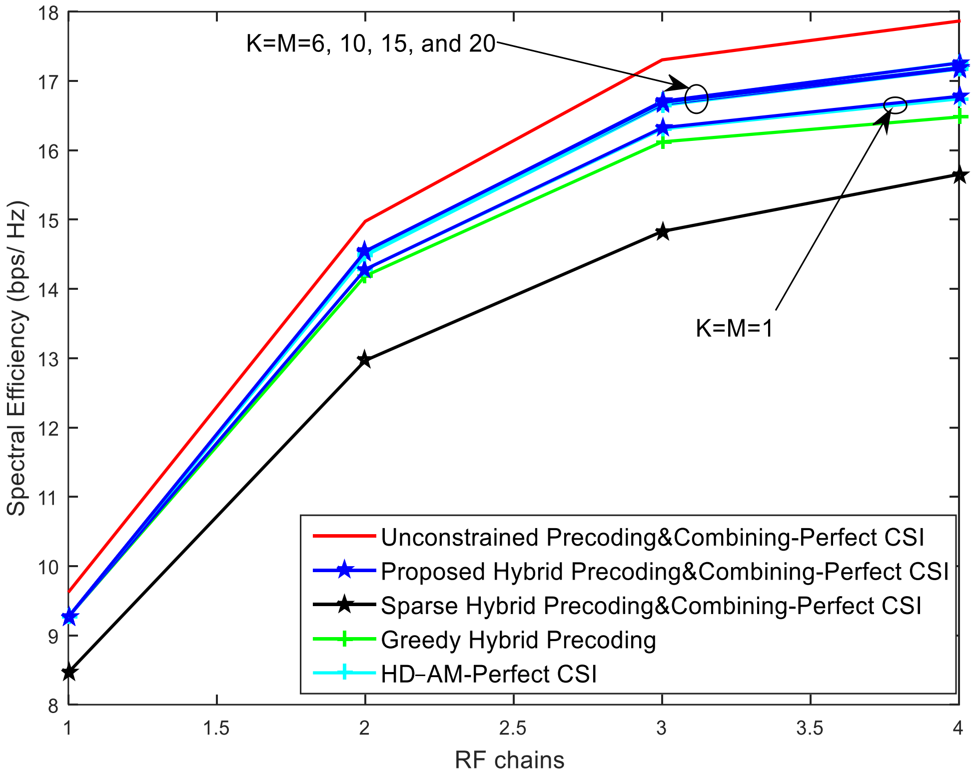

Figure 4. 6 Average spectral efficiency achieved by the proposed design with different K compared to the sparse hybrid precoders/combiners [8], the optimal unconstrained digital precoders/combiners, greedy hybrid precoders/combiners [26], and the HD-AM [28] with different M in 64 x 16 UPAs mm wave systems for $SNR = 0$ dB with $N_S = N_{RF}^{BS} = N_{RF}^{MS}$.

Fig. 4.7 evaluates the performance when the number of RF chains is greater than the number of data streams, where $N_S \in \{1,2,4\}$ and the SNR is fixed to 0 dB for any number of RF chains. We note again that the HD-AM cannot be applied when the number of RF chains is greater than the number of data streams. The other parameters are the same. The proposed hybrid design and the greedy hybrid design perform better than the sparse hybrid method in all cases. The proposed hybrid design with $K = 6$ can accurately approximate the optimal unconstrained one when the number of RF chains slightly exceeds the number of data streams. Moreover, it only needs a small number of RF chains (less than twice the number of streams) to achieve the optimal performance compared to the sparse hybrid precoders / combiners, and the greedy hybrid design. The gain of the proposed hybrid solution over the greedy hybrid design is noticeable for $N_S \in \{2,4\}$. In practice, the number of RF chains will be limited because of the high power consumption and cost per RF chain [6] [8] [9] [11] [66].

Notice that the number of iterations $K = 6$ of the proposed hybrid design is sufficient to outperform both the greedy hybrid design and the sparse hybrid design. Moreover, the total performance of the proposed hybrid design improves slowly when the number of iterations K increases beyond 6.

Therefore, the performance of the proposed method is the same as that of the HD-AM when $N_S = N_{RF}^{BS} = N_{RF}^{MS}$ and better than that of the greedy or sparse hybrid design when the number of RF chains is greater than or equal to the number of data streams with a reasonable number of iterations K.

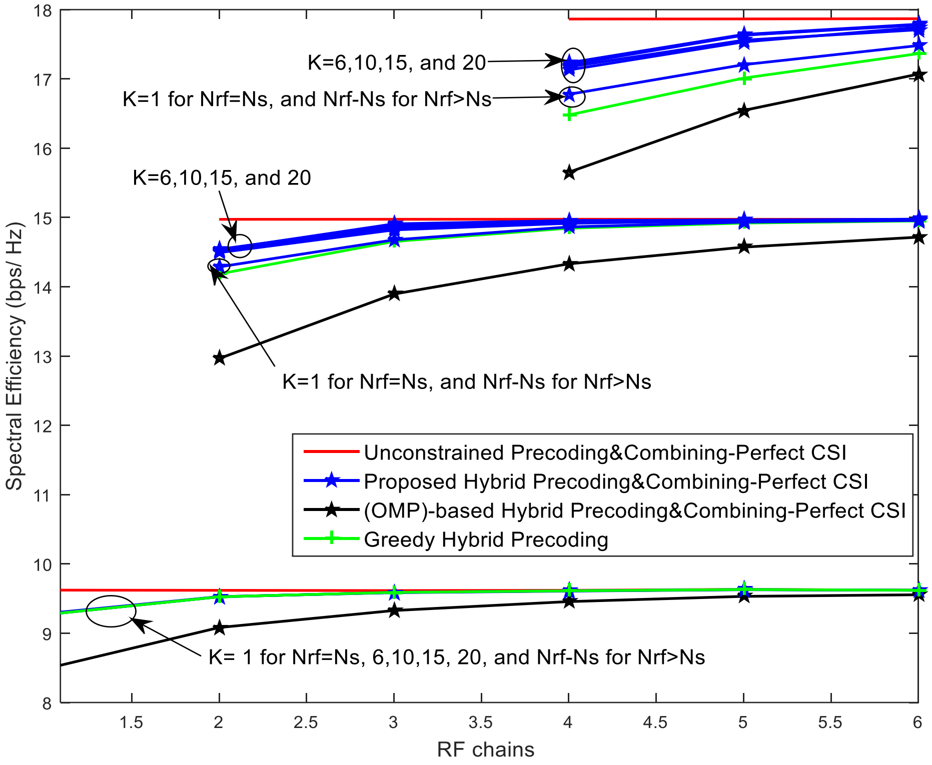

Figure 4. 7 Average spectral efficiency achieved by the proposed design with different K compared to the sparse hybrid precoders/combiners [8], the optimal unconstrained digital precoders/combiners, and the greedy hybrid precoders/combiners [26] in 64 x 16 UPAs mm wave systems for SNR = 0 dB with $N_S \in \{1,2,4\}$ and different RF chains.

Figs. 4.8 and 4.9 show the average simulation running time of the proposed hybrid design with different numbers of iterations K compared to the other methods vs. the number of BS antennas. All the results are obtained using the same computer with 10^6 iterations. The computer has i7 processor and a memory size of 8 gigabytes. In Fig. 4.8 and Fig. 4.9, we consider UPAs mm wave systems with $N_S = N_{RF}^{BS} = N_{RF}^{MS} = 3$ and $N_S = 3, N_{RF}^{BS} = N_{RF}^{MS} = 4$ respectively. As we can see from both figures, the complexity of the sparse hybrid method with an angular resolution $L = N_{BS}$ increases with the number of BS antennas. In addition, the proposed hybrid with any number of iterations K, HD-AM with any number of iterations M, and greedy hybrid have very low complexity compared to the sparse hybrid method especially when $N_S \ll N_{BS}$. In Fig. 4.8, the average simulation running time of the proposed hybrid design and HD-AM is the same for any number of iteration, where $K = M$ for fair comparison. In addition, the proposed hybrid design, HD-AM, and the greedy hybrid design have almost the same simulation time for small numbers of iterations $K = M = 1$ and 6 but the greedy hybrid design becomes faster with an increase in the number of iterations. In Fig. 4.9, the average simulation running times of the proposed hybrid design with $K = 6$ or 10 and of the greedy hybrid design are almost the same, but the simulation time of the proposed hybrid design increases slightly with the increase of the number of iterations K.

To summarize the performance results, when $N_S > 1$, the appropriate number of iterations for the proposed hybrid design is N_{RF} - $N_S \leq K \leq 6$ when the number of RF chains is greater than or equal to the number of data streams. In practice, the number of RF chains and data streams will be limited and hence, the difference between them should be less than 6.

Moreover, the gain of the proposed hybrid design improves slowly by increasing the number of iterations above 6. In the case when $N_S = 1$, the appropriate number of iterations in the proposed hybrid design is K=1 when the number of RF chains equals the number of data streams, i.e., N_{RF} = N_S and $K = N_{RF} - N_S$ when the number of RF chains is greater than the number of data streams.

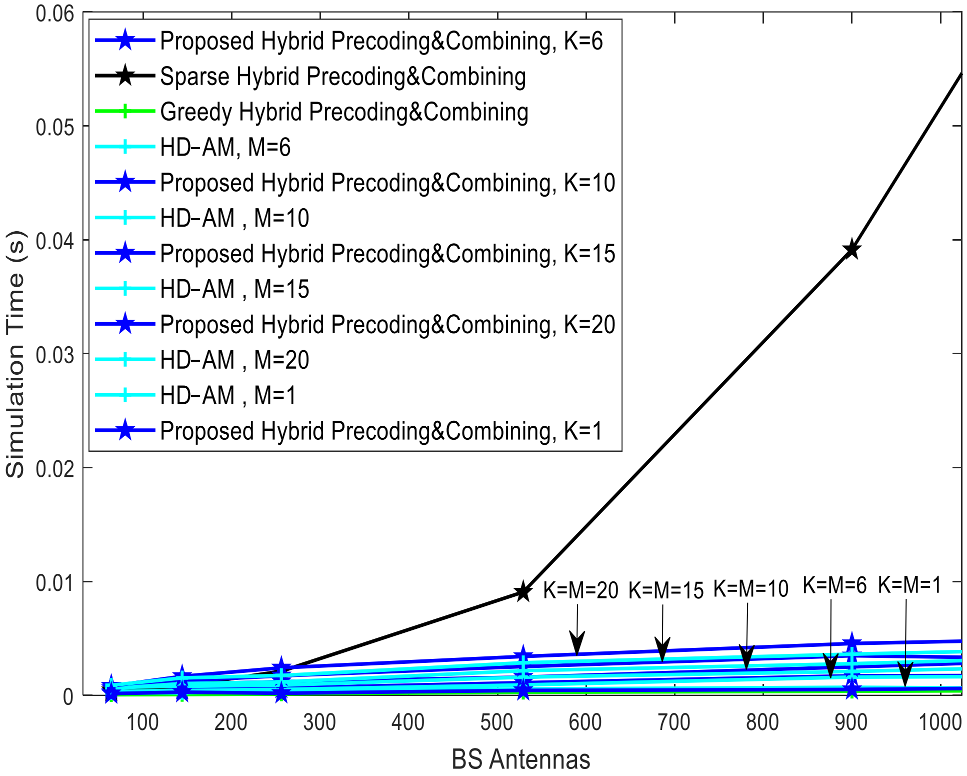

Figure 4. 8 Average running time of the proposed hybrid design with different K compared to the HD-AM with different M [28], greedy hybrid design [26], and sparse hybrid method [8] with different number of BS antennas for UPAs mm wave systems, and $N_{RF}^{BS} = N_{RF}^{MS} = N_S = 3$.

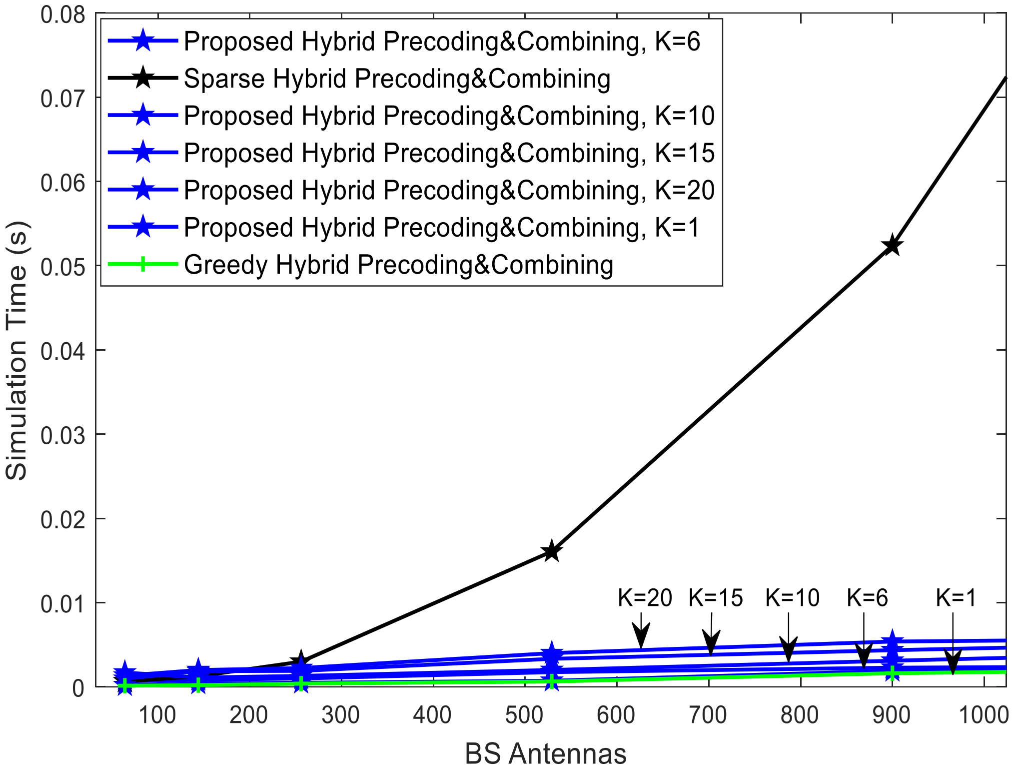

Figure 4. 9 Average running time of the proposed hybrid design with different K compared to the greedy hybrid design [26], and sparse hybrid method [8] with different number of BS antennas for UPAs mm wave systems and $N_{RF}^{BS} = N_{RF}^{MS}$=4, and $N_S = 3$.

4.3 Summary

In this chapter, we have proposed a low complexity hybrid precoder/combiner design for single user communication in mm wave systems. Assuming the channel state information is known, we consider an optimization problem that finds the hybrid precoder/combiner pair that best approximates the optimal unconstrained digital ones. In addition, there is no need to make any assumption on the antenna array geometry or for any other constraints such as the number of streams must be equal to the number of RF chains, and the unitary baseband precoder/combiner. The computational complexity of our proposed solution is comparable to that of the HD-AM technique and close to that of the greedy hybrid design when the number of iterations K is reasonable, and it is much lower than the complexity of the sparse hybrid design. The proposed solution can also be applied in all cases whereas the HD-AM technique can only be applied when the number of RF chains is equal to the number of data streams. Furthermore, based on our results, the proposed low complexity hybrid precoding/combining design improves the BER performance of simple ZF/MMSE detectors and considerably reduces the performance gap between these detectors and the high computational complexity ML detector or Sphere Decoding. Moreover, for a given detection scheme, the BER of the proposed hybrid beamformer is lower than that of the sparse hybrid and greedy beamformers, similar to the HD-AM and close to the unconstrained hybrid beamformer.

CHAPTER 5: LOW COMPLEXITY HYBRID PRECODING AND COMBINING WITH MOMENTUM GRADIENT DESCENT AND NEWTON'S METHOD FOR MILLIMETER WAVE SYSTEMS

5.1 Proposed Method

Our new work in this section combines the momentum method and Newton's Method with equation (4.7) to remove the zig-zag effect of the negative gradient before the convergence, and determine α automatically or avoid having to select a learning rate α respectively as described in Appendix A.2 and A.3 [74] [75]. In the momentum method, the first iterations will provide a crude moving average over the past gradients because we do not have enough values yet to average over; the solution is to use what's called bias-corrected version as described in Appendix A.3. In Newton's Method, the Hessian $\mathbf{F_{BB}}\mathbf{F_{BB}^H}$ of the objective function in (4.4) is N_{BS}^{RF} x N_{BS}^{RF} matrix. Because N_{BS}^{RF} is small, then the inversion of the Hessian $(\mathbf{F_{BB}}\mathbf{F_{BB}^H})^{-1}$ is easy to compute. However, $\mathbf{F_{BB}}\mathbf{F_{BB}^H}$ cannot be inverted when $N_S < N_{RF}^{BS}$; therefore, we use the preconditioning method (see Appendix A.2.2) to avoid inverting the Hessian in its entirety but only inverting the diagonal entries. From (4.7), we improve the performance of the proposed hybrid design by adding the momentum term $\mathbf{Z}_k$ and Newton's Method as follows

$$\mathbf{Z}_k = (\beta \nabla_f(\mathbf{F_{RF}^{\mathit{k}}}) + (1-\beta)\mathbf{Z}_{k-1})/(1-\beta^k) \qquad (5.1)$$

$$\mathbf{F_{RF}^{\mathit{k}+1}} = \mathbf{F_{RF}^{\mathit{k}}} + \alpha \mathbf{Z}_k (diag(\mathbf{F_{BB}}\mathbf{F_{BB}^H}))^{-1} \qquad (5.2)$$

where $\alpha > 0$ is the step length or learning rate, that controls the distance of the negative gradient direction from the RF precoder $\mathbf{F_{RF}^{\mathit{k}}}$, and β is the momentum decay term. Large β amounts to a long-range average, whereas small β amounts to only a slight correction relative to a gradient method. We use the learning rate α with Newton's Method because we do not use the full inversion of the Hessian and only invert the diagonal entries. Notice that with large values of k, β to the power of k will be indistinguishable from zero, thus not changing the values of $\mathbf{Z}_k$ at all. By using (5.1) and (5.2) in the proposed hybrid design, we can improve its performance with fewer number of iterations. From our preliminary results, we can confirm that the gradient descent with momentum and Newton's Method can improve the proposed hybrid design and reduce the objective function much more with only a small number of iterations K. This solution can also be applied when $N_S = N_{RF}^{BS}$. Note that when $N_S < N_{RF}^{BS}$, we need to complete the N_{BS} x N_{RF}^{BS} $\mathbf{F_{RF}}$ after the initialization. In each iteration, we add a column to $\mathbf{F_{RF}}$ which leads to the highest reduction of the residual. This column can be selected from the basis of the range of the residual, which is the element-wise normalization of the first singular vector of the residual.

The pseudo-code for the proposed hybrid precoder $\mathbf{F^P}$ solution with the gradient descent with momentum is given in Algorithm 5.1. Assume BS with N_{BS} antennas communicate with a single MS with N_{MS} antennas. The inputs of the algorithm are $\mathbf{F_{opt}} \in \mathbb{C}^{N_{BS} \text{x} N_S}$ and the maximum number of iterations K, where $K \geq N_{RF}^{BS}$ - N_S when $N_S < N_{RF}^{BS}$, in order to calculate the N_{BS} x N_{RF}^{BS} $\mathbf{F_{RF}}$ matrix, and $K \geq 1$ when $N_{RF}^{BS} = N_S$. In the general case of $N_S \geq 1$ where $N_S \leq N_{RF}^{BS}$, the algorithm starts by initializing $\mathbf{F_{RF}}$ with the element-wise normalization of the first N_{s} columns of $\mathbf{F_{opt}}$ i.e., $\mathbf{F_{RF}} = \mathbf{F_{opt}} \oslash \left(|\mathbf{F_{opt}}|\sqrt{N_{BS}}\right)$, and the momentum term $\mathbf{Z} \in C^{N_{RF} \text{x} N_S}$ with zero matrix. Then, $\mathbf{F_{BB}}$ is computed using least squares in step 2. After that, the algorithm proceeds to update the residual precoding matrix $\mathbf{F_{res}}$, the momentum term $\mathbf{Z}$, and the proposed RF precoder $\mathbf{F_{RF}}$ in steps 3, 4 and 5 respectively. Step 6 ensures that the proposed RF precoder $\mathbf{F_{RF}}$ is satisfied exactly with constant-magnitude entries which can be applied at RF using analog phase shifters.

In steps 8 and 9, when $N_S < N_{RF}^{BS}$, we need to complete the N_{BS} x N_{RF}^{BS} $\mathbf{F_{RF}}$, which can be done by adding the element-wise normalization of the first singular vector of the residual matrix $\mathbf{F_{res}}$ to $\mathbf{F_{RF}}$. After K iterations the process is completed and the algorithm will find the N_{BS} x N_{RF}^{BS} proposed RF precoding matrix $\mathbf{F_{RF}}$ and the optimal N_{RF}^{BS}x N_S baseband precoder $\mathbf{F_{BB}}$ such that $\left\|\mathbf{F_{opt}} - \mathbf{F_{RF}}\mathbf{F_{BB}}\right\|_F$ is minimized. In steps 13 and 14, we ensure that the transmit power constraint is satisfied and return the proposed hybrid precoder $\mathbf{F^P} = \mathbf{F_{RF}}\mathbf{F_{BB}}$. The proposed hybrid combiner $\mathbf{W_{RF}^P}$ can be calculated in the same way.

```
Algorithm 5.1: Proposed Hybrid Precoding with the gradient descent with momentum and Newton's Method.

Input: The optimum unconstrained solution $\mathbf{F_{opt}} \in C^{N_{BS} \times N_S}$ and the maximum number of iterations $K$.
Output: Analog $\mathbf{F_{RF}} \in C^{N_{BS} \times N_{RF}^{BS}}$ with the element-wise normalization and baseband $\mathbf{F_{BB}} \in C^{N_{\mathbf{RF}}^{\mathbf{BS}} \times N_S}$ such that $\left\|\mathbf{F_{opt}} - \mathbf{F^P}\right\|_F$ is reduced and $\left\|\mathbf{F^P}\right\|_F^2 = N_S$, where $\mathbf{F^P} = \mathbf{F_{RF}}\mathbf{F_{BB}}$.

Initialization: analog precoder $\mathbf{F_{RF}} = \mathbf{F_{opt}} \oslash \left(|\mathbf{F_{opt}}|\sqrt{N_{BS}}\right)$.
Initialization: the momentum term $\mathbf{Z} = \mathbf{F_{RF}}.\mathbf{0}$

1: for $i = 1{:}K$ do
2:    Update: $\mathbf{F_{BB}} = \left(\mathbf{F_{RF}^H}\mathbf{F_{RF}}\right)^{-1}\mathbf{F_{RF}^H}\mathbf{F_{opt}}$
3:    Update the residual: $\mathbf{F_{res}} = \mathbf{F_{opt}}$ - $\mathbf{F_{RF}}\mathbf{F_{BB}}$
4:    Update: $\mathbf{Z} = (\beta\mathbf{F_{res}}\mathbf{F_{BB}^H} + (1-\beta)\mathbf{Z})/((1-\beta^i))$
5:    Update: $\mathbf{F_{RF}} = \mathbf{F_{RF}} + \alpha\mathbf{Z}(\mathrm{diag}(\mathbf{F_{BB}}\mathbf{F_{BB}^H}))^{-1}$
6:    Element-Wise Normalization:
      $\mathbf{F_{RF}} = \mathbf{F_{RF}} \oslash \left(|\mathbf{F_{RF}}|\sqrt{N_{BS}}\right)$
7:    If $i \leq N_{RF}^{BS}$ - $N_S$
8:        $\mathbf{F_{res}} = \mathbf{U}\,\mathbf{\Sigma}\,\mathbf{V^H}$
9:        Append the element-wise normalization of the first vector of $\mathbf{U}$ as a new column to
          $\mathbf{F_{RF}}$: $\mathbf{F_{RF}} = [\ \mathbf{F_{RF}}\ \ (\mathbf{U})_1 \oslash \left(|(\mathbf{U})_1|\sqrt{N_{BS}}\right)\ ]$
10:   end if
11: end for
12: $\mathbf{F_{BB}} = \left(\mathbf{F_{RF}^H}\mathbf{F_{RF}}\right)^{-1}\mathbf{F_{RF}}\mathbf{F_{opt}}$
13: $\mathbf{F_{BB}} = \sqrt{N_S}\frac{\mathbf{F_{BB}}}{\left\|\mathbf{F_{RF}^P}\mathbf{F_{BB}}\right\|_F}$
14: return $\mathbf{F^P} = \mathbf{F_{RF}}\mathbf{F_{BB}}$
```

In Table I, we compare the proposed hybrid design with the previous method in chapter 4 and the other popular approaches in the literature. The hybrid design by alternating minimization (HD-AM) method [28], the sparse hybrid precoder [8], the greedy hybrid precoding [26], and the previous algorithm design are well described in chapter 4. The main difference between the new proposed algorithm and the previous design is the addition of the momentum term and the Newton's Method to the gradient descent in the design of analog precoder/combiner. The proposed solution can be applied in the general case (the number of RF chains can be greater than or equal to the number of data streams). The design of baseband precoder is not made exactly unitary unlike the HD-AM approach. Specifically, after the initialization of the analog precoder i.e., $\mathbf{F_{RF}} = \mathbf{F_{opt}} \oslash \left(\left|\mathbf{F_{opt}}\right|\sqrt{N_{BS}}\right)$, the baseband precoder of the proposed design is solved using the least squares solution, but it is approximately unitary or approximately semi-unitary [8][28]. After that, the analog precoder is designed by solving an optimization problem separately but adding the momentum term, which is given by $\mathbf{Z}_k = \frac{\beta \mathbf{F_{res}} \mathbf{F_{BB}^H} + (1-\beta)\mathbf{Z}_{\boldsymbol{k-1}}}{(\mathbf{1}-\beta^{\boldsymbol{k}})}$, and $\mathbf{F}_{\mathbf{RF}}^{k+1} = \mathbf{F}_{\mathbf{RF}}^{k} + \alpha \mathbf{Z}_k (\mathrm{diag}(\mathbf{F_{BB}} \mathbf{F_{BB}^H}))^{-1}$. Then, the analog precoder $\mathbf{F_{RF}}$ is normalized element-wise to satisfy the hardware constraint, i.e., $\mathbf{F}_{\mathbf{RF}}^{k+1} = \mathbf{F}_{\mathbf{RF}}^{k+1} \oslash \left(\left|\mathbf{F}_{\mathbf{RF}}^{k+1}\right| \sqrt{N_{BS}}\right)$ where each entry has constant magnitude, which can be implemented in the RF circuitry using analog phase shifters. Notice that the $\sqrt{N_{BS}}$ in the normalization step is a good way to make the diagonal of $\mathbf{F_{RF}}^{\mathbf{H}}\mathbf{F_{RF}}$ normalized to one, which is needed because $\mathbf{F_{opt}}^{\mathbf{H}}\mathbf{F_{opt}} = \mathbf{I}_{\mathbf{N_s}}$. Hence, its factors should also have a semi-unitary structure [28]. The analog precoder $\mathbf{F_{RF}}$ can be normalized again to the unit modulus between step 10 and 11 in Algorithm 5.1 and we have verified that the results have not been affected by that. This process is repeated up to K iterations. After the last iteration, $\mathbf{F_{BB}}$ is updated via the least squares. The same method can be applied for the hybrid combiners.

Table 5. 1 Comparison between the proposed method, previous method, and other approaches

Method	Sparse Hybrid Design [8]	Greedy Hybrid Design [26]	Hybrid Design by Alternating Minimization (HD-AM) [28]	Previous Hybrid Design (Chapter 4) [46]	Proposed Hybrid Design
Year	2014	2015	2016	2021	2022
Constraints	RF precoding /combining codebooks	None	1. $N_S = N_{RF}$ 2.Baseband precoders /combiners are exactly unitary	None	None
Initial analog precoder	None	$\mathbf{F_{RF}} = \mathbf{F_{opt}} \oslash \left(\lvert\mathbf{F_{opt}}\rvert\right)$	$\mathbf{F_{RF}} = \mathbf{F_{opt}} \oslash \left(\lvert\mathbf{F_{opt}}\rvert\right)$	$\mathbf{F_{RF}} = \mathbf{F_{opt}} \oslash \left(\lvert\mathbf{F_{opt}}\rvert\sqrt{N_{\mathrm{BS}}}\right)$	$\mathbf{F_{RF}} = \mathbf{F_{opt}} \oslash \left(\lvert\mathbf{F_{opt}}\rvert\sqrt{N_{\mathrm{BS}}}\right)$
Baseband precoder design	Least squares solution $\mathbf{F_{BB}} = \left(\mathbf{F_{RF}^H}\mathbf{F_{RF}}\right)^{-1}\mathbf{F_{RF}^H}$	Least squares solution $\mathbf{F_{BB}} = \left(\mathbf{F_{RF}^H}\mathbf{F_{RF}}\right)^{-1}\mathbf{F_{RF}^H}\mathbf{F_{opt}}$	$\mathbf{F_{opt}}^{\mathbf{H}}\mathbf{F_{RF}} = \mathbf{U\,\Sigma\,V^H}$ $\mathbf{F_{BB}} = \mathbf{V\,U^H}$	Least squares solution $\mathbf{F_{BB}} = \left(\mathbf{F_{RF}^H}\mathbf{F_{RF}}\right)^{-1}\mathbf{F_{RF}^H}\mathbf{F_{opt}}$	Least squares solution $\mathbf{F_{BB}} = \left(\mathbf{F_{RF}^H}\mathbf{F_{RF}}\right)^{-1}\mathbf{F_{RF}^H}\mathbf{F_{opt}}$
Analog precoder design	The vectors of $\mathrm{F_{RF}}$ are found from the RF precoding codebooks matrix $\mathrm{A_{BS}}$ along which the optimal precoder $\mathrm{F_{opt}}$ has the maximum projection	When $N_S < N_{RF}$, the columns of $\mathrm{F_{RF}}$ are selected from the element-wise normalization of the first singular vectors of the residual matrices $\mathrm{F_{res}}$	$\mathbf{F_{RF}} = \mathbf{F_{opt}}\mathbf{F_{BB}}^{\mathbf{H}} \oslash \left(\lvert\mathbf{F_{opt}}\mathbf{F_{BB}}^{\mathbf{H}}\rvert\right)$	$\mathbf{F_{RF}^{\mathit{k}+1}} = \mathbf{F_{RF}^{\mathit{k}}} + \boldsymbol{\alpha}\mathbf{F_{res}}\mathbf{F_{BB}^H}$ $\mathbf{F_{RF}^{\mathit{k}+1}} = \mathbf{F_{RF}^{\mathit{k}+1}} \oslash \left(\lvert\mathbf{F_{RF}^{\mathit{k}+1}}\rvert\sqrt{N_{BS}}\right)$ When $N_{\mathrm{S}} < N_{\mathrm{RF}}$, the columns of $\mathrm{F_{RF}}$ are selected from the element-wise normalization of the first singular vectors of the residual matrices $\mathrm{F_{res}}$	$\mathbf{Z}_k = \frac{\beta\mathbf{F_{res}}\mathbf{F_{BB}^H}+(1-\beta)\mathbf{Z}_{\boldsymbol{k-1}}}{(\mathbf{1}-\beta^{\boldsymbol{k}})}$ $\mathbf{F_{RF}^{\mathit{k}+1}} = \mathbf{F_{RF}^{\mathit{k}}} + \alpha\mathbf{Z}_k(\mathrm{diag}(\mathbf{F_{BB}}\mathbf{F_{BB}^H}))^{-1}$ $\mathbf{F_{RF}^{\mathit{k}+1}} = \mathbf{F_{RF}^{\mathit{k}+1}} \oslash \left(\lvert\mathbf{F_{RF}^{\mathit{k}+1}}\rvert\sqrt{N_{BS}}\right)$ When $N_{\mathrm{S}} < N_{\mathrm{RF}}$, the columns of $\mathrm{F_{RF}}$ are selected from the element-wise normalization of the first singular vectors of the residual matrices $\mathrm{F_{res}}$
Max # of iterations	N_{RF}	$N_{RF} - N_S$	M	K	K
Baseband/ Analog combiner design	Same as Baseband/Analog precoder design. Or minimize the mean square error between transmitted and received signals	Same as Baseband/Analog precoder design	Same as Baseband/Analog precoder design	Same as Baseband/Analog precoder design	Same as Baseband/Analog precoder design

5.2 Complexity Analysis of the Proposed Algorithm

In this section, we analyze the complexity in implementing the proposed hybrid precoding/combining design using Algorithm 5.1 as compared to previous methods from the literature. To simplify the complexity analysis, let us denote $N = L = \max\{N_{BS}, N_{MS}\}$, $N_{\mathrm{RF}} = \max\{N_{RF}^{BS}, N_{RF}^{MS}\}$, K is the maximum number of iterations of the proposed hybrid design, and M is the maximum number of iterations of the hybrid design by alternating minimization (HD-AM) [28]. In Table 5.2, we present the complexity analysis by evaluating the total number of floating-point operations (flops) for each hybrid precoding/combining approach.

Because of the angular resolution and the correlation function for sparse hybrid design, the previous design in chapter 4, the proposed design, greedy hybrid design [26], and the HD-AM [28] provide a great complexity reduction compared to the sparse hybrid design especially when $N_S \ll N$. Moreover, the computational complexity of the proposed hybrid design is twice that of the previous hybrid design, and the HD-AM when the maximum number of iterations is the same, i.e., $K = M$. However, the proposed hybrid design performs much better than the previous hybrid design, and the HD-AM with fewer iterations as we will see in the next section. Also, the drawback of the HD-AM is that it can only be used when the number of RF chains equals the number of data streams $N_S = N_{RF}$. The computational complexity of the proposed hybrid design is almost the same as that of the greedy hybrid design because our proposed hybrid design only needs a small number of iterations K to outperform the greedy hybrid design.

Therefore, the complexity of the proposed hybrid precoders/combiners is lower than that of the sparse hybrid precoders/combiners, twice the previous hybrid design, and the HD-AM with better performance when the maximum number of iterations is the same, i.e., $K = M$, and close to the greedy hybrid design with better performance.

Table 5. 2 Complexity of the proposed algorithm compared to previous methods from the literature

Method	Constraints	Complexity
Sparse Hybrid Design [18]	RF precoding/Combining codebooks	O($N^2 N_{RF} N_S$)
Hybrid Design by Alternating Minimization (HD-AM) [28]	$N_S = N_{RF}$	O($N N_S^2 M$)
Greedy Hybrid Design [26]	None	O($N N_{RF}^2 N_S$)
Previous Hybrid Design (Chapter 4) [46]	None	O($N N_{RF}^2 K$)
Proposed Hybrid Design	None	O($2 N N_{RF}^2 K$)

5.3 Simulation Results

This section presents the numerical results to show the performance advantages of the proposed hybrid precoders /combiners implemented as described in Algorithm 5.1. Specifically, we present the BER performance of the ZF, MMSE, ML, and sphere decoding. Moreover, we provide the sum rate for the proposed design compared to other popular methods from the literature. We show numerical simulations of the proposed methods' performance when maximizing the spectral efficiency as defined in (2.40). For all detection algorithms, the 16 QAM modulation schemes are used without error-control coding. In addition, for all cases, the mm wave channel remains constant during the transmission of one block of data.

In these simulations, we use the system architecture presented in Fig. 2.5. We consider the case where there is only one BS and one MS at a distance of 100 meters. The spacing between antenna elements is equal to $\lambda/2$. The system is assumed to operate at a 28 GHz carrier frequency in an outdoor scenario, and with a path loss exponent $n = 3.4$. The channel model is described in (2.34), with $\overline{\mathrm{P}_{\alpha,\iota}} = 1$ for all clusters. The azimuth and elevation angles AoAs/AoDs of the rays within a cluster are assumed to be randomly Laplacian distributed. The AoAs/AoDs azimuths and elevations of the cluster means are assumed to be uniformly distributed. We use the AoD/AoA beamforming codebooks (exact array response of mm wave channel) at the BSs and MSs respectively for the sparse hybrid design. The SNR in all the plots is defined as SNR $= P_r/\sigma^2$. We assume perfect CSI at the BS and MS. For fairness, the same total power constraint is enforced on all precoding/combining solutions.

In Figs. 5.1 and 5.2, the channel model has $N_{cl} = 8$ clusters, and the number of rays $N_{ray} = 10$ per cluster with an angular spread of 7.5° which is the same at the transmitter and receiver. Also, the transmitter's sector angle is 60° wide in the azimuth domain and 20° wide in elevation, but the receivers have relatively smaller antenna arrays of omni-directional elements. In Fig. 5.1, we evaluate the BER performance of the ZF detector using the proposed hybrid precoders/combiners with different numbers of iterations K, the sparse hybrid precoders/combiners [8], the unconstrained digital precoders/combiners, and the greedy hybrid precoders/combiners [26] for a 16 QAM 64 x 16 UPAs mmW systems with $N_{RF}^{BS} = N_{RF}^{MS} = 4$ RF chains and $N_S = 3$ data streams. Fig. 5.1 shows that the ZF detector with the proposed hybrid precoders/combiners achieves a BER, which is very close to that of the unconstrained digital precoders/combiners and performs better than the ZF detector with sparse hybrid precoders/combiners over the whole range of SNR. The ZF detector with the proposed hybrid precoders/combiners performs similarly to the ZF detector with the greedy hybrid precoders/combiners with the smallest number of iteration $K = N_{RF}^{BS} - N_S = 1$, but outperforms the greedy hybrid precoders/combiners when K is increased. Moreover, as we can see from Fig. 5.1, a number of iterations $K = 6$ or 10 is sufficient to outperform the other hybrid designs and to achieve a performance very close to that of the unconstrained digital precoders/combiners. Furthermore, the performance of the proposed hybrid precoders/combiners improves rapidly by increasing K from 1 to 6, but it improves slowly after $K = 6$. Notice that the the HD-AM [28] cannot be applied when the number of RF chains is greater than the number of data streams

Fig. 5.2 shows the BER performance of the ZF detector with the proposed hybrid precoders/combiners with different numbers of iterations K, ZF detector with the sparse hybrid precoders/combiners, ZF detector with the unconstrained digital precoders/combiners, ZF detector with the greedy hybrid precoders/combiners, and ZF detector with the HD-AM with different numbers of iterations M for a 16 QAM 64×16 UPAs mmW system with $N_{RF}^{BS} = N_{RF}^{MS} = 3$ RF chains and $N_S = 3$ data streams. For the sake of fairness, we use the same number of iterations for the proposed hybrid precoders/combiners and the HD-AM design, i.e., $K = M$. As we can see from Fig. 5.2, the ZF detector with the proposed hybrid design with K =1, the ZF detector with HD-AM with M =1, and the ZF detector with the greedy hybrid design are overlapped and outperform the ZF detector with sparse hybrid design. By increasing the number of iterations K and M, the ZF detector with the proposed hybrid design performs better than the ZF detector with HD-AM. In our previous design in chapter 4, the previous hybrid design overlaps with HD-AM design for all cases when $K = M$. However, in this chapter, our proposed hybrid design outperforms the HD-AM design when $K = M > 1$. The improvement over the sparse hybrid design is significant and exceeds 6 dB even with K=1 and more than that when $K > 1$.

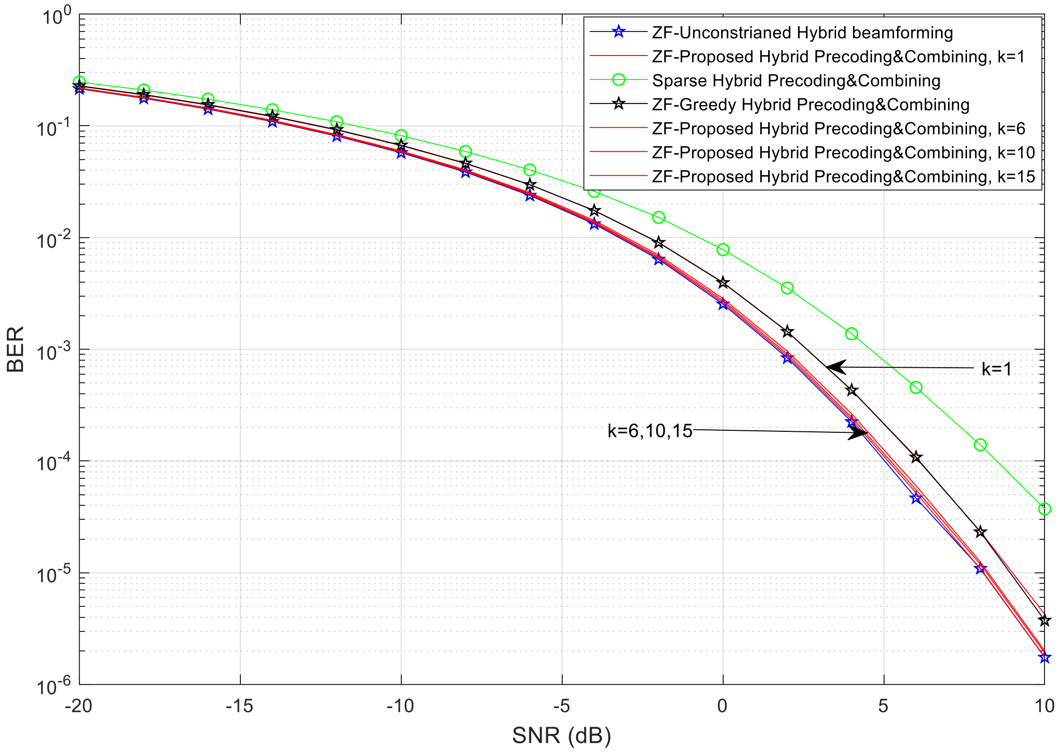

Figure 5. 1 BER performance achieved by the proposed design with different K compared to the sparse hybrid precoders/combiners [8], the optimal unconstrained digital precoders/combiners, and the greedy hybrid precoders/combiners [26] for ZF detector in uncoded 16 QAM single-cell in UPAs mm wave systems for $N_{BS} = 64$ and $N_{MS} = 16$ with 4 and 4 RF chains respectively, and $N_S = 3$.

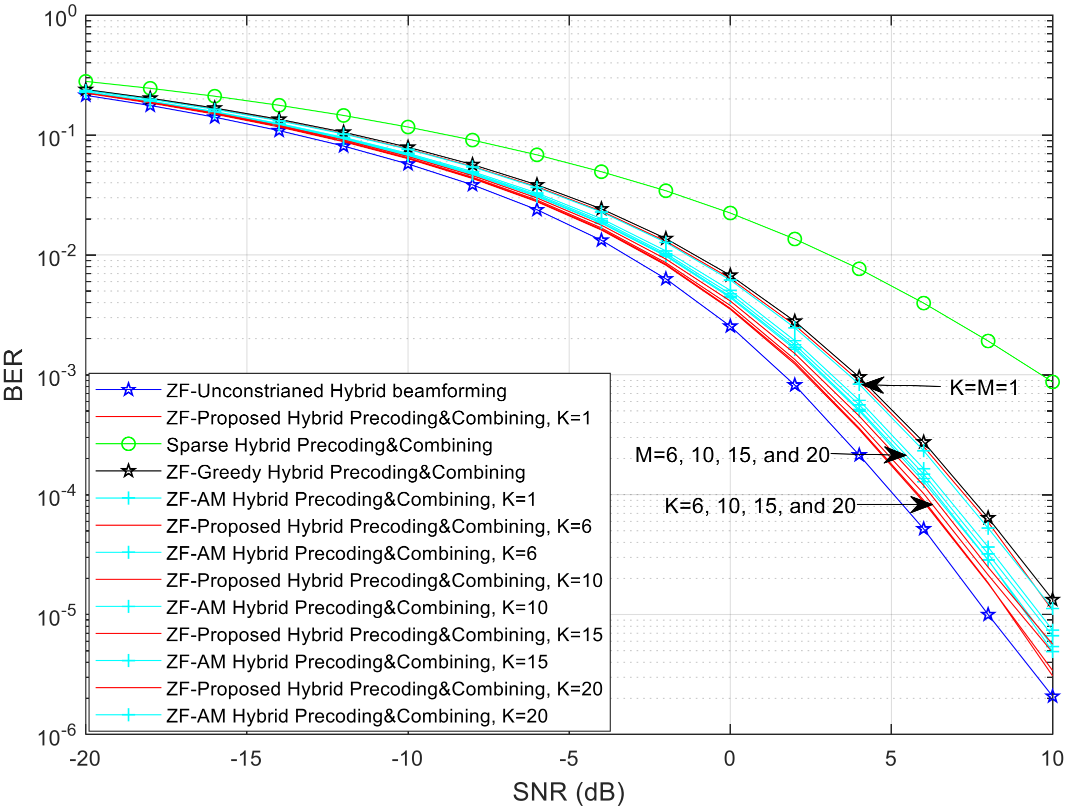

Figure 5. 2 BER performance achieved by the proposed design with different K compared to the sparse hybrid precoders/combiners [8], the optimal unconstrained digital precoders/combiners, the greedy hybrid precoders/combiners [26], and the HD-AM [28] with different M for for ZF detector in uncoded 16 QAM single-cell in UPAs mm wave systems for $N_{BS} = 64$ and $N_{MS} = 16$ with 3 and 3 RF chains respectively, and $N_S = 3$.

Fig. 5.3 shows the BER performance of the ZF detector with the proposed hybrid precoders/combiners with $K = 15$, ZF detector with the previous hybrid precoders/combiners (Chapter 4) [46] with different numbers of iterations K, and ZF detector with the unconstrained digital precoders/combiners for a 16 QAM 64 x 16 UPAs mmW system with $N_{RF}^{BS} = N_{RF}^{MS} = 4$ RF chains and $N_S = 4$ data streams. As we can see from Fig. 5.3, the ZF detector with the previous hybrid design needs a large number of iterations $K = 150$ in order to have the same performance as the proposed hybrid design with a very small number of iterations $K = 15$. Thus, the complexity of the previous design will increase ten times to have the same performance as the proposed hybrid design.

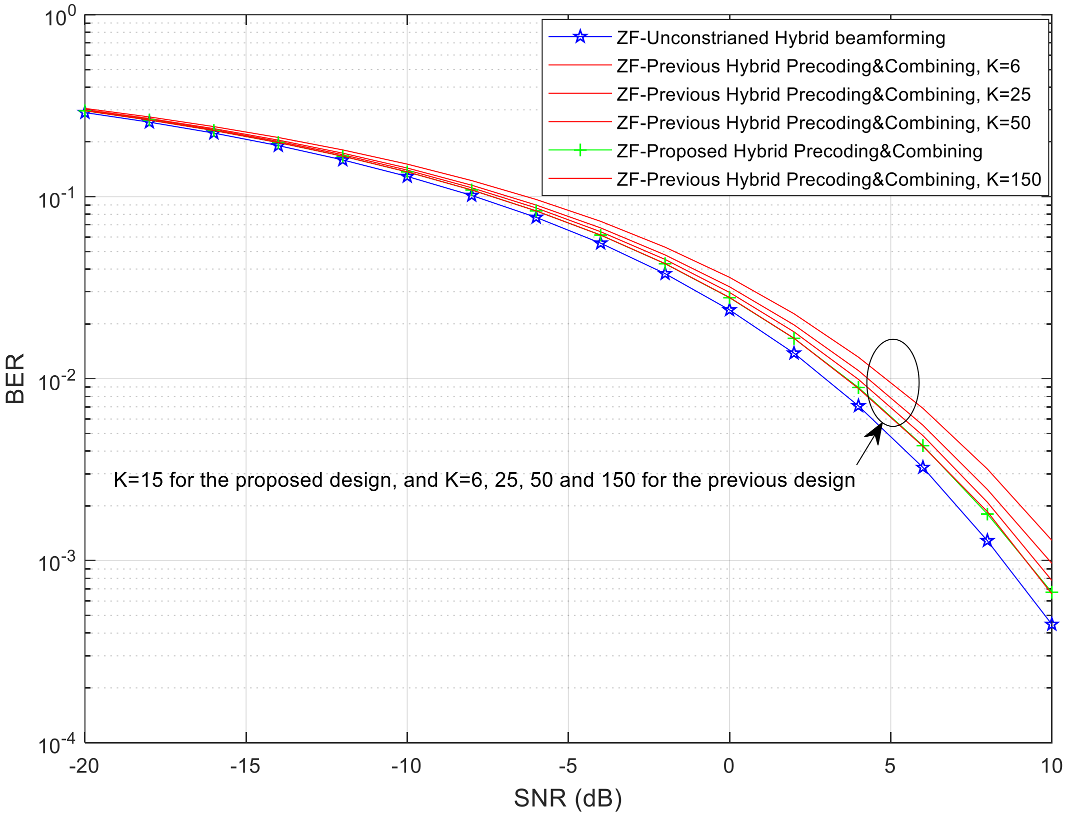

Figure 5. 3 BER performance achieved by the proposed design with $K = 15$ compared to the previous design [46] with different K, the optimal unconstrained digital precoders/combiners, for ZF detector in uncoded 16 QAM single-cell in UPAs mm wave systems for $N_{BS} = 64$ and $N_{MS} = 16$ with 4 and 4 RF chains respectively, and $N_S = 4$.

In Fig. 5.4, we evaluate the BER performance of the ZF detector using the proposed hybrid precoders/combiners with numbers of iterations $K = 15$, the previous hybrid precoders/combiners (Chapter 4) with different numbers of iterations K, and the unconstrained digital precoders/combiners for a 16 QAM 64 x 16 UPAs mmW systems with $N_{RF}^{BS} = N_{RF}^{MS} = 4$ RF chains and $N_S = 3$ data streams. Fig. 5.4 shows that the ZF detector with the proposed hybrid precoders/combiners with $K = 15$ achieves a BER, which is very close to that of the unconstrained digital precoders/combiners. The ZF detector with the previous hybrid precoders/combiners with a very large number of iteration $K = 150$ performs similarly to the ZF detector with the proposed hybrid precoders/combiners with $K = 15$. Therefore, the previous hybrid design needs high computational complexity to order to perform similarly to the proposed hybrid design.

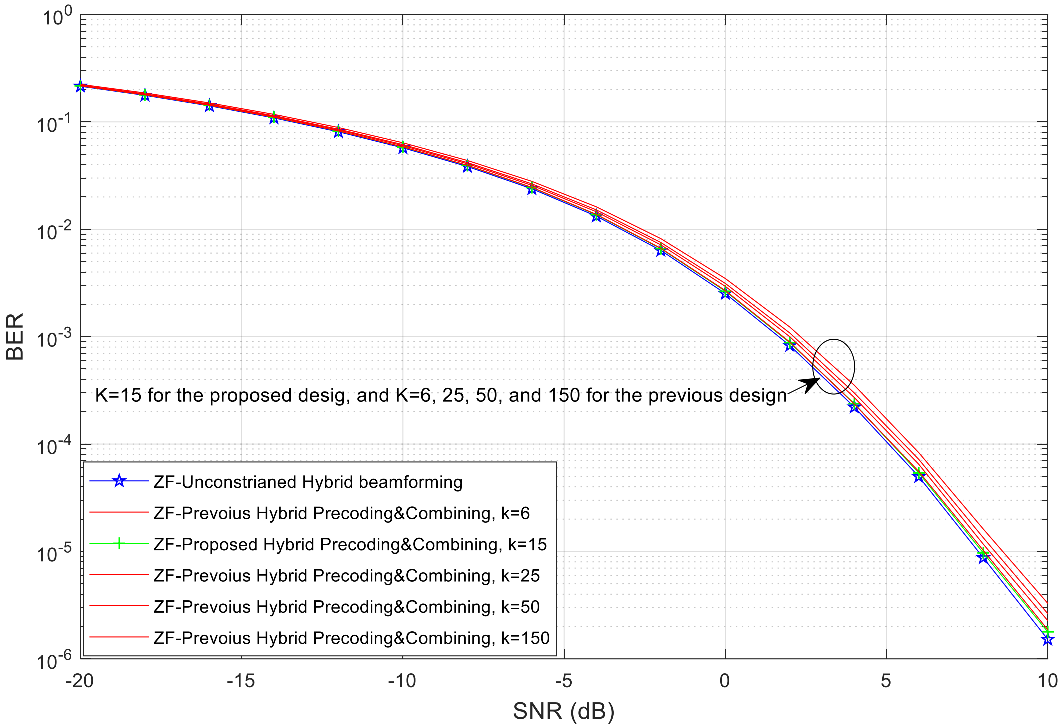

Figure 5. 4 BER performance achieved by the proposed design with $K = 15$ compared to the previous hybrid design [46] with different K, the optimal unconstrained digital precoders/combiners for ZF detector in uncoded 16 QAM single-cell in UPAs mm wave systems for $N_{BS} = 64$ and $N_{MS} = 16$ with 4 and 4 RF chains respectively, and $N_S = 3$.

Figs. 5.5 and 5.6 show the simulated sum rate of the proposed hybrid precoders/combiners with different number of iterations, sparse hybrid precoders /combiners, optimal unconstrained digital precoders/combiners, greedy hybrid design, and HD-AM with different numbers of iterations M. The channel model has $N_{cl} = 8$ clusters and the number of rays $N_{ray} = 10$ per cluster with an angular spread of 7.5^{o} which is the same at the transmitter and receiver. Also, the transmitter's sector angle is 60^{o} wide in the azimuth domain and 20^{o} wide in elevation, but the receivers have relatively smaller antenna arrays of omni-directional elements.

When the number of RF chains equals the number of data streams, Fig. 5.5 shows the spectral efficiency achieved by the proposed hybrid precoders/combiners with different numbers of iterations K, the sparse hybrid precoders /combiners, the optimal unconstrained digital precoders/combiners, greedy hybrid design, and the HD-AM with different numbers of iterations M for different numbers of RF chains and data streams varying from 1 to 4 in a 64 x 16 UPAs mm wave systems where $N_s = N_{RF}^{BS} = N_{RF}^{MS}$. The SNR is fixed to 0 dB for any number of RF chains. To make a fair comparison between the proposed hybrid design and the HD-AM, the number of iterations for both designs is the same, i.e., $K = M$. We can see that the proposed hybrid design outperforms the HD-AM for $= M > 1$, and the greedy hybrid design for $N_s = N_{RF}^{BS} = N_{RF}^{MS} = 2, 3,$ and 4 and yields an improvement over the sparse hybrid design for the whole number of RF chains which equals the number of data streams. Moreover, by increasing the number of iterations K and M, the overall performance of the proposed hybrid precoders/combiners is better than that of the HD-AM. Notice that the HD-AM can only be applied when $N_S = N_{RF}^{BS} = N_{RF}^{MS}$, but the proposed design, and the greedy hybrid design can be applied in the general case (the number of RF chains is greater than or equal to the number of data streams).

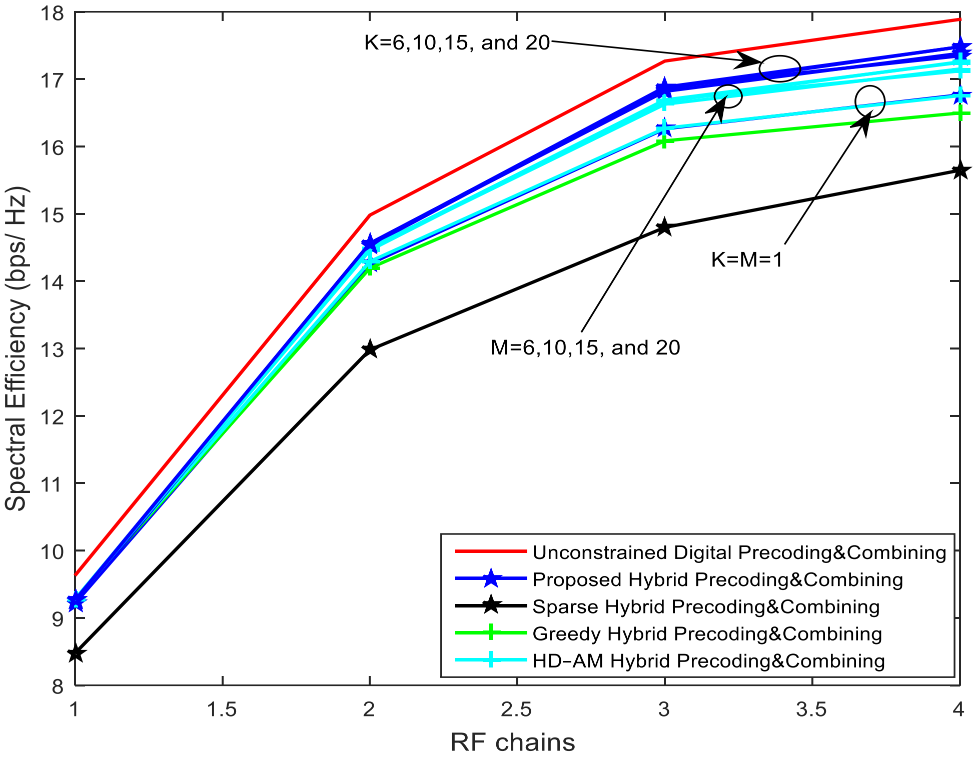

Figure 5. 5 Average spectral efficiency achieved by the proposed design with different K compared to the sparse hybrid precoders/combiners [8], the optimal unconstrained digital precoders/combiners, greedy hybrid precoders/combiners [26], and the HD-AM [28] with different M in 64 x 16 UPAs mm wave systems for $SNR = 0$ dB with $N_S = N_{RF}^{BS} = N_{RF}^{MS}$.

Fig. 5.6 evaluates the performance when the number of RF chains is greater than the number of data streams, where $N_S \in \{1,2,4\}$ and the SNR is fixed to 0 dB over the whole range of RF chains. We note again that the HD-AM can not be applied when the number of RF chains is greater than the number of data streams. The other parameters are the same. The proposed hybrid design and the greedy hybrid design perform better than the sparse hybrid method in all cases. The proposed hybrid design with $K = 6$ can accurately approximate the optimal unconstrained one when the number of RF chains slightly increases over the number of data streams. Moreover, it only needs a small number of RF chains (less than twice the number of streams) to achieve the optimal performance compared to the sparse hybrid precoders / combiners, and the greedy hybrid design.

The gain of the proposed hybrid solution over the greedy hybrid design is noticeable for $N_S \in \{2,4\}$. In practice, the number of RF chains will be limited because of the high power consumption and cost per RF chain [8]-[9]. Notice that the number of iterations $K = 6$ of the proposed hybrid design is sufficient to outperform both the greedy hybrid design and the sparse hybrid design. Moreover, the total performance of the proposed hybrid design improves slowly when the number of iterations K increases beyond 6.

Therefore, the performance of the proposed method is better than the HD-AM when $N_S = N_{RF}^{BS} = N_{RF}^{MS}$ for $K = M > 1$ and better than that of the greedy or sparse hybrid design when the number of RF chains is greater than or equal to the number of data streams with a reasonable number of iterations K.

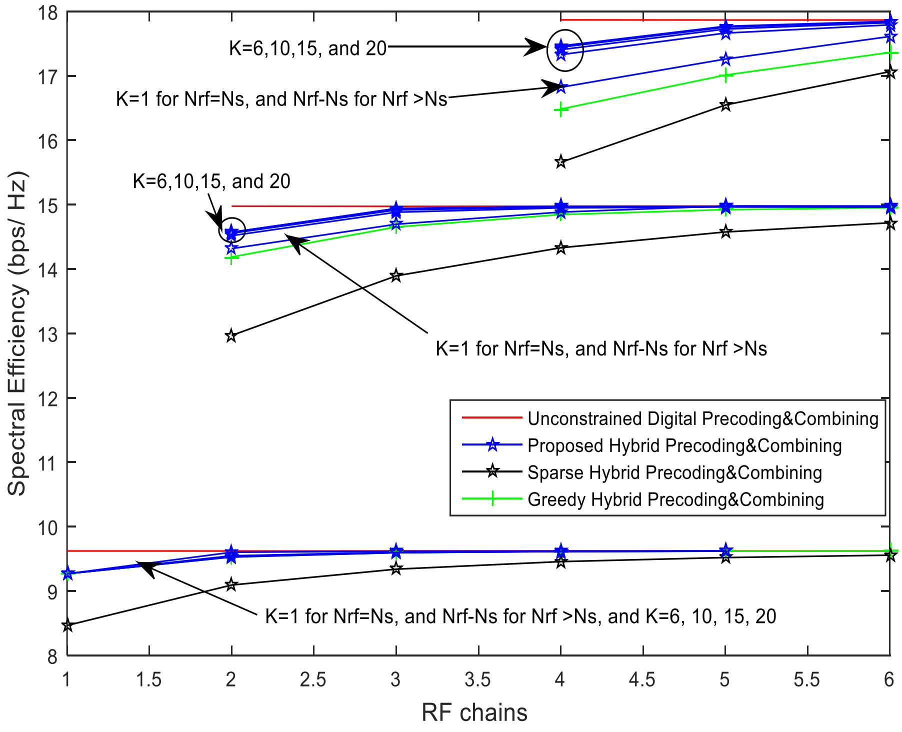

Figure 5. 6 Average spectral efficiency achieved by the proposed design with different K compared to the sparse hybrid precoders/combiners [18], the optimal unconstrained digital precoders/combiners, and the greedy hybrid precoders/combiners [28] in 64 x 16 UPAs mm wave systems for $SNR = 0$ dB with $N_S \in \{1,2,4\}$ and different RF chains.

In Figs. 5.7 and 5.8, we show the spectral efficiency achieved by the proposed hybrid precoders/combiners with number of iterations $K = 15$, the previous hybrid precoders/combiners (Chapter 4) with different numbers of iterations K, and the unconstrained digital precoders/combiners for a 16 QAM $64 \text{ x } 16$ UPAs mmW systems with $N_S > N_{RF}^{BS} = N_{RF}^{MS}$, and $N_S = N_{RF}^{BS} = N_{RF}^{MS}$ respectively. Fig. 5.7 and 5.8 show that the proposed hybrid precoders/combiners with $K = 15$ achieves a spectral efficiency very close to that of the unconstrained digital precoders/combiners. Moreover, the previous hybrid precoder/combiner needs a very large number of iterations $K = 150$ to perform similarly to the proposed hybrid precoders/combiners with $K = 15$ for $N_S \in \{2,4\}$ in Fig 5.7 and for the entire range of data streams in Fig 5.8. Therefore, the previous hybrid design needs a high computational complexity in order to perform similarly to the proposed hybrid design.

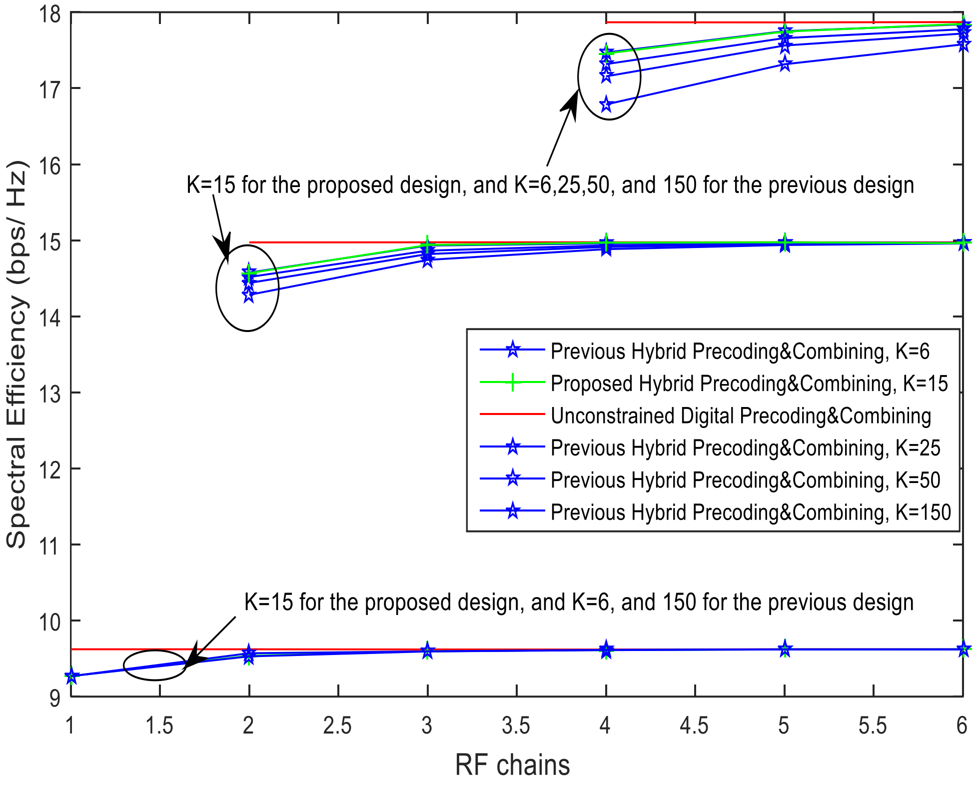

Figure 5. 7 Average spectral efficiency achieved by the proposed design with $K = 15$ compared to the previous hybrid precoders/combiners with different K [46], and the optimal unconstrained digital precoders/combiners in 64 x 16 UPAs mm wave systems for $SNR = 0$ dB with $N_S \in \{1,2,4\}$ and different RF chains.

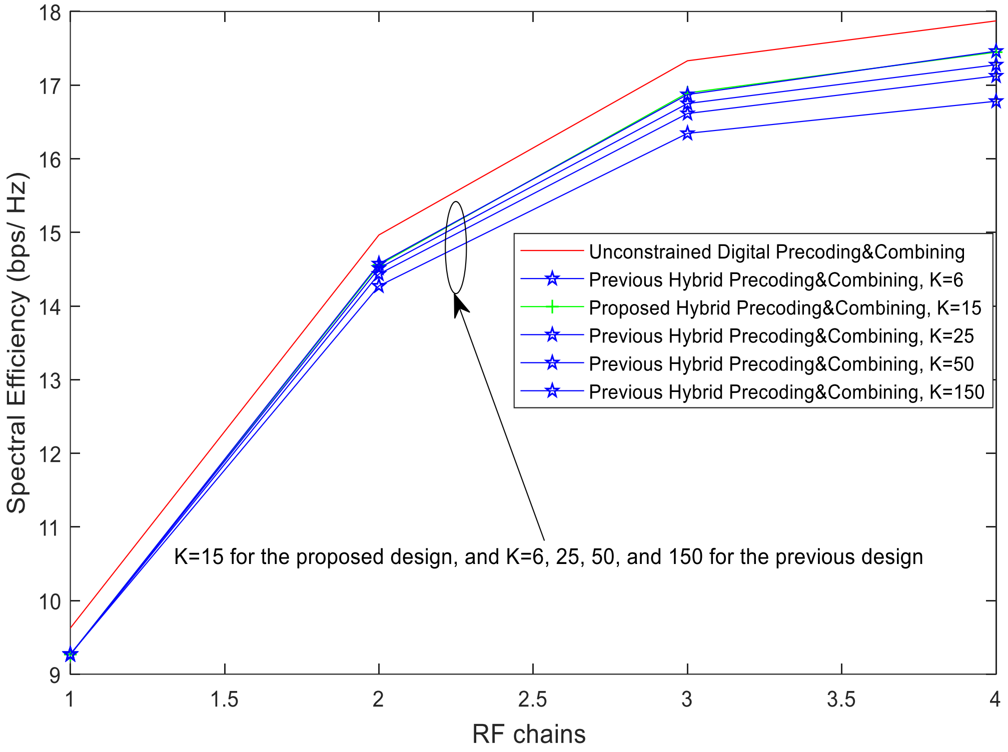

Figure 5. 8 Average spectral efficiency achieved by the proposed design with $K = 15$ compared to the previous hybrid precoders/combiners with different K [46], and the optimal unconstrained digital precoders/combiners in 64 x 16 UPAs mm wave systems for *SNR* = 0 dB with $N_S = N_{RF}^{BS} = N_{RF}^{MS}$.

Figs. 5.9 shows the average simulation running time of the proposed and previous hybrid design (Chapter 4) vs. the numbers of iterations K. All the results are obtained using the same computer with 10^6 iterations. The computer has i7 processor and a memory size of 8 gigabytes. In Fig. 5.9, we consider 64 x 16 UPAs mmW systems with $N_S = N_{RF}^{BS} = N_{RF}^{MS} = 3$. As we can see, the complexity of the proposed and previous hybrid design increases with the number of iterations K. In addition, the complexity of the proposed hybrid design is higher compared to the previous hybrid method. The average simulation running time of the proposed hybrid design is twice that of the previous hybrid design as we showed in the complexity analysis section. However, the performance of the proposed hybrid design is much better than the previous design with only a very small number of iterations K.

To summarize the performance results, when $N_S > 1$, the appropriate number of iterations for the proposed hybrid design should be much smaller than the previous hybrid design with higher performance when the number of RF chains is greater than or equal to the number of data streams. In the case when $N_S = 1$, the appropriate number of iterations in the proposed hybrid design is K=1 when the number of RF chains equals the number of data streams, i.e., $N_{RF} = N_S$ and $K = N_{RF} - N_S$ when the number of RF chains is greater than the number of data streams.

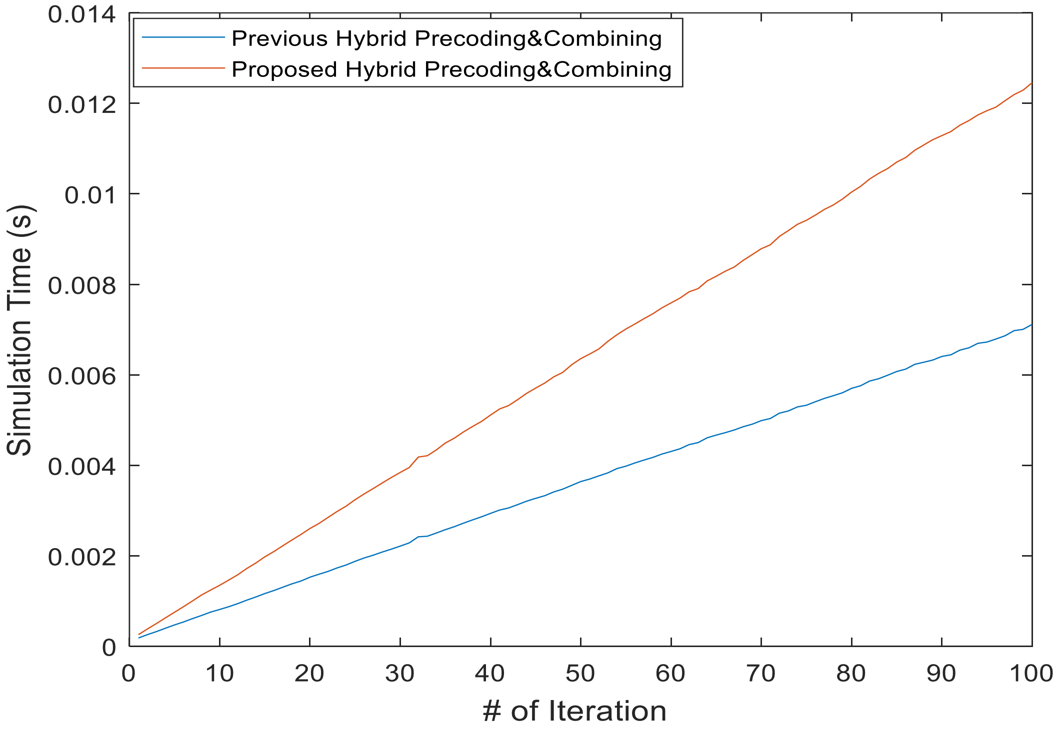

Figure 5. 9 Average running time of the proposed and previous hybrid design [46] with different K for 64 x 16 UPAs mm wave system.

Figs. 5.10 shows the average value of the objective function $\left\|\mathbf{F_{opt}} - \mathbf{F_{RF}F_{BB}}\right\|_F$ vs. the number of iterations K for one million simulation runs of the proposed hybrid beamformer and the previous design (Chapter 4). In Fig. 5.10, we use UPAs mm wave systems with $N_S = 3, N_{RF}^{BS} = N_{RF}^{MS} = 4$ and $N_S = N_{RF}^{BS} = N_{RF}^{MS} = 4$. As we can see from the figure, the objective function $\left\|\mathbf{F_{opt}} - \mathbf{F_{RF}}\mathbf{F_{BB}}\right\|_F^2$ of the proposed design has the smallest values compared to the other objective functions for the entire number of iterations. After the number iteration $K = 1000$, all the objective functions for all designs converge together to a lower bound. The objective function of the proposed design with only the momentum method (without using the Newton's Method) is in the middle between the previous design and the proposed design, which uses the momentum method and Newton's Method. The momentum method decreases the objective function compared to the previous design, but without using the Newton's Method, we need to select manually the learning rate α, which is not an easy task. Notice than the value of β increases to 0.4 instead of 0.3 when $N_{RF} > N_S$ and that is because the optimization problem is ill-conditioned which means that there are some directions where progress is much slower than in others. Thus, we use a larger value of β to obtain more stable directions of descent. When $N_{RF} > N_S$, the objective function is smaller compared to the case when $N_{RF} = N_S$ and that is because the proposed and previous hybrid design can more accurately approximate the optimal unconstrained beamformer.

The proposed design by using only the momentum method can improve the performance compared to the previous design, but it is better to use the momentum method and Newton's Method in our proposed design to improve performance much more with fewer number of iteration K. This plot is consistent with the convergence property in Remark 1 as described in Chapter 4.1.

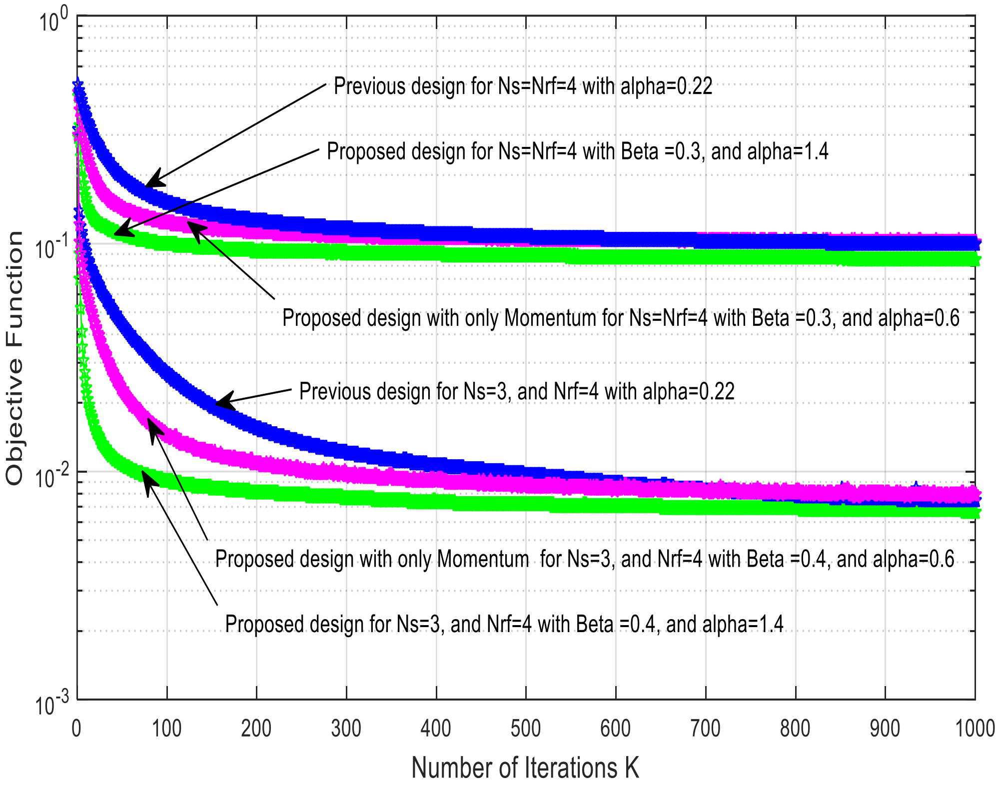

Figure 5. 10 Average value of the objective function $\left\|\mathbf{F_{opt}} - \mathbf{F_{RF}F_{BB}}\right\|_F^2$ obtained by simulating the proposed hybrid design with different numbers of iteration K compared to the previous design [46] for a 64 x 16 UPAs mm wave system with $N_{RF}^{BS} = N_{RF}^{MS} = N_S = 4$ and $N_{RF}^{BS} = N_{RF}^{MS} = 4$ and $N_S = 3$

Figs. 5.11 shows a closer look at the average value of the objective function $\left\|\mathbf{F_{opt}} - \mathbf{F_{RF}F_{BB}}\right\|_F$ vs. the number of iterations K which was simulated in Fig 5.10. As we can see from both figures Figs. 5.11 (a) and (b), the previous hybrid design needs very large number of iterations, around K=150, to performs similarly to the proposed hybrid design with $K = 15$. Therefore, the previous hybrid design needs a high computational complexity in order to perform similarly to the proposed hybrid design. This plot confirms the results that we showed in Fig 5.3, 5.4, 5.7, and 5.8.

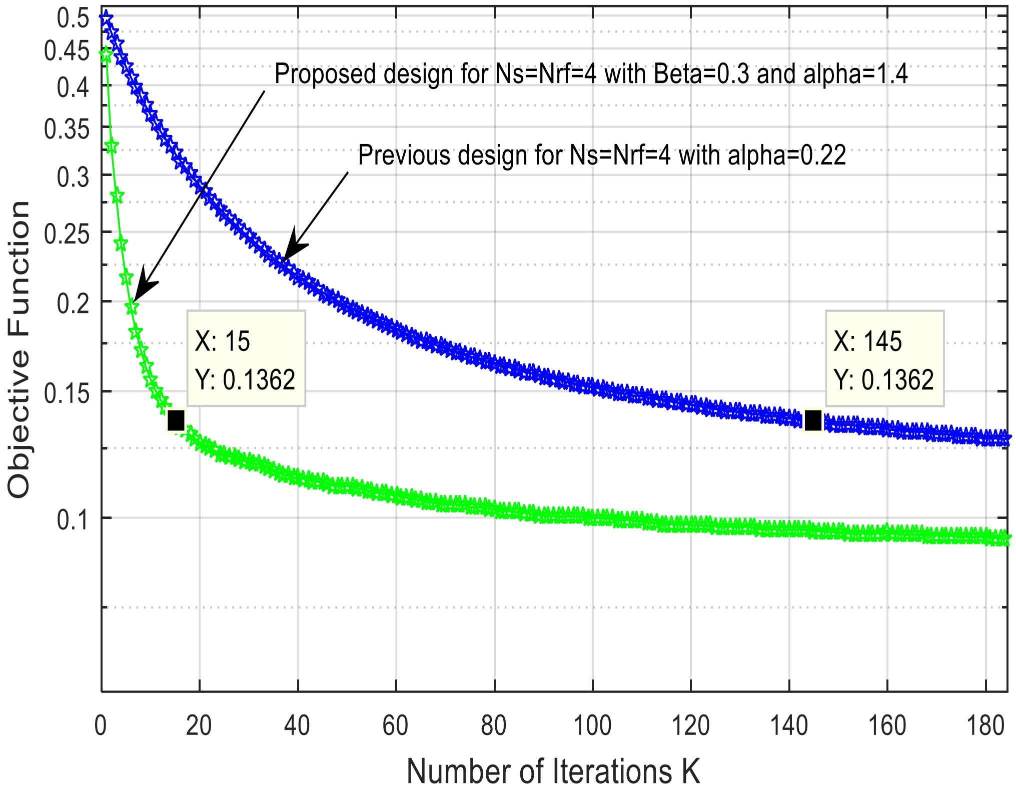

(a) $N_{RF}^{BS} = N_{RF}^{MS} = N_S = 4$

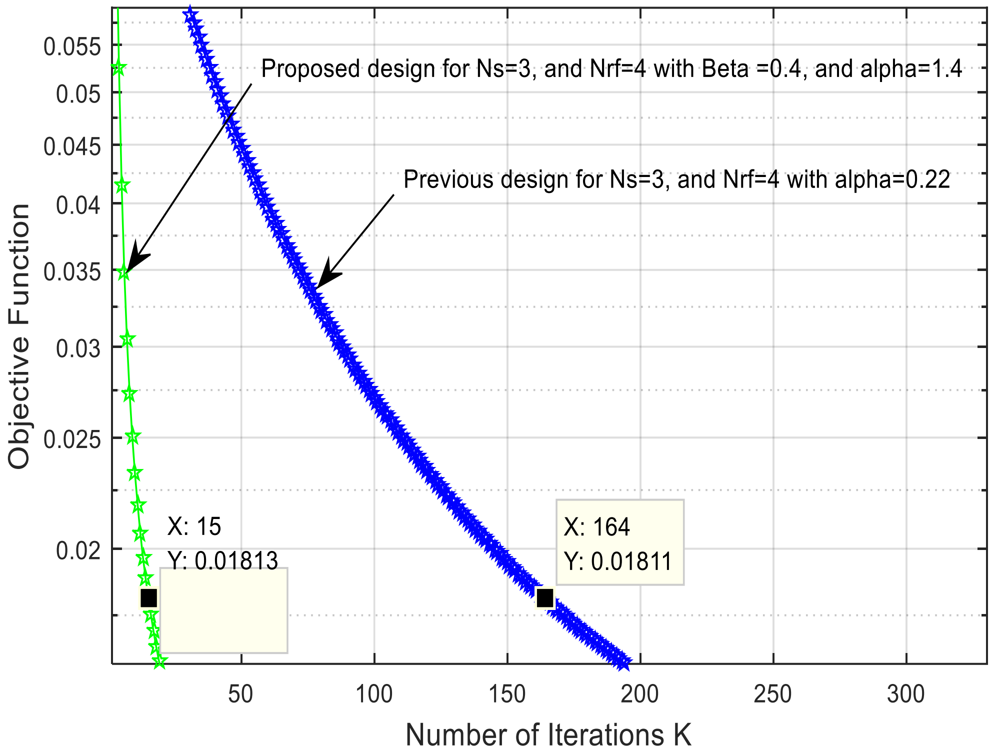

(b) $N_{RF}^{BS} = N_{RF}^{MS} = 4$ and $N_S = 3$

Figure 5. 11 Average value of the objective function $\left\|\mathbf{F_{opt}} - \mathbf{F_{RF}}\mathbf{F_{BB}}\right\|_F^2$ obtained by simulating the proposed hybrid design with different numbers of iteration K compared to the previous design [46] for a 64 x 16 UPAs mm wave system with $N_{RF}^{BS} = N_{RF}^{MS} = N_S = 4$ and $N_{RF}^{BS} = N_{RF}^{MS} = 4$ and $N_S = 3$

5.4 Summary

In this chapter, we have proposed a low complexity hybrid precoder/combiner design for single user communication in mm wave systems. Assuming the channel state information is known, we consider an optimization problem that finds the hybrid precoder/combiner pair that best approximates the optimal unconstrained digital one. We combine the momentum method and Newton's Method in the proposed hybrid design to remove the oscillating effect of the negative gradient and determine α automatically respectively. In addition, there is no need to make any assumption on the antenna array geometry or for any other constraints such as the number of streams must be equal to the number of RF chains, and the unitary baseband precoder/combiner.

The computational complexity of our proposed solution is much lower than the complexity of the sparse hybrid design, but twice that of the previous hybrid design (Chapter 4) with the same number of iterations and the HD-AM technique with the same number of iterations. However, the proposed design needs a very small number of iterations to outperform the previous hybrid design and the HD-AM technique. Moreover, the computational complexity of our proposed solution is close to that of the greedy hybrid design when the number of iterations K is reasonable while yielding a better performance.

Our proposed solution can also be applied in all cases whereas the HD-AM technique can only be applied when the number of RF chains is equal to the number of data streams. The simulation results show that our proposed low complexity solution with a reasonable number of iterations K outperforms the previous hybrid design, the HD-AM technique when $N_S = N_{RF}^{BS} = N_{RF}^{MS}$ and $K = M$, and the greedy or sparse hybrid design in all cases. Moreover, for a given detection scheme, the BER of the proposed hybrid beamformer is lower than that of the previous hybrid design, the sparse hybrid and greedy beamformers, the HD-AM and close to the unconstrained hybrid beamformer. Finally, because of the large available bandwidth in mm wave systems, it will be interesting to extend the proposed hybrid design to the multicarrier techniques such as orthogonal frequency division multiplexing (OFDM).

Chapter 6: Direct Conversion of Hybrid Precoding from Full Array Architecture to Subarray Architecture for mm wave MIMO Systems

Hybrid precoding is a key technology for massive multiple-input multiple-output (MIMO) systems for mm wave communications [5]. The hybrid precoding/combining architectures currently in use can be classified as full array (FA) or subarray (SA) [77]-[78]. Because each radio frequency (RF) chain is linked to each antenna by using phase shifters (PSs), the FA hybrid precoding/combining architecture can provide high spectral efficiency, but requires a large number of phase shifters, which results in high complexity and power consumption [79]-[80]. Because each RF chain in the SA architecture is only connected to a subset of antennas, it consumes significantly less energy than the FA architecture and its complexity is lower than that of the FA architecture [77]-[78]. As a result, the array gain realised in the SA architecture is of course lower than that in the FA architecture.

Recently, SA architecture has received a lot of attention because of its reduced complexity. SA architecture can be classified into fixed SA [78], [81] and dynamic SA [77], [82]-[83]. Although a dynamic SA architecture requires more power than a fixed SA architecture, and an increased amount of hardware and computational complexity, the dynamic SA architecture outperforms the fixed SA architecture in terms of performance. This is because the number of switches necessary increases linearly with the number of transmit antennas. Using a partially dynamic SA structure can reduce the complexity compared to a dynamic SA approach [84]. In [78], two low-complexity hybrid precoding algorithms were proposed for the fixed SA architecture mm wave MIMO systems. They divide the hybrid precoding matrix into vectors and determine the analog precoding function of each subarray from the first vector of the subarray submatrix. Then, to further enhance the system performance, the resulting hybrid precoding is found through an iterative algorithm. By using group sparse approaches, the authors of [85] propose a joint subarray selection and precoding design scheme. The authors of [86] proposed a low-complexity hybrid precoding scheme for wideband multiuser mm wave systems. A closed-form solution for fully connected hybrid precoding based on OFDM is proposed in [77] for mm wave systems. This solution is then expanded into dynamic fixed SA. In [82]-[83], the issue of dynamic SA that uses switches to adjust the connections between RF chains and subarrays was investigated.

Most researchers in the literature only designed FA hybrid precoding/combining or SA hybrid precoding/combining. To the best of our knowledge, no work deals with converting hybrid precoding/combining of the FA structure to SA structure, which is the goal of this chapter, and the resulting architecture is called the Full array to Sub-array architecture (FS). The proposed FS technique described in this chapter differs significantly from the conventional SA in that the latter solves all subarray suboptimization problems to determine the hybrid precoding/combining of the SA architecture, whereas our proposed approach only solves the optimization problem of the hybrid precoding/combining in the FA architecture and then transforms the resulting hybrid precoder/ combiner directly into the SA architecture.

The main contributions of this work are summarized as follows:

- An efficient FS approach to find the hybrid precoding/combining is proposed and its system model is derived for mm wave MIMO communication systems. The suggested approach directly converts the hybrid precoding/combining of the FA architecture into SA architecture.
- The problem formulation of hybrid precoding/combining in the FS is discussed and optimization problem is solved. Our design approach is general, and it would be suitable

to convert the existing hybrid precoding/combining in the FA architecture into SA architecture.

- This chapter proposes an iterative hybrid precoding/combining scheme for the FS architecture. It is called direct conversion of iterative hybrid precoding/ combining from FA to SA (DCIFS). In the design derivation, the proposed DCIFS scheme takes into account the matrix structure of the analog and baseband precoding/combining. It also solves the optimization problem of the hybrid precoding/combining for FA architecture iteratively and converts it into SA architecture.
- The proposed DCIFS hybrid precoding/combining scheme was evaluated by simulations. Results show that the developed hybrid precoding and combining design outperforms the existing SA architecture and provides a performance close to that of the FA architecture and with low complexity.

6.1 System Models and Problem Formulation

Consider a single user mm wave hybrid precoding system, in which a base station equipped with N_t antennas and N_{tRF} RF chains serves a single mobile station with N_r antennas and N_{rRF} RF chains. The base station transmits N_s independent data streams. In this section we develop the mathematical framework for the system models of the FA, the SA, and the FS architectures. Figure 6.1 shows the block diagram of the hybrid precoding in the FA and SA architecture.

A. FA Architecture

A system model of the FA architecture was described previously in chapter 2 in hybrid beamforming solutions.

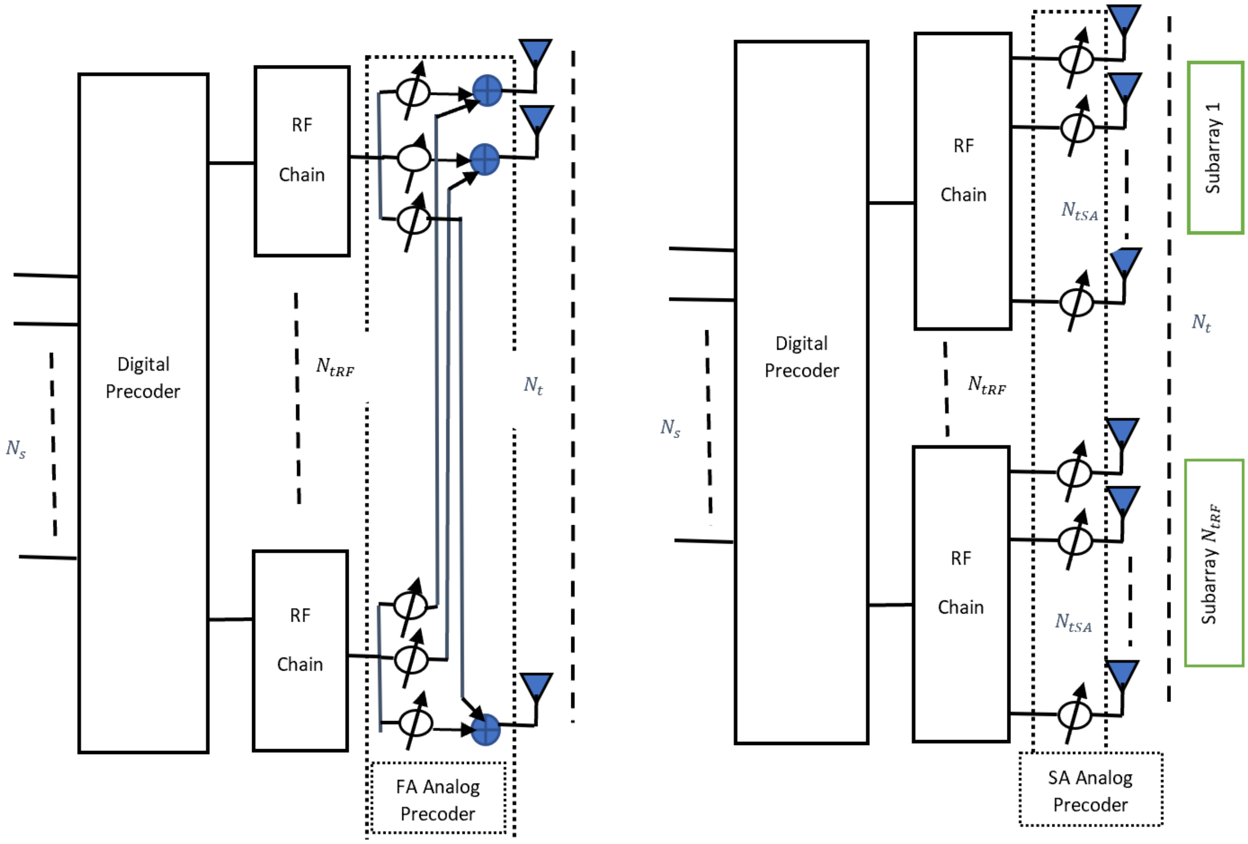

(a)

(b)

Figure 6. 1 Hybrid Precoding at the BS. (a) FA architecture. (b) SA Architecture

B. SA Architecture

In this subsection, a system model of the SA architecture is described and the received signal of the SA can be written as follows

$$\mathrm{y} = \sqrt{\rho}\mathbf{W_D}^{\mathbf{H}}\mathbf{W_{ASA}}^{\mathbf{H}}\mathbf{H}\mathbf{P_{ASA}}\mathbf{P_D}\mathrm{s} + \mathrm{n} \qquad (6.1)$$

where $\mathbf{P_{ASA}}$ is the analog precoding matrix and $\mathbf{W_{ASA}}$ is the analog combining matrix of the SA architecture. Also, $\mathbf{P_D}$ is the digital precoding matrix and $\mathbf{W_D}$ is the digital combining matrix of the SA architecture. For SA architecture, $\mathbf{P_{ASA}}$ and $\mathbf{W_{ASA}}$ can be expressed as

$$\mathbf{P_{ASA}} = \begin{bmatrix} \mathrm{p_{A1}} & 0_{\mathrm{N_{tSA}}\times 1} & \cdots & 0_{\mathrm{N_{tSA}}\times 1} \\ 0_{\mathrm{N_{tSA}}\times 1} & \mathrm{p_{A2}} & \cdots & \vdots \\ \vdots & \vdots & \ddots & 0_{\mathrm{N_{tSA}}\times 1} \\ 0_{\mathrm{N_{tSA}}\times 1} & \cdots & 0_{\mathrm{N_{tSA}}\times 1} & \mathrm{p_{AN_{tRF}}} \end{bmatrix} \tag{6.2}$$

and

$$\mathbf{W_{ASA}} = \begin{bmatrix} \mathrm{w_{A1}} & 0_{\mathrm{N_{rSA}}\times 1} & \cdots & 0_{\mathrm{N_{rSA}}\times 1} \\ 0_{\mathrm{N_{rSA}}\times 1} & \mathrm{w_{A2}} & \cdots & \vdots \\ \vdots & \vdots & \ddots & 0_{\mathrm{N_{rSA}}\times 1} \\ 0_{\mathrm{N_{rSA}}\times 1} & \cdots & 0_{\mathrm{N_{rSA}}\times 1} & \mathrm{w_{AN_{rRF}}} \end{bmatrix} \tag{6.3}$$

where $\mathrm{p_{Al}}$ is the $N_{tSA} \times 1$ analog precoding vector of the lth subarray $(l = 1, 2, \ldots\ldots, N_{tRF})$ whose elements have the same amplitude $1/\sqrt{N_{tSA}}$ but different phases. $\mathrm{w_{Al}}$ represents the $N_{rSA} \times 1$ analog combining vector of the lth subarray $(l = 1, 2, \ldots\ldots, N_{rRF})$ whose elements have the same amplitude $1/\sqrt{N_{rSA}}$ but different phases. $N_{tSA} = N_t/N_{tRF}$ and $N_{rSA} = N_r/N_{rRF}$ are the number of elements in each SA at the transmitter and at the receiver, respectively.

The optimization problem of the lth subarray can be written as [78]

$$\begin{aligned} \left(\mathrm{p_{Al}^{opt}}, \mathrm{p_{Dl}^{opt}}\right) = & \underset{\mathrm{p_{Al}},\, \mathrm{p_{Dl}}}{\mathbf{arg\,min}} \left\|\mathbf{P_l^{opt}} - \mathrm{p_{Al}p_{Dl}}\right\|_{\mathbf{F}}^{\mathbf{2}} \\ \mathbf{st.}\ & \mathrm{p_{Al}} \in \overline{\boldsymbol{\mathcal{F}}}_{\mathbf{A}} \quad , \\ & \|\mathbf{P_{ASA}P_D}\|_{\mathrm{F}}^{\mathbf{2}} = \boldsymbol{N_s} \end{aligned} \tag{6.4}$$

where $\mathbf{P_l^{opt}} = \mathbf{V}_{\mathbf{1},l}$ is the optimum unconstrained digital precoding solution of the *lth* subarray. p_{Dl} is the *lth* row of the $\mathbf{P_D}$. $\overline{\boldsymbol{\mathcal{F}}}_{\mathbf{A}}$ includes all possible $N_{tSA} \times 1$ vectors satisfying the amplitude constraint. The solution of this problem was discussed in detail in [78].

C. The Proposed FS Architecture

In this subsection, an efficient FS system model to convert the FA architecture into SA architecture is introduced. At the receiver side, the received signal can be given as

$$\mathrm{y} = \sqrt{\rho}\mathbf{W_D}^{\mathbf{H}}\mathbf{W_{AFS}}^{\mathbf{H}}\mathbf{H}\mathbf{P_{AFS}}\mathbf{P_D}\mathrm{s} + \mathrm{n} \tag{6.5}$$

where $\mathbf{P_{AFS}}$ and $\mathbf{W_{AFS}}$ are the analog precoding and combining matrices of the proposed FS architecture.

In the proposed FS model, $\mathbf{P_{AFS}}$ and $\mathbf{W_{AFS}}$ can be expressed as

$$\mathbf{P_{AFS}} = \mathbf{P_{AFA}} \odot \mathbf{T_{PFS}}, \text{ and } \mathbf{W_{AFS}} = \mathbf{W_{AFA}} \odot \mathbf{T_{WFS}} \tag{6.6}$$

where $\mathbf{T_{AFS}}$ and $\mathbf{T_{WFS}}$ are the transformation matrices that are used to transform the FA architecture into SA architecture and their dimensions are the same as that of $\mathbf{P_{AFA}}$ and $\mathbf{P_{WFA}}$. $\odot$ is the element-wise multiplication. $\mathbf{T_{AFS}}$ and $\mathbf{T_{WFS}}$ can be given as

$$\mathbf{T_{PFS}} = \begin{bmatrix} 1_{\mathrm{N_{tSA}}\times 1} & 0_{\mathrm{N_{tSA}}\times 1} & \cdots & 0_{\mathrm{N_{tSA}}\times 1} \\ 0_{\mathrm{N_{tSA}}\times 1} & 1_{\mathrm{N_{tSA}}\times 1} & \cdots & \vdots \\ \vdots & \vdots & \ddots & 0_{\mathrm{N_{tSA}}\times 1} \\ 0_{\mathrm{N_{tSA}}\times 1} & \cdots & 0_{\mathrm{N_{tSA}}\times 1} & 1_{\mathrm{N_{tSA}}\times 1} \end{bmatrix} \tag{6.7}$$

and

$$\mathbf{T_{WFS}} = \begin{bmatrix} 1_{\mathrm{N_{rSA}}\times 1} & 0_{\mathrm{N_{rSA}}\times 1} & \cdots & 0_{\mathrm{N_{rSA}}\times 1} \\ 0_{\mathrm{N_{rSA}}\times 1} & 1_{\mathrm{N_{rSA}}\times 1} & \cdots & \vdots \\ \vdots & \vdots & \ddots & 0_{\mathrm{N_{rSA}}\times 1} \\ 0_{\mathrm{N_{rSA}}\times 1} & \cdots & 0_{\mathrm{N_{rSA}}\times 11} & 1_{\mathrm{N_{rSA}}\times 1} \end{bmatrix}$$

where $1_{N_{rSA}\times 1}$ and $0_{N_{rSA}\times 1}$ are an $N_{rSA} \times 1$ vectors of ones and zeros, respectively. The problem formulation of the hybrid precoding/combining FS architecture will be discussed and solved in the next section.

6.2 The Proposed DCIFS Hybrid Precoding/Combining Algorithm

In this subsection, we propose the low complexity DCIFS hybrid precoding/combining algorithm that works on FS system model. Only the precoder's derivation is discussed, and the derivation of the combiner is similar. We note that the optimal unconstrained semi-unitary precoder for $\mathbf{H}$ is simply given by $\mathbf{P}_{\mathbf{FA}}^{\mathbf{opt}} = \mathbf{V}_{\mathbf{1}}$, where $\mathbf{V}_{\mathbf{1}}^{\mathbf{H}}\,\mathbf{V}_{\mathbf{1}} = \mathbf{I}_{\mathbf{N}_{\mathbf{s}}}$. Also, we need the hybrid precoder $\mathbf{P}_{\mathbf{AFS}}\mathbf{P}_{\mathbf{D}}$ to be sufficiently "close" to the optimal precoder $\mathbf{V}_{\mathbf{1}}$ by using its digital precoder to construct linear combinations of the RF precoder vectors. By knowing that the structure of $\mathbf{P}_{\mathbf{AFS}}$ is a semi-diagonal matrix, this matrix is totally non-square semi-unitary after its element-wise normalization, i.e., $\mathbf{P}_{\mathbf{AFS}}^{\mathbf{H}}\,\mathbf{P}_{\mathbf{AFS}} = \mathbf{I}_{\mathbf{N}_{\mathbf{tRF}}}$. In addition, the digital precoding $\mathbf{P}_{\mathbf{D}}$ can be totally unitary $\mathbf{P}_{\mathbf{D}}^{\mathbf{H}}\mathbf{P}_{\mathbf{D}} = \mathbf{P}_{\mathbf{D}}\mathbf{P}_{\mathbf{D}}^{\mathbf{H}} = \mathbf{I}_{\mathbf{N}_{\mathbf{S}}}$ or a non-square matrix that is totally semi-unitary $\mathbf{P}_{\mathbf{D}}^{\mathbf{H}}\mathbf{P}_{\mathbf{D}} = \mathbf{I}_{\mathbf{N}_{\mathbf{s}}}$. This structure will be reflected in solving the optimization problem to make the hybrid precoder $\mathbf{P}_{\mathbf{AFS}}\mathbf{P}_{\mathbf{D}}$ sufficiently "close" to the optimal precoder $\mathbf{V}_{\mathbf{1}}$ since the optimal unconstrained precoder $\mathbf{V}_{\mathbf{1}}$ is semi-unitary matrix. Thus, by knowing this information about hybrid precoder $\mathbf{P}_{\mathbf{AFS}}\mathbf{P}_{\mathbf{D}}$, we need to solve the following optimization problem

$$\left(\mathbf{P}_{\mathbf{AFS}}^{\mathbf{opt}}, \mathbf{P}_{\mathbf{D}}^{\mathbf{opt}}\right) = \underset{\mathbf{P}_{\mathbf{AFS}},\ \mathbf{P}_{\mathbf{D}}}{\arg\ min} \left\|\mathbf{P}_{\mathbf{FA}}^{\mathbf{opt}} - \mathbf{P}_{\mathbf{AFS}}\mathbf{P}_{\mathbf{D}}\right\|_F^2 \qquad (6.8)$$

$$st. \quad \mathbf{P}_{\mathbf{AFS}} \in \mathcal{F}_{\mathbf{AFA}} ,$$

$$\mathbf{P}_{\mathbf{AFS}}^{\mathbf{H}}\,\mathbf{P}_{\mathbf{AFS}} = \mathbf{I}_{\mathbf{N}_{\mathbf{tRF}}} \text{ and } \mathbf{P}_{\mathbf{D}}^{\mathbf{H}}\mathbf{P}_{\mathbf{D}} = \mathbf{I}_{\mathbf{N}_{\mathbf{s}}}$$

$$\|\mathbf{P}_{\mathbf{AFS}}\mathbf{P}_{\mathbf{D}}\|_F^2 = N_s$$

The problem (6.8) is non-convex optimization problem with a difficult optimal solution. However, by knowing that the structure of $\mathbf{P}_{\mathbf{AFS}}$ is totally non-square semi-unitary and assuming $\mathbf{P}_{\mathbf{D}}$ is totally unitary or semi-unitary matrix, the iterative solution to (6.8) can be obtained by solving the following optimization problem

$$\left(\mathbf{P}_{\mathbf{AFS}}^{\mathbf{opt}}, \mathbf{P}_{\mathbf{D}}^{\mathbf{opt}}\right) = \underset{\mathbf{P}_{\mathbf{AFS}},\ \mathbf{P}_{\mathbf{D}}}{\arg\ min} \left\| \mathbf{P}_{\mathbf{FA}}^{\mathbf{opt}} - \mathbf{P}_{\mathbf{AFS}}\mathbf{P}_{\mathbf{D}} \right\|_F^2 \tag{6.9}$$

we first need to find the baseband precoder $\mathbf{P}_{\mathbf{D}}$ that minimizes the Euclidean distance by using the initialization of the proposed RF precoder $\mathbf{P}_{\mathbf{AFS}}$, which is calculated by taking the first N_{tRF} columns from $\mathbf{P}_{\mathbf{FA}}^{\mathbf{opt}}$ and then normalizing them such that each entry has constant magnitude, i.e., $\mathbf{P}_{\mathbf{AFS}} = (\ \mathbf{P}_{\mathbf{FA}}^{\mathbf{opt}}\ \oslash \left(\left|\mathbf{P}_{\mathbf{FA}}^{\mathbf{opt}}\right| \sqrt{N_{tSA}}\right)) \odot \mathbf{T}_{\mathbf{PFS}}$. One should note that the element-wise normalization of $\mathbf{P}_{\mathbf{AFS}}$ satisfies the normalization constraint $\left|[\mathbf{P}_{\mathbf{AFS}}\ ]_{\mathrm{i,j}}\right|^2 = {}^{1}\!/_{N_{tSA}}$. We then find the RF precoder $\mathbf{P}_{\mathbf{AFS}}$ such that the hybrid precoder $\mathbf{P}_{\mathbf{AFS}}\mathbf{P}_{\mathbf{D}}$ is sufficiently "close" to the optimal unconstrained digital precoder $\mathbf{V}_{\mathbf{1}}$. Specifically, we would like to solve the following optimization problem first, which is related to (6.9):

$$\left(\mathbf{P}_{\mathbf{D}}^{\mathbf{opt}}\right) = \arg \min_{\mathbf{P}_{\mathbf{D}}} \left\| \mathbf{P}_{\mathbf{FA}}^{\mathbf{opt}} - \ \mathbf{P}_{\mathbf{AFS}}\mathbf{P}_{\mathbf{D}} \right\|_F^2 \tag{6.10}$$

The objective function can be expanded as

$$\left\| \mathbf{P}_{\mathbf{FA}}^{\mathbf{opt}} - \ \mathbf{P}_{\mathbf{AFS}}\mathbf{P}_{\mathbf{D}} \right\|_F^2 \tag{6.11}$$

$$= \mathrm{tr}\left(\mathbf{P}_{\mathbf{FA}}^{\mathbf{opt}^{\mathbf{H}}} \mathbf{P}_{\mathbf{FA}}^{\mathbf{opt}}\right) - 2\mathrm{tr}\left(\mathbf{P}_{\mathbf{FA}}^{\mathbf{opt}^{\mathbf{H}}} \mathbf{P}_{\mathbf{AFS}}\mathbf{P}_{\mathbf{D}}\right) + \|\mathbf{P}_{\mathbf{AFS}}\mathbf{P}_{\mathbf{D}}\|_F^2$$

$$= 2N_S - 2\mathrm{tr}\left(\mathbf{P}_{\mathbf{FA}}^{\mathbf{opt}^{\mathbf{H}}} \mathbf{P}_{\mathbf{AFS}}\mathbf{P}_{\mathbf{D}}\right)$$

The solution of this problem, which is to find the maximization of $\mathbf{P}_{\mathbf{FA}}^{\mathbf{opt}^{\mathbf{H}}} \mathbf{P}_{\mathbf{AFS}}\mathbf{P}_{\mathbf{D}}$ is solved by what is called the orthonormal Procrustes problem [87] as follows

$$\mathbf{P_D} = \mathbf{V}\mathbf{U}^{\mathbf{H}} \tag{6.12}$$

where $\mathbf{P_{FA}^{opt}}^{\mathbf{H}}\mathbf{P_{AFS}} = \mathbf{U\Sigma V^H}$. Then, we keep $\mathbf{P_D}$ fixed and solve the same optimization problem but now minimizing over $\mathbf{P_{AFS}}$ as follows:

$$\left(\mathbf{P_{AFS}^{opt}}\right) = \arg\min_{\mathbf{P_{AFS}}}\left\|\mathbf{P_{FA}^{opt}} - \mathbf{P_{AFS}}\mathbf{P_D}\right\|_F^2 \tag{6.13}$$

Similar to (6.10), expanding the objective function yields

$$\left\|\mathbf{P_{FA}^{opt}} - \mathbf{P_{AFS}}\mathbf{P_D}\right\|_F^2 \tag{6.14}$$

$$= 2N_S - 2\mathrm{tr}\left(\mathbf{P_{FA}^{opt}}^{\mathbf{H}}\mathbf{P_{AFS}}\mathbf{P_D}\right)$$

Given that the optimal unconstrained matrix $\mathbf{V_1}$ is totally semi-unitary and the digital precoding $\mathbf{P_D}$ is totally unitary or semi-unitary non-square matrix, the solution that maximize $\mathbf{P_{FA}^{opt}}^{\mathbf{H}}\mathbf{P_{AFS}}\mathbf{P_D}$ in (6.14) is given as follows

$$\mathbf{P_{AFS}} = \mathbf{P_{FA}^{opt}}\mathbf{P_D}^{\mathbf{H}} \tag{6.15}$$

The main difference between the hybrid design in this chapter and that in [28] is that our design is more general, and can work in all scenarios whether the number of data streams equals the number of RF chains or the number of data streams is smaller than the number of RF chains. However, HD-AM can only work when the number of data streams equals the number of RF chains. Furthermore, our derivation is based on the SA architecture and thanks to the structure of $\mathbf{P_{AFS}}$, which is totally non-square semi-unitary matrix. HD-AM, on the other hand, is derived only for the FA architecture.

The pseudo-code for the proposed DCIFS hybrid precoder $\mathbf{P_{FS}}$ solution is given in Algorithm 6.1. The inputs of the algorithm are $\mathbf{P_{FA}^{opt}} \in C^{N_t \times N_S}$, initialized analog procoder $\mathbf{P_{AFS}} \in C^{N_t \times N_{tRF}}$

i.e., $\mathbf{P_{AFS}} = \left(\mathbf{P_{FA}^{opt}} \oslash \left(|\mathbf{P_{FA}^{opt}}|\sqrt{N_{tSA}} \right)\right) \odot \mathbf{T_{PFS}}$, and the maximum number of iterations K, where $K \geq 1$ for $N_S < N_{tRF}$ or $N_{rRF} = N_S$. In the general case of $N_S \geq 1$ where $N_S \leq N_{tRF}$, the algorithm starts by computing $\mathbf{P_D}$ using the orthonormal Procrustes solution in step 2. After that, the algorithm proceeds to update the proposed RF precoder $\mathbf{P_{AFS}}$ in steps 3. Step 4 ensures that the proposed RF precoder $\mathbf{P_{AFS}}$ is satisfied exactly with constant-magnitude entries which can be applied at RF using analog phase shifters. In step 5, we make sure that $\mathbf{P_{AFS}}$ still has the subarray structure. After the last iteration of the algorithm, $\mathbf{P_D}$ is updated via the maximal ratio combining (MRC) instead of the least squares solution which has an impact on Frobenius norm objective function [4]. Based on our results, step 7 reduces the Frobenius norm objective function $\left\|\mathbf{P_{FA}^{opt}} - \mathbf{P_{AFS}}\mathbf{P_D}\right\|_F$ because the least squares solution becomes MRC after implementing the semi-unitary FS analog precoder, i.e., $\mathbf{P_{AFS}^H}\,\mathbf{P_{AFS}} = \mathbf{I_{N_{tRF}}}$. After K iterations the process is completed and the algorithm will find the N_t x N_{tRF} proposed RF precoding matrix $\mathbf{P_{AFS}}$ and the optimal N_{tRF} x N_S baseband precoder $\mathbf{P_D}$ such that $\left\|\mathbf{P_{FA}^{opt}} - \mathbf{P_{AFS}}\mathbf{P_D}\right\|_F$ is minimized. In steps 8 and 9, we ensure that the transmit power constraint is satisfied and return the proposed hybrid precoder $\mathbf{P_{FS}} = \mathbf{P_{AFS}}\mathbf{P_D}$. The proposed DCIFS hybrid combiner $\mathbf{W_{FS}}$ can be calculated in the same way.

Algorithm 6. 1: Proposed DCIFS Hybrid Precoding

Input: The optimum unconstrained solution $\mathbf{P_{FA}^{opt}} \in C^{N_t \times N_S}$, initialized analog precoder $\mathbf{P_{AFS}} \in C^{N_t \times N_{tRF}}$ with the element-wise normalization, and the maximum number of iterations K.

Output: Analog $\mathbf{P_{AFS}} \in C^{N_t \times N_{tRF}}$ with the element-wise normalization and baseband $\mathbf{P_D} \in C^{N_{tRF} \times N_S}$ such that $\left\|\mathbf{P_{FA}^{opt}} - \mathbf{P_{FS}}\right\|_F$ is reduced and $\|\mathbf{P_{FS}}\|_F^2 = N_S$, where $\mathbf{P_{FS}} = \mathbf{P_{AFS}}\mathbf{P_D}$.

```
for $i = 1{:}K$ do
    Update: $\mathbf{P_D} = \mathbf{VU^H}$, where $\mathbf{P_{FA}^{opt}}^{\mathbf{H}}\mathbf{P_{AFS}} = \mathbf{U\Sigma V^H}$
    Update: $\mathbf{P_{AFA}} = \mathbf{P_{FA}^{opt}}\mathbf{P_D}^{\mathbf{H}}$
    Element-Wise Normalization: $\mathbf{P_{AFS}} = \mathbf{P_{AFA}} \oslash \left(|\mathbf{P_{AFA}}|\sqrt{N_{tSA}}\right)$
    $\mathbf{P_{AFS}} = \mathbf{P_{AFA}} \odot \mathbf{T_{PFS}}$
end for
$\mathbf{P_D} = \mathbf{P_{AFS}}^{\mathbf{H}}\mathbf{P_{FA}^{opt}}$
$\mathbf{P_D} = \sqrt{N_S}\frac{\mathbf{P_D}}{\|\mathbf{P_{AFS}}\,\mathbf{P_D}\|_F}$
Return $\mathbf{P_{FS}} = \mathbf{P_{AFS}}\mathbf{P_D}$.
```

6.3 Complexity Analysis of the Proposed Algorithm

In this section, we analyze the complexity in implementing the proposed DCIFS hybrid precoding/combining design using Algorithm 6.1. To simplify the complexity analysis, let us denote $N = \max\{N_t, N_r\}$, $N_{\text{RF}} = \max\{N_{tRF}, N_{rRF}\}$, $N_{\text{SA}} = \max\{N_{tSA}, N_{rSA}\}$ and K is the maximum number of iterations of the proposed hybrid design, HD-AM design [28], and SA hybrid design [78]. In this section, we present the complexity analysis by evaluating the total number of floating-point operations (flops) for each hybrid precoding/combining approach.

The primary factor in the sparse hybrid precoder/combiner design algorithm's complexity depends on the squared maximum number of antennas. The complexity increases nonlinearly when the maximum number of antennas increases. Thus, as we see in table 6.1, the complexities of the proposed DCIFS hybrid design, SA hybrid design [78], IFA hybrid design [46], and HD-AM hybrid design [28] are very low compared to that of the sparse hybrid precoding [8], which requires $\text{O}(N^2 N_{RF} N_S)$. Also, the computational complexities of proposed DCIFS hybrid design, SA hybrid design, IFA Hybrid Design, and HD-AM are almost the same, especially when $N \ll N_S$. In terms of the hardware complexity, the proposed DCIFS hybrid design, and the SA hybrid design require lower hardware cost compared to the sparse hybrid design, IFA hybrid design, and HD-AM hybrid design; the number of the required phase shifters with the proposed DCIFS hybrid design, and SA hybrid design is N, whereas the other methods require NN_{RF}. Thus, this concludes that the proposed DCIFS hybrid design has lower computational and hardware complexities than the FA hybrid design.

TABLE 6. 1. Complexity of the proposed algorithm compared to previous methods from the literature.

Method	**Constraints**	**Number of Phase Shifters**	**Complexity**
Sparse Hybrid Design [8]	RF precoding/Combining codebooks	NN_{RF}	$\mathrm{O}(N^2 N_{RF} N_S)$
HD-AM Hybrid Design [28]	$N_S = N_{\mathrm{RF}}$	NN_{RF}	$\mathrm{O}(NN_S^2 K)$
IFA Hybrid Design [46]	None	NN_{RF}	$\mathrm{O}(NN_{RF}^2 K)$
SA Hybrid Design [78]	None	N	$\mathrm{O}(N_{\mathrm{SA}} N_{\mathrm{RF}} N_S K)$
Proposed DCIFS Hybrid Design	None	N	$\mathrm{O}(NN_{\mathrm{RF}} N_S K)$

6.4 Simulation Results

This section presents the numerical results to show the performance advantages of the proposed hybrid precoding/combining implemented as described in Algorithm 6.1. Specifically, we show numerical simulations of the proposed methods' performance when maximizing the spectral efficiency as defined in (2.40).

In these simulations, we use the system architecture presented in Fig. 6.1. We consider the case where there is only one BS and one MS at a distance of 100 meters. The spacing between antenna elements is equal to $\lambda/2$. The system is assumed to operate at a 28 GHz carrier frequency in an outdoor scenario, and with a path loss exponent $n = 3.4$. The channel model is described in (2.34), with $\overline{\mathrm{P}_{\alpha,\mathrm{l}}} = 1$ for all clusters. The azimuth and elevation angles AoAs/AoDs of the rays within a cluster are assumed to be randomly Laplacian distributed. The AoAs/AoDs azimuths and elevations of the cluster means are assumed to be uniformly distributed. We use the AoD/AoA beamforming codebooks (exact array response of mm wave channel) at the BSs and MSs, respectively for the sparse hybrid design. The *SNR* in all the plots is defined as $SNR = \rho/\sigma^2$. We assume perfect CSI at the BS and MS. For fairness, the same total power constraint is enforced on all precoding/combining solutions.

We divide our results into two scenarios. The first scenario presents the results of implementing the DCIFS hybrid precoding design using Algorithm 6.1 at the BS, and IFA hybrid combining design [46] at the MS. Then, the second scenario shows the results by using the DCIFS hybrid design at both the BS and the MS. For fairness comparison, we proceed similarly to the subarray iterative hybrid design [78]. For both scenarios, we compare the proposed DCIFS hybrid design with the FA sparse hybrid design [8], IFA hybrid design [46], optimal unconstrained digital method, and the SA hybrid design [78].

(a) DCIFS Hybrid Precoding Design at the BS, and Iterative FA Hybrid combining Design at the MS.

Fig. 6.2 shows the spectral efficiency achieved by the proposed hybrid DCIFS design, the FA sparse hybrid design [8], the optimal unconstrained digital design, IFA hybrid design [46], and the SA hybrid design [78] in a 144 x 64 UPAs mm wave system for different *SNR* values with $N_S \in$

$\{1,2,3\}$, and $N_{tRF} = N_{rRF} = 4$. The maximum number of iterations K for the proposed DCIFS hybrid design and the SA hybrid design is equal to 1, and 10 for all data streams N_S. In addition, the maximum number of iterations K for IFA hybrid precoding/combining design is 10 for all data streams and for all cases. The proposed DCIFS hybrid design and the SA hybrid design outperform the FA sparse hybrid design, regardless of the number of data streams N_S. The proposed DCIFS hybrid design overlaps the SA hybrid design for any number of data streams with any number of iterations K and both achieve the optimal performance of the unconstrained digital design for $N_S = 1$, and 2. However, when $N_S = 3$, the IFA hybrid design outperforms the proposed DCIFS, and the SA hybrid design.

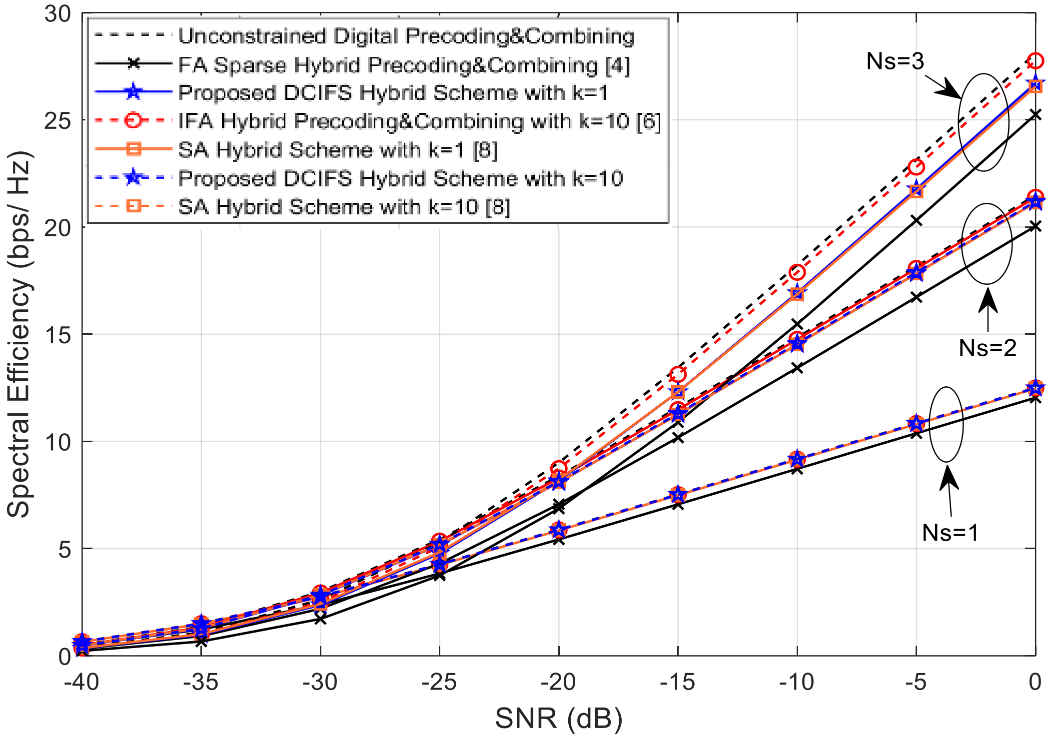

Figure 6. 2 Average spectral efficiency achieved by the proposed DCIFS hybrid design with K=1, and 10 compared to the FA sparse hybrid precoders/combiners design [8], the optimal unconstrained digital precoders/combiners, IFA hybrid precoders/combiners design [46], and the SA hybrid design [78] for a 144 x 64 UPAs mm wave systems for different SNR values with $N_S \in \{1,2,\ 3\}$, and $N_{tRF} = N_{rRF} = 4$.

When the number of RF chains equals the number of data streams, Fig. 6.3 shows the spectral efficiency achieved by the proposed DCIFS hybrid design with $K = 1, \text{and } 10$, the FA sparse hybrid precoders/combiners, the optimal unconstrained digital precoders/combiners, IFA hybrid design with $K = 10$, and the SA hybrid design with $K = 1, \text{and } 10$ for different numbers of RF chains and data streams varying from 1 to 4 in a 144 x 64 UPAs mm wave systems where $N_S = N_{tRF} = N_{rRF}$. The *SNR* is fixed to 0 dB for any number of RF chains. We can see that the proposed DCIFS hybrid design and the SA hybrid design are overlapped when $N_S = N_{tRF} = N_{rRF} = 1, \text{and } 2$; also, they yield an improvement over the FA sparse hybrid design, and both achieve a performance close to the IFA hybrid design for any number of iterations. However, when $N_S = N_{tRF} = N_{rRF} = 4$, the overall performance of the proposed DCIFS and SA hybrid design is degraded because of the data streams interference; the proposed DCIFS design with *K*=10 outperforms the FA sparse hybrid design whereas the SA hybrid design with K=10 overlaps with the FA sparse hybrid design. The proposed DCIFS hybrid design outperforms the SA hybrid design when the number of RF chains equals to 4 for any number of iterations K.

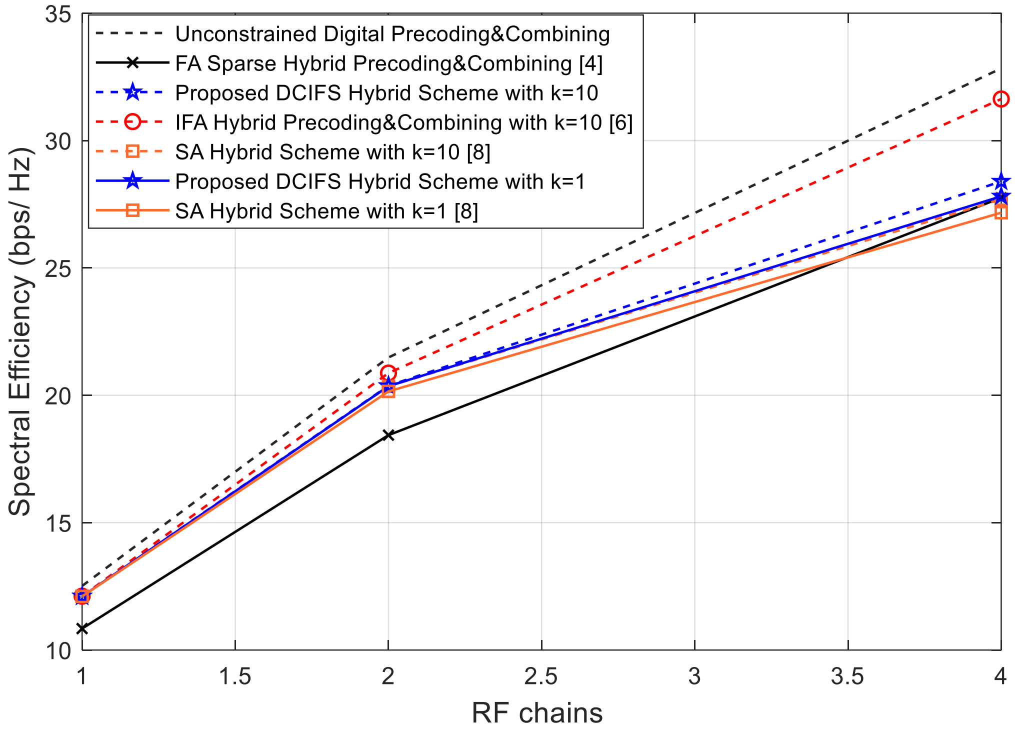

Figure 6. 3 Average spectral efficiency achieved by the proposed DCIFS hybrid design with different K compared to the full array sparse hybrid precoders/combiners [8], the optimal unconstrained digital precoders/combiners, IFA hybrid precoders/combiners [46] with K =10, and the SA hybrid design [78] with different K in 144 x 64 UPAs mm wave systems for SNR = 0 dB with $N_S = N_{tRF} = N_{tRF}$.

Fig.6.4 evaluates the performance when the number of RF chains is greater than the number of data streams, where $N_S \in \{1,2,4\}$ and the *SNR* is fixed to 0 dB over the whole range of RF chains. The proposed DCIFS hybrid design and the SA hybrid design perform better than the full array sparse hybrid method when $N_S = 1,$ and 2 for any number of K with a small difference between K=1, and K=10. The proposed DCIFS hybrid design with $K = 1$ can accurately approximate the optimal unconstrained one when the number of RF chains is twice the number of data streams when $N_S = 1$ and 2. When $N_S = 4$, the performance of the proposed DCIFS is better than the SA hybrid design for any number of K and the FA sparse hybrid design for K=10; however, both design have a degradation compared to the FA sparse hybrid design and the optimal unconstrained design when the number RF chains increases because of the high interference between data streams.

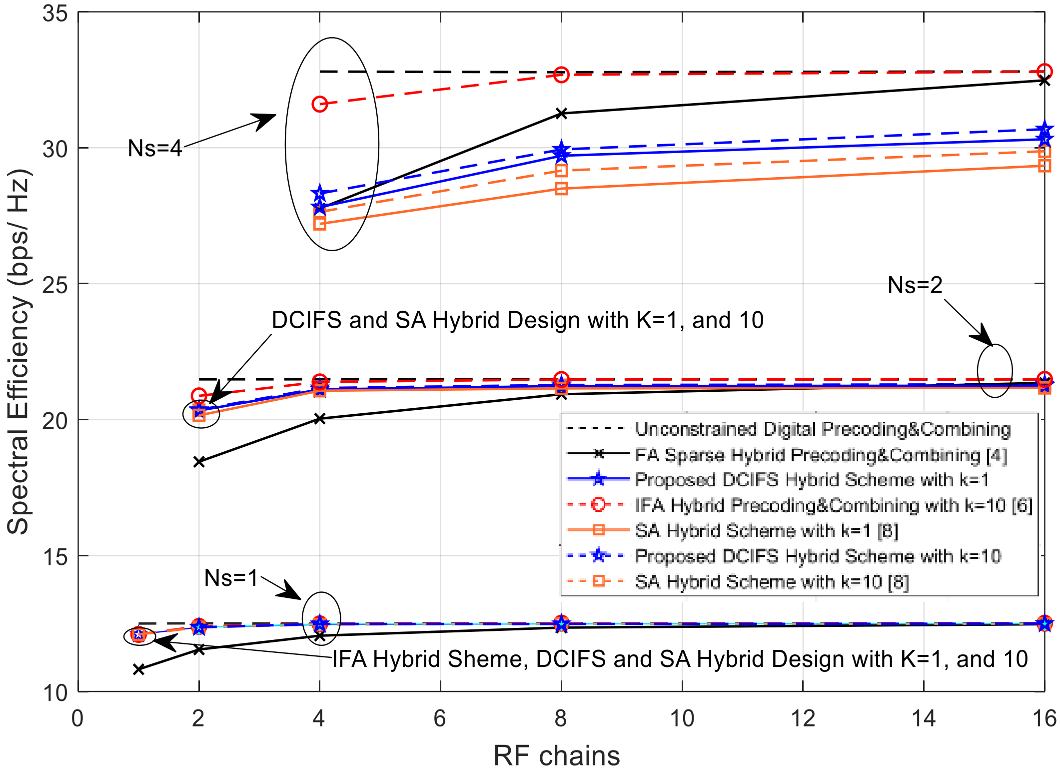

Figure 6. 4 Average spectral efficiency achieved by the proposed DCIFS design with different K compared to the FA sparse hybrid precoders/combiners [8], the optimal unconstrained digital precoders/combiners, IFA hybrid precoders/combiners [46] with K =10, and the SA hybrid design [78] with different K in 144 x 64 UPAs mm wave systems for SNR = 0 dB with $N_S \in \{1,2,4\}$ and different RF chains.

Fig. 6.5 shows the spectral efficiency achieved by the proposed DCIFS hybrid design, the FA sparse hybrid precoding/combining design [8], the optimal unconstrained digital precoding/combining design, IFA hybrid precoding/combining design [46], and the SA hybrid [78] in a UPAs mm wave system for different BS antenna values with $N_r = 64$, SNR = 0 dB, $N_S = 2$, and $N_{tRF} = N_{rRF} = 4$. The maximum number of iterations K for the proposed DCIFS hybrid precoding/combining design and the SA hybrid precoding/combining design is equal to 1 and 10 for all number of BS antenna. In addition, the maximum number of iterations K for IFA hybrid precoding/combining design is 10. The performance of the proposed DCIFS and SA hybrid design is better than the FA sparse hybrid design for all cases. However, the IFA hybrid precoding/combining design outperforms the proposed DCIFS and the SA hybrid design for all cases. The performance of the proposed DCIFS hybrid design is better than the SA hybrid design for smaller number of BS antenna and becomes much better for larger number of BS antenna. The gap between K=1 and K=10 for the proposed DCIFS hybrid design is small for any number of BS antenna. However, the gap between K=1 and K=10 for the SA hybrid design is bigger especially for higher number of BS antenna. Thus, using small number of iterations such as K=1 for the proposed DCIFS hybrid design is enough for any number of BS antenna. The performance of the proposed DCIFS hybrid design with K=1 is the same performance as the SA hybrid design with K=10 which means that our design performs better than the SA design with a very small number of iterations K resulting in a reduced computational complexity.

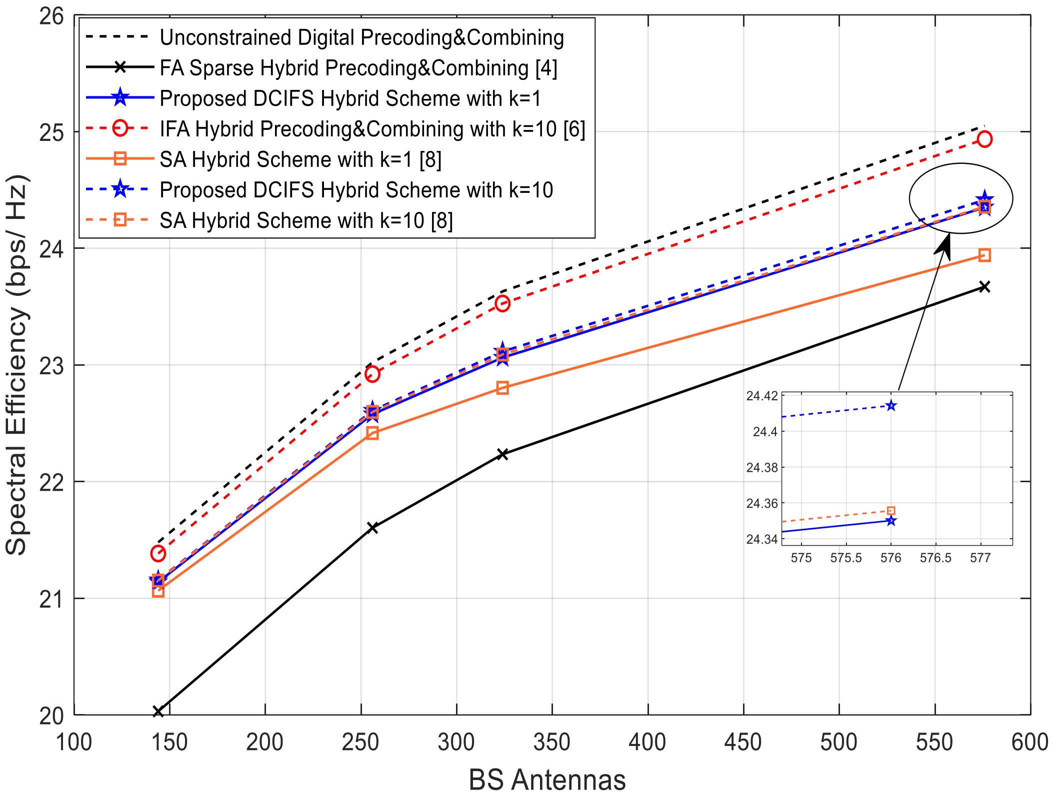

Figure 6. 5 Average spectral efficiency vs the number of BS antenna achieved by the proposed DCIFS design with different K compared to the full array sparse hybrid precoders/combiners [8], the optimal unconstrained digital precoders/combiners, IFA hybrid precoders/combiners [46] with K =10, and the SA hybrid design [78] with different K in UPAs mm wave systems for $N_r = 64$ with SNR = 0 dB, $N_S = 2$ and $N_{tRF} = N_{rRF} = 4$

In Fig 6.6, we utilize the same parameters used in generating Fig 6.5, but we increase the number of data streams to 4. As we can see in Fig 6.6, the IFA still outperforms the other designs. The proposed DCIFS hybrid design outperforms the FA sparse hybrid design for *K*=10 and with small gain when *K*=1. The SA hybrid design performs similarly to the FA sparse design for a small number of BS antennas when *K*=10. However, for larger number of BS antennas, the SA hybrid design has a lower performance for any number of iterations *K*. The gap between *K*=1 and *K*=10 for the proposed DCIFS hybrid design is smaller for any number of BS antenna compared to the gap between *K*=1 and *K*=10 for the SA hybrid design, especially for higher number of BS antenna.

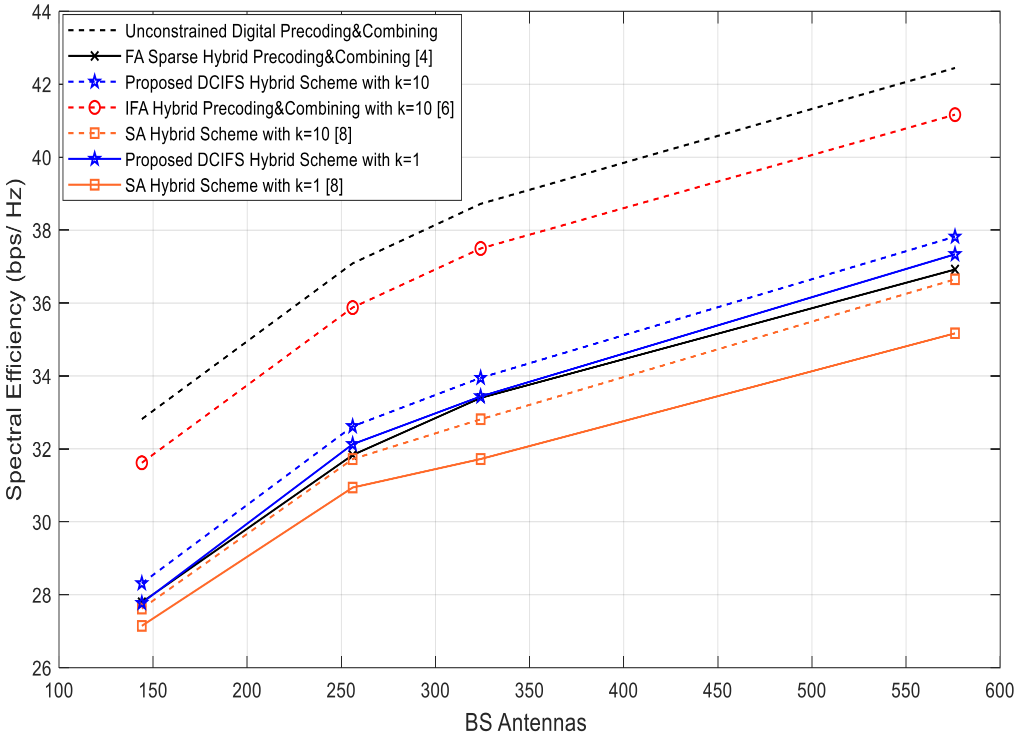

Figure 6. 6 Average spectral efficiency vs the number of BS antenna achieved by the proposed DCIFS design with different K compared to the full array sparse hybrid precoders/combiners [8], the optimal unconstrained digital precoders/combiners, IFA hybrid precoders/combiners [46] with K =10, and the SA hybrid design [78] with different K in UPAs mm wave systems for $N_r = 64$ with SNR = 0 dB, $N_S = 4$ and $N_{tRF} = N_{rRF} = 4$

In conclusion, the structure of the analog and baseband precoding/combining matrices in the proposed DCIFS hybrid design provides a higher gain compared to the FA sparse hybrid design and the SA hybrid design for any number of data streams, especially for a large number of BS antennas with a small number of iterations. The number of iterations should be 10 or less because the gain after that will be very small which is verified by our results that we did not include in this thesis. For a large number of RF chains, more than 4, the proposed DCIFS hybrid design performs poorly when compared to all FA methods where the data streams interferences become small for them. However, in practice, the number of RF chains will be limited because of the high-power consumption and cost per RF chain. The IFA hybrid design outperforms the proposed DCIFS hybrid design for all results, but its hardware complexity is much higher because of a higher number of phase shifters in the BS side.

(b) DCIFS Hybrid Precoding Design at the BS, and DCIFS Hybrid Combining Design at MS.

Fig. 6.7 shows the spectral efficiency achieved by the proposed DCIFS hybrid precoding/combining design, the FA sparse hybrid precoding/combining design [8], the optimal unconstrained digital precoding/combining design, the IFA hybrid precoding/combining design [46], and the SA hybrid precoding/combining design [78] in a 144 x 64 UPAs mm wave system for different SNR values with $N_S \in \{1,2\}$, and $N_{tRF} = N_{rRF} = 4$. The maximum number of iterations K for the proposed DCIFS hybrid precoding/combining design and the SA hybrid precoding/combining design is equal to 1, and 10 for all data streams N_S. In addition, the maximum number of iterations K for IFA hybrid precoding/combining design is 10. The performance of the proposed DCIFS hybrid precoding/combining design and the SA hybrid precoding/combining is close to the optimal unconstrained one and overlapped with the FA sparse hybrid design for $N_S = 1$. However, when $N_S = 2$, the proposed DCIFS hybrid precoding/combining design outperforms the SA hybrid precoding/combining and its performance is close to that of the FA sparse hybrid deign when K=10; the total performance of the proposed DCIFS hybrid precoding/combining design and the SA hybrid precoding/combining design is degraded compared to the results in subsection (a) because of the subarray design in the transmitter and the receiver.

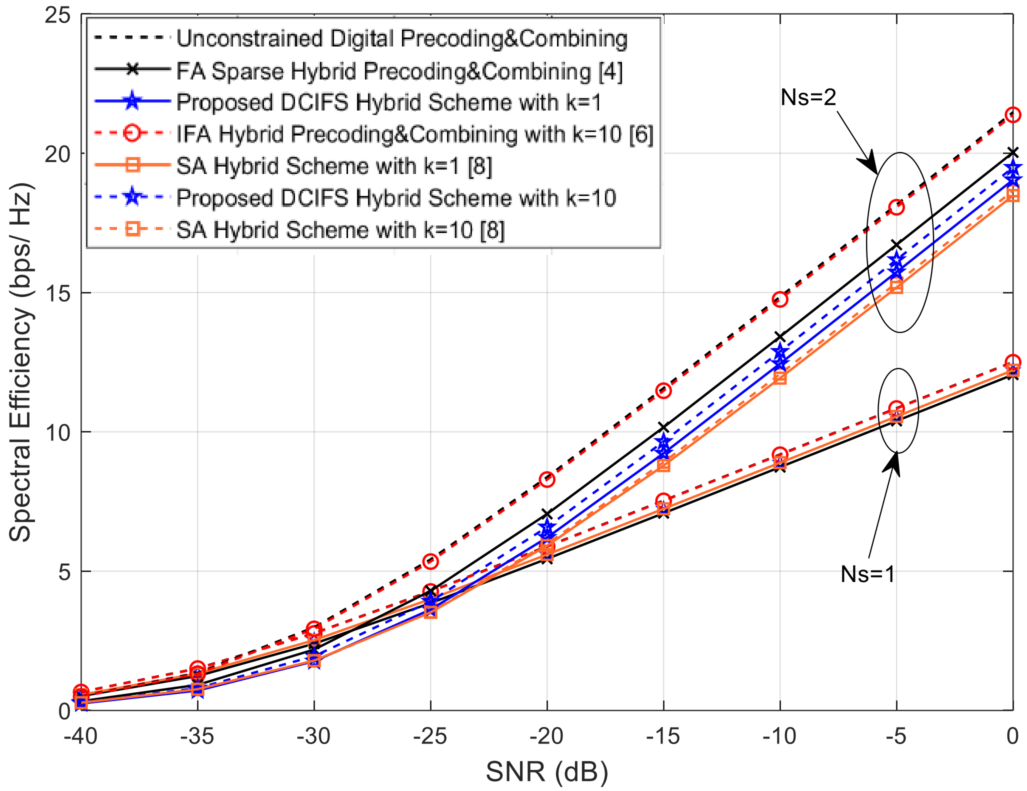

Figure 6. 7 Average spectral efficiency achieved by the proposed DCIFS hybrid design with K=1, and 10 compared to the FA sparse hybrid precoders/combiners design [8], the optimal unconstrained digital precoders/combiners, the IFA hybrid precoders/combiners design [46], and the SA hybrid design [78] for a 144 x 64 UPAs mm wave systems for different SNR values with $N_S \in \{1,2\}$, and $N_{tRF} = N_{rRF} = 4$.

Similar to the previous subsection, we evaluate the performance when the number of RF chains equals the number of data streams. Fig. 6.8 shows the spectral efficiency achieved by the proposed DCIFS hybrid precoding/combining design with $K = 1$, and 10, the FA sparse hybrid precoders/combiners, the optimal unconstrained digital precoders/combiners, the IFA hybrid precoding/combining design with $K = 10$, and the SA hybrid precoding/combining design with $K = 1$, and 10 for different numbers of RF chains and data streams varying from 1 to 4 in a 144 x 64 UPAs mm wave systems where $N_S = N_{tRF} = N_{rRF}$. The SNR is fixed to 0 dB for any number of RF chains. As we see in Fig 6.8, the overall performance of the proposed DCIFS and

SA hybrid precoding/combining design is worse compared to the results in the previous subsection in Fig 6.3; this is because we use the SA architecture in both transmitter and receiver. The data streams interference increases with the data streams resulting in increasing the gap between the proposed DCIFS and SA hybrid precoding/combining design and the other FA designs. The performance of the proposed DCIFS hybrid precoding/combining design overlaps with the performance of the SA hybrid design when $N_S = 1$. However, for a higher number of data streams, the performance of the DCIFS design is much better than that of the SA design for any number of iterations K.

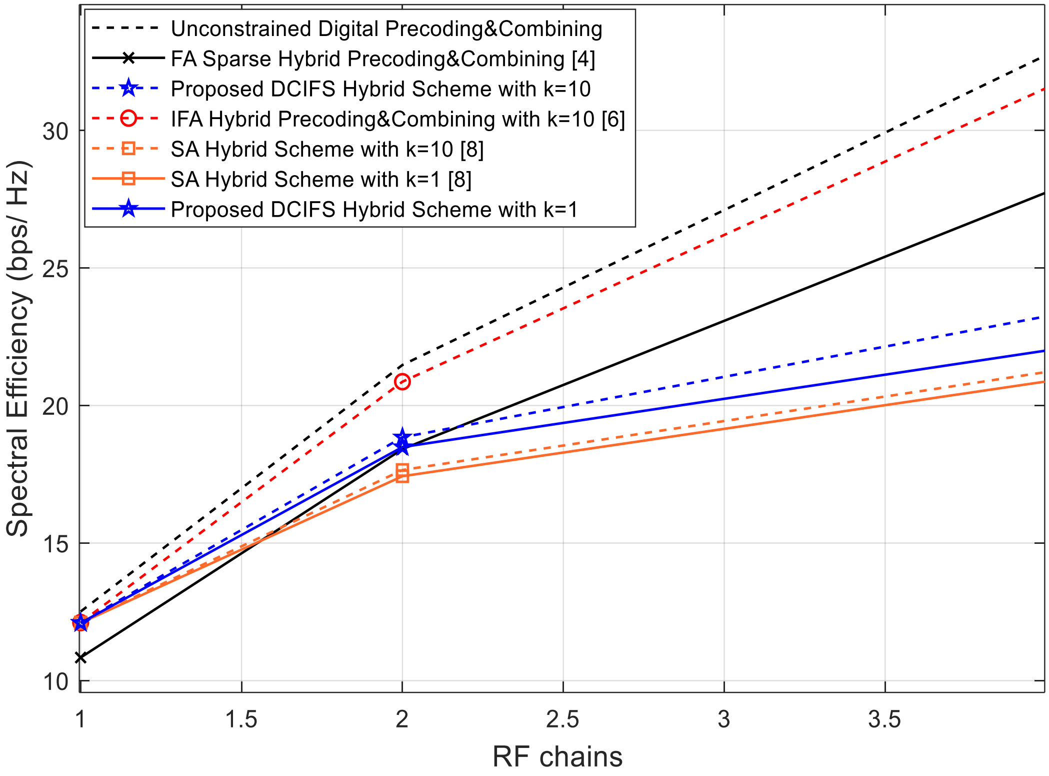

Figure 6. 8 Average spectral efficiency achieved by the proposed DCIFS hybrid precoding/combing design with different K compared to the FA sparse hybrid precoders/combiners [8], the optimal unconstrained digital precoders/combiners, IFA hybrid precoders/combiners [46] with K =10, and the SA hybrid precoding/combing design [78] with different K in 144 x 64 UPAs mm wave systems for SNR = 0 dB with $N_S = N_{tRF} = N_{rRF}$.

Fig. 6.9 evaluates the performance when the number of RF chains is greater than the number of data streams, where $N_S \in \{1,2,4\}$ and the SNR is fixed to 0 dB over the whole range of RF chains. Using the SA design in both the transmitter and receiver leads to a degradation in the overall performance of the proposed DCIFS hybrid precoding/combining design and the SA hybrid precoding/combining design compared to the results in Fig 6.4; the overall performance becomes worse when the interference between data streams increases for $N_S = 2,$ and 4. Similar to Fig 6.4, the performance of the proposed DCIFS hybrid precoding/combining design overlaps with the performance of the SA hybrid design for $N_S = 1$ and outperforms the SA design for any number of iterations K for $N_S = 2,$ and 4.

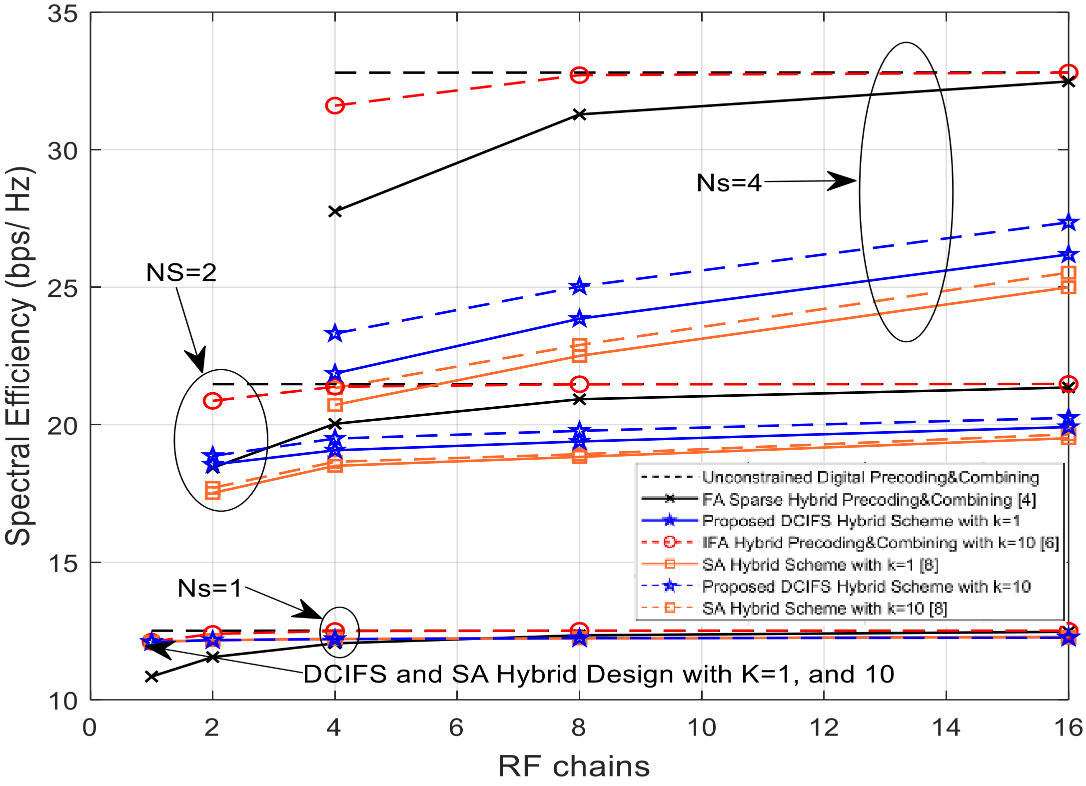

Figure 6. 9 Average spectral efficiency achieved by the proposed DCIFS hybrid precoding/combining design with different K compared to the FA sparse hybrid precoders/combiners [8], the optimal unconstrained digital precoders/combiners, IFA hybrid precoders/combiners [46] with K =10, and the SA hybrid precoding/combining design [78] with different K in 144 x 64 UPAs mm wave systems for SNR = 0 dB with $N_S \in \{1,2,4\}$ and different RF chains.

Fig. 6.10 shows the spectral efficiency achieved by the proposed DCIFS hybrid design, the FA sparse hybrid precoding/combining design [8], the optimal unconstrained digital precoding/combining design, the IFA hybrid precoding/combining design [46], and the SA hybrid [78] in a mm wave system for different BS antenna values with $N_r = 64$, *SNR* = 0 dB, $N_S = 2$ and $N_{tRF} = N_{rRF} = 4$. The maximum number of iterations K for the proposed DCIFS hybrid precoding/combining design and the SA hybrid precoding/combining design is equal to $1,$ and 10 for all BS antennas. In addition, the maximum number of iterations K for IFA hybrid precoding/combining design is 10. The performance of the proposed DCIFS and SA hybrid design is degraded compared to the results in Fig 6.5 and that is because we use the SA architecture in BS and MS. The performance of the proposed DCIFS hybrid design is much better than the SA hybrid design for any number of BS antennas and iterations. The proposed DCIFS hybrid design with *K*=1 outperforms the SA hybrid design with *K*=10 which means that our design performs better than the SA design with a very low number of iterations *K* resulting in a reduced computational complexity.

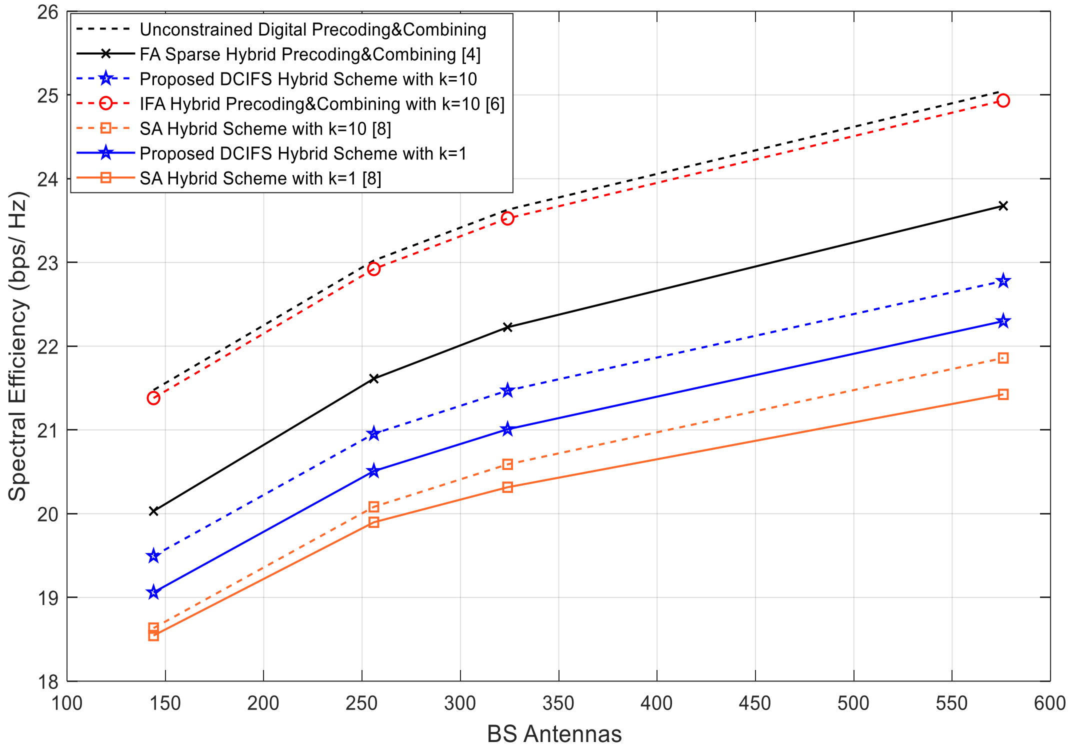

Figure 6. 10 Average spectral efficiency vs the number of BS antenna achieved by the proposed DCIFS hybrid precoders/combiners design with different K compared to the FA sparse hybrid precoders/combiners [8], the optimal unconstrained digital precoders/combiners, IFA hybrid precoders/combiners [46] with K =10, and the SA hybrid precoders/combiners design [78] with different K in UPAs mm wave systems for SNR = 0 dB with $N_r = 64$, $N_S = 2$ and $N_{tRF} = N_{rRF} = 4$

In Fig 6.11, we use the same parameters as in Fig 6.10, but we increase the number of data streams to 4. As we can see in Fig 6.11, similar to the previous figure, because we use the SA architecture in BS and MS, the performance of the proposed DCIFS and SA hybrid design is degraded compared to the results in Fig 6.6. The gain of the proposed DCIFS hybrid design over the SA hybrid design is very high for any number of BS antennas and iterations. Also, the proposed DCIFS hybrid design with K=1 outperforms the SA hybrid design with K=10 which shows the strength of our design against the SA hybrid design and that is because we take into consideration the matrix structure of the analog and baseband precoding and combining in the DCIFS hybrid design derivation.

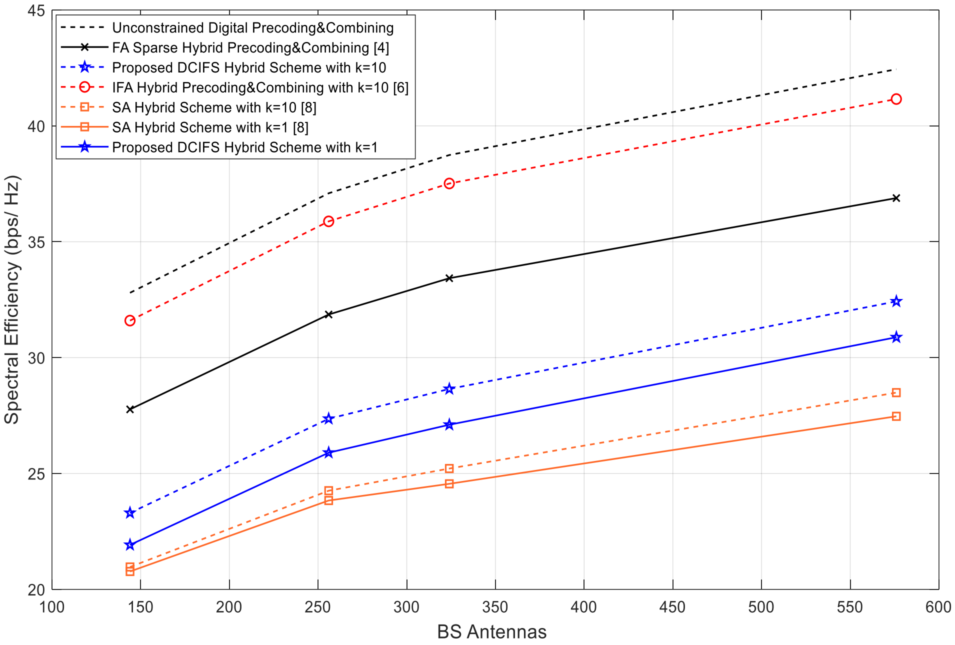

Figure 6. 11 Average spectral efficiency vs the number of BS antenna achieved by the proposed DCIFS hybrid precoders/combiners design with different K compared to the full array sparse hybrid precoders/combiners [8], the optimal unconstrained digital precoders/combiners, IFA hybrid precoders/combiners [46] with K =10, and the SA hybrid precoders/combiners design [78] with different K in UPAs mm wave systems for SNR = 0 dB with $N_r = 64$, $N_S = 4$ and $N_{tRF} = N_{rRF} = 4$

In conclusion, although we use the proposed DCIFS hybrid design in both transmitter and receiver, its performance is acceptable compared to the higher hardware complexity FA designs such as the sparse hybrid design and the IFA hybrid design. All full array hybrid design requires a higher hardware complexity in the BS and MS, and a higher number of phase shifters in the BS ad MS. The performance of the proposed DCIFS hybrid design is considerably better compared to the SA hybrid design with a small number of iterations and especially for a large number of BS antenna; taking advantage of the structure of the analog and baseband precoding/combing matrices in the proposed DCIFS hybrid design is the key point to achieve high performance and to outperform the SA hybrid design. The number of iterations should be 10 or less because after that the gain will be very small which is confirmed by our results that we did not include here in this thesis.

6.5 Summary

In this chapter, we developed an iterative hybrid precoding/combining design for mm wave MIMO systems with SA architecture. Considering the structure of the analog precoding/combining matrix in the SA architecture, we derived a solution that converts the analog precoding/combining of FA into SA directly. Two scenarios are studied with the suggested approach and compared with other existing FA and SA hybrid designs. The first one employs the proposed DCIFS hybrid precoding at the BS and the iterative FA hybrid combining at the MS, whereas the second scenario employs the proposed DCIFS hybrid precoding/combining at both the BS and the MS. Simulation results showed that the spectral efficiency of the DCIFS design approaches that obtained with the FA design and outperforms that obtained with the conventional SA design. Results also showed that the number of iterations suitable for the proposed hybrid design should be 10 or less. The hardware complexity of the suggested DCIFS hybrid design is the same as that of the conventional SA hybrid design and lower than that of the FA hybrid design. This indicates that the proposed DCIFS hybrid design is more suitable for future communication systems.

Chapter:7 Conclusions and Future Work

7.1 Summary

In this thesis, we proposed novel methods to minimize the bit error rate (BER) and achieve high spectral efficiency with lower computational and hardware complexity for 5G and beyond mm wave systems.

The first contribution has been to apply the SD and SDR algorithms to improve the performance of outdoor hybrid beamforming mm wave massive MIMO systems. Assuming the channel state information is known, the SDR algorithm can achieve near-ML performance for QPSK and better performance than ZF or MMSE for 16-QAM while requiring a lower complexity than SD at low to moderate SNRs even when the number of data streams or constellation size are large. The complexity of the SDR detector is higher compared to the linear ZF/MMSE detectors, but it is acceptable since it does not depend on the modulation order or SNR. Hence, when the SNR is low or moderate, SDR is well suited for applications that require an error performance that is superior to ZF or MMSE, and a complexity that is lower than sphere decoding. Moreover, for small number of data streams and low modulation order, the SD achieves the same bit error probability as the ML detector and with low complexity which is close to the complexity of the linear detection schemes such as ZF and MMSE.

In our second contribution, we have proposed a low complexity hybrid precoder/combiner design for single-user communication in mm wave systems. In our proposed design, there is no need to make any assumption on the antenna array geometry or for any other constraint, such as equal numbers of streams and RF chains. Assuming the channel state information is known, the proposed hybrid precoder/combiner approximates the optimal unconstrained digital ones. The computational complexity of our proposed solution is comparable to that of the HD-AM technique and close to that of the greedy hybrid design when the number of iterations K is reasonable, and it is much lower than the complexity of the sparse hybrid design. Our proposed solution can also be applied in all cases whereas the HD-AM technique can only be applied when the number of RF chains is equal to the number of data streams. The simulation results have shown that the proposed low complexity hybrid precoding/combining design improves the BER performance of simple ZF/MMSE detectors and considerably reduces the performance gap between these linear detectors and the high computational complexity methods such as the ML detector or Sphere Decoding. In addition, the spectral efficiency simulation results show that our proposed low complexity solution with a reasonable number of iterations K is similar to the HD-AM technique when the number of data streams is equal to the number of RF chains and outperforms the greedy or sparse hybrid design in all cases.

We extended our work in order to improve the performance of hybrid precoding/combining design by using gradient descent with momentum and Newton's Method. This is the third contribution of this thesis. The main difference between this proposed hybrid design and the previous hybrid design in our second contribution is that the gradient descent with momentum and Newton's Method can significantly improve the performance of the hybrid beamforming design and reduce the objective function with only a small number of iterations K. The proposed algorithm still has the same advantage as in our second contribution, which is that there is no need to make any assumption on the channel array geometry or channel structure while maintaining a low computational complexity. Simulation results verify that the two proposed hybrid precoding/combining schemes in our second and third contributions outperform the other popular schemes and achieves a much better performance in terms of the achievable spectral efficiency and BER with low complexity.

In the fourth contribution, we introduced an iterative hybrid precoding/combining design for mm wave systems with SA architecture. We derived a solution that converts the analog precoding/combining of FA into SA directly. Two scenarios are studied with the proposed approach and compared with other existing FA and SA hybrid designs. Simulation results showed that the spectral efficiency of the DCIFS design with small number of iterations approaches that obtained with the FA design and outperforms that obtained with the conventional SA design. The hardware complexity of the suggested DCIFS hybrid design is the same as that of the conventional SA hybrid design and much lower than that of the FA hybrid design.

7.2 Future Work

Several of the items explored in the thesis could be expanded upon. More specifically, possible future work could include the following:

1. Possible future work could explore and analyze the performance of the proposed hybrid designs in chapters 4, 5, and 6 with multiuser scenario where the multi streams interference problem appears.
2. Because of the large available bandwidth in mm wave systems, it will be interesting to extend the proposed hybrid designs to the multicarrier techniques such as orthogonal frequency division multiplexing (OFDM).
3. In chapter 6, the proposed hybrid design can be extended to a new low-complexity hybrid architecture (HA) for mm wave systems. The antennas at the transmitter/receiver in the HA

architecture are first divided into a set of subarrays equal to the number of radio frequency chains at the transmitter/receiver. The resulting set of subarrays is then divided into disjoint subsets known as groups. Finally, the antennas in each group are connected with a group of radio frequency chains in a manner similar to the connections in the FA architecture. For a future work, an efficient iterative hybrid design is still under study and analysis to solve the optimization problem of the hybrid precoding/combining for mm wave MIMO systems with HA architecture.

Appendix A: Numerical optimization schemes for minimization of a general function

In this Appendix, we present numerical optimization schemes for minimization of a general function. The optimal solution to minimize a general function f(x) over all input values x is typically denoted as x*. However, sometimes is not easy to find directly the optimal value x* especially for non-convex functions. In this section, we will introduce a gradient descent technique that finds points or input values which make the general function f(x) smaller and smaller. Then we select the point that is the most acceptable. The gradient descent or any numerical optimization scheme, which is used for minimizing a general function f(x) needs to follows these steps: first, we need an initial point x0 to start with, then we need to find the points x1, x2,… that make the function f(x) smaller. After that, we repeat the previous step until these points converge to a stationary point of f(x), i.e, a global minimum point for a convex function or local minimum point for a non-convex function. Notice that for a convex function, any initial point will lead to the global optimum. However, for non-convex functions, we need to try different initial points. In the next section, we will go into the details and see how the gradient descent works [74] [75].

A.1 Gradient descent

In gradient descent, there is a linear model of the function f, where we travel with a specific distance in the downward direction which is the negative gradient of the function f and then we return back to the function f [74] [75]. The process repeats until we reach the convergence. As shown in Fig. 2.7, we start with an initial point x0, then the gradient descent procedure uses the negative gradient of the cost function f to produces a sequence of points x1, x2,. . . , that minimizes the value of the cost function at each step and eventually reaches a stationary point of the cost function [74].

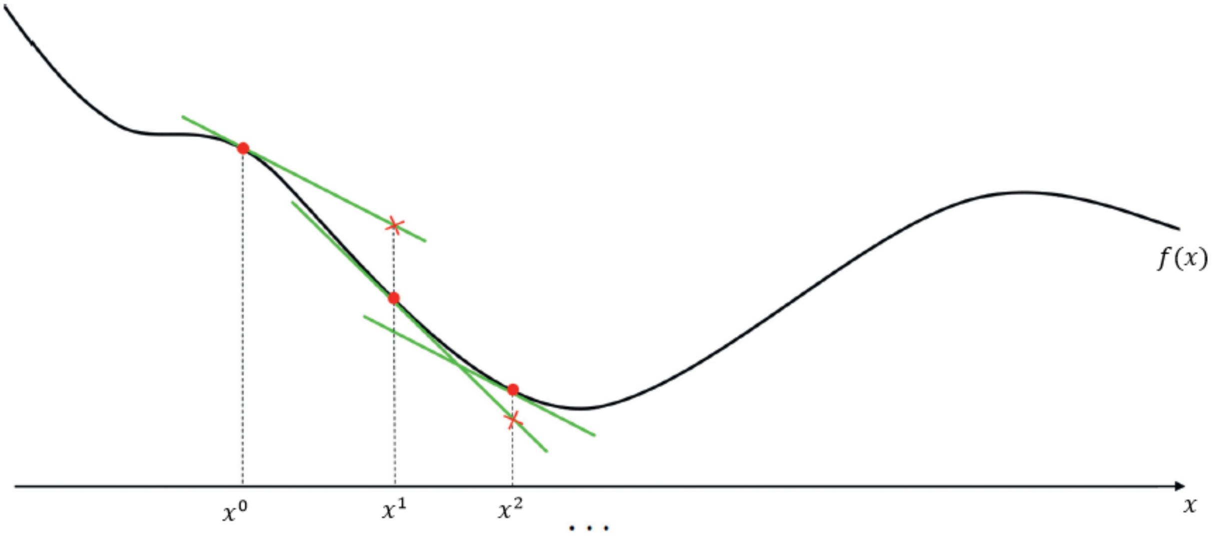

Figure A. 1 Travelling in the downward direction of a linear approximation in the gradient descent method [74].

To derive the gradient descent, first we need to use the first order Taylor series approximation at an initial point x^0 which is a tangent line passing through the point (x^0, $f(x^0)$) which is given by [74]

$$h(x) = f(x^0) + \nabla_f(x^0)^T(x - x^0) \tag{A.1}$$

We can get the downward direction by using the following solution [74]

$$h(x) = f(x^0) - \nabla_f(x^0)^T x^0 + \nabla_f(x^0)^T x \tag{A.2}$$

where the first two terms on the right hand side are considered as a constant with respect to x. Thus the direction x that minimizes the inner product $\nabla_f(X^0)^T x$ and reduces the value of the function h is $x = -\nabla_f(x^0)$ [74].

After descending in the direction of the negative gradient, the next point x^1 is derived as follows

$$x^1 = x^0 - \alpha_1 \nabla_f(x^0) \qquad \text{(A.3)}$$

where $\alpha_1 > 0$ is called a step length or a learning rate, that controls the distance of the negative gradient direction from the initial point x^0. This procedure is repeated by constructing the first order Taylor series approximation at x^1, traveling in its steepest descent direction $\nabla_f(x^1)$ and so on.

In general, this process is repeated with the kth step as follows [74]

$$x^k = x^{k-1} - \alpha_k \nabla_f(x^{k-1}) \qquad \text{(A.4)}$$

When $x^k = x^{k-1}$, that means that $\nabla_f(x^{k-1}) \approx 0_{NX1}$ which approximately satisfies the first order condition and x^k is the stationary point of f. Also, we can stop this procedure when a pre-specified number of iterations is completed or when the gradient of the function is smaller than a pre-defined threshold. Notice that the learning rate or the step length cannot be chosen too large or too small, because then the algorithm travels too far or too slowly, respectively at each step and will never converge. Algorithm A.1 shows the entire procedure of the gradient descent [74].

Algorithm A. 1: Gradient descent (with fixed step length) [74]

```
**Input**: differentiable function $f$, fixed step length α, and initial point $x^0$
$k$=1
**Repeat until stopping condition is met:**
$x^k = x^{k-1} - \alpha_k \nabla_f(x^{k-1})$
$k = k + 1$
```

We can input vectors instead of scalers in the objective function that maps the vectors to scalers, where $\mathrm{x} = [x_1,\ x_2 \dots\dots x_n]^{\mathrm{T}}$. By doing that, we can apply Multivariate Gradient descent and repeat the same process as before.

A.2 Adaptive Methods

From section A.1, choosing the learning rate α is not an easy task; it cannot be chosen too large or too small because the algorithm might oscillate and diverge, or make a small progress respectively. Thus, Second-order methods could determine α automatically and get rid of having to select a learning rate at all.

A.2.1 Newton's Method

From the Second-order Taylor expansion which is given by the following equation, where $\mathbf{H} = \nabla_f^2(\mathrm{x})$ to be the Hessian of f, which is a n x n matrix [74] [75]

$$f(\mathrm{x} + \varepsilon) = f(\mathrm{x}) + \varepsilon^{\mathrm{T}} \nabla_f(\mathrm{x}) + \frac{1}{2}\, \varepsilon^{\mathrm{T}}\, \mathbf{H}\, \varepsilon \qquad \text{(A.5)}$$

Newton's Method is established by setting the derivative of the Second-order Taylor expansion with respect to ε equal to zero and ignoring higher-order terms as follows

$$\nabla_f(\mathrm{x}) + \mathbf{H}\, \varepsilon = 0 \qquad \text{(A.6)}$$

In cases where the matrix $\mathbf{H}$ is invertible we may write the solution to the system in (A.6) as follows

$$\varepsilon = \mathbf{H}^{-1}\nabla_f(\mathrm{x}) \tag{A.7}$$

Thus, the equation of the gradient descent can add the Newton's Method and solve for the next steps as follows [74] [75]

$$\mathrm{x}^{\mathrm{k}} = \mathrm{x}^{k-1} - \mathbf{H}^{-1}\nabla_f(\mathrm{x}^{k-1}) \tag{A.8}$$

By using Newton's method, gradient descent converges in a much smaller number of steps than classical gradient descent. This is because it uses more precise second order information. However, this comes at the cost of having to solve the inversion of Hessian matrix. If the dimension of Hessian matrix **H** is small, then the gradient descent with Newton's Method is a good choice to make the objective function converge faster with fewer number of steps.

A.2.2 Preconditioning

Preconditioning is a good way to avoid the high computational complexity of the full Hessian. It computes only the inversion of its diagonal entries. This leads to following updated gradient descent with Newton's Method [74] [75]

$$\mathrm{x}^{\mathrm{k}} = \mathrm{x}^{k-1} - \alpha_k \, diag(\mathbf{H})^{-1}\nabla_f(\mathrm{x}^{k-1}) \tag{A.9}$$

We use the learning rate α with preconditioning because it does not use the full Newton's method.

A.3 Gradient descent with momentum

The problem in the gradient descent procedure is that the directions of the negative gradient tend to zig-zag before the convergence as shown in Fig. A.2 [74].

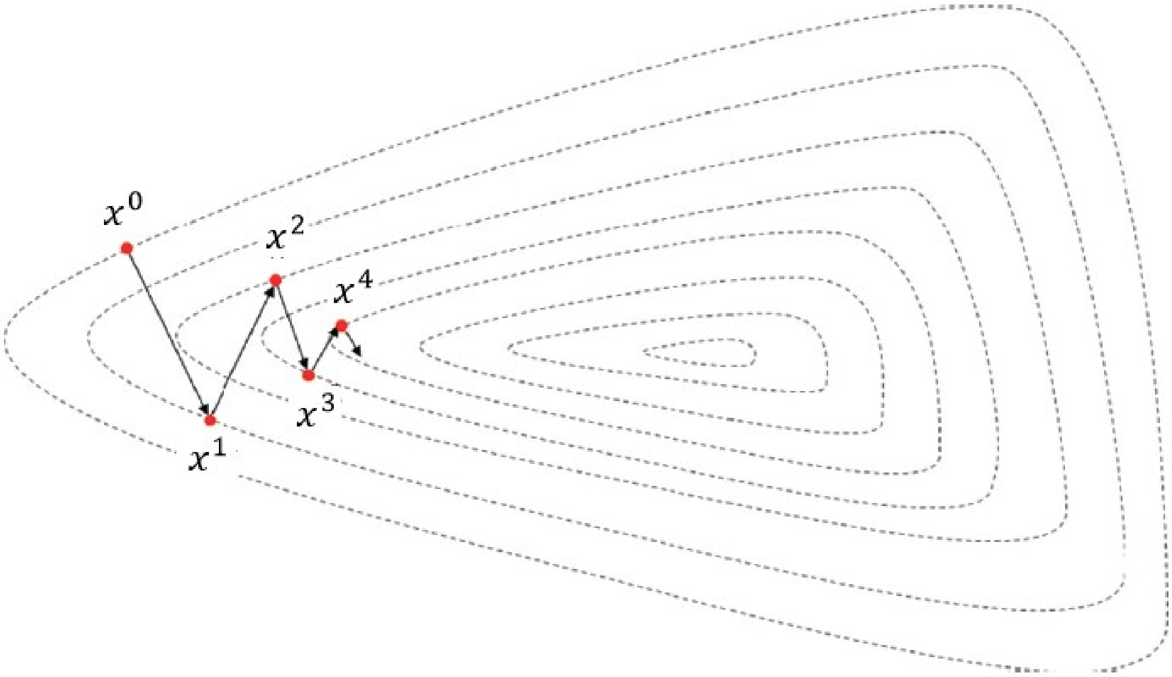

Figure A. 2. Gradient steps toward the minimum of a function in two dimensions [74].

The momentum term can be used to solve this problem and is designed to remove the effect of the zig-zag. The momentum term is added to the gradient of the function to correct it as follows [74]

$$\mathrm{x}^{k+1} = \mathrm{x}^{k} - \alpha_{k+1}\mathrm{Z}_{k} \qquad \text{(A.10)}$$

$$\mathrm{Z}_{k} = \beta_{k}\mathrm{Z}_{k-1} + (1-\beta_{k})\nabla_{f}(\mathrm{x}^{k})$$

where Z_k is another direction and is different from the direction of the gradient. Notice that $0 < \beta < 1$ can be adjusted at each iteration. Large β amounts to a long-range average, whereas small β amounts to only a slight correction relative to a gradient method. Fig. A.3 shows the gradient descent scheme with the momentum term or memory term where we can see that this solution averages out the zig-zagging problem which occurred in the original gradient descent procedure [74].

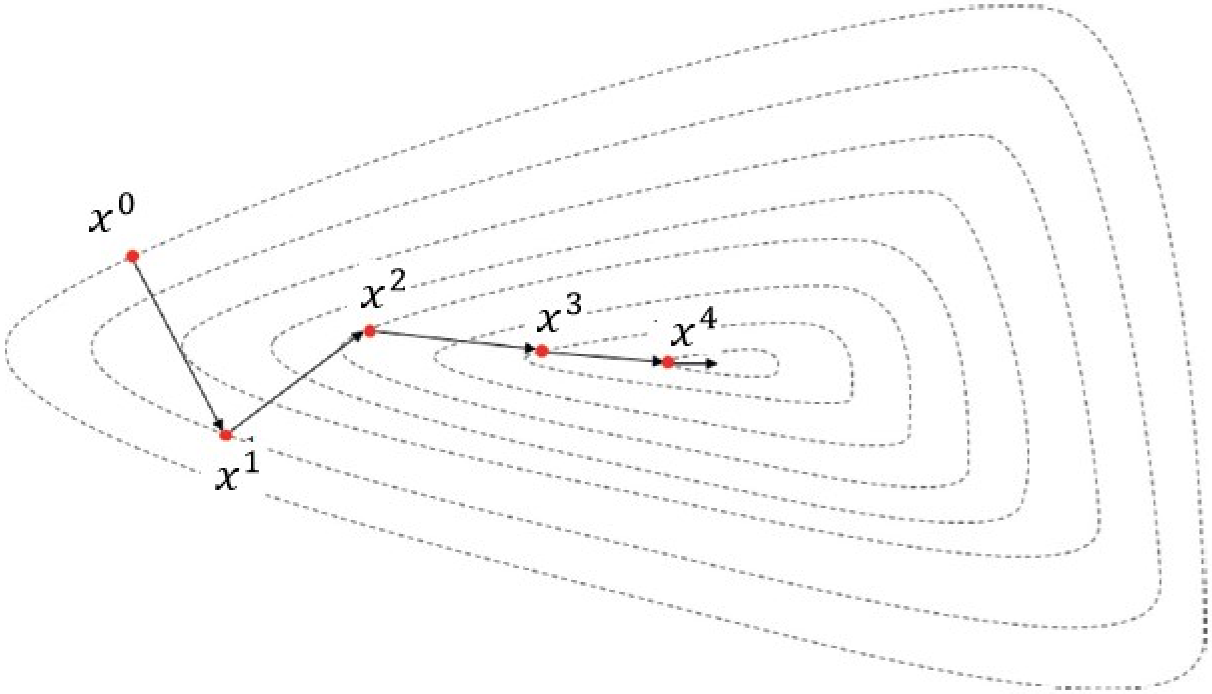

Figure A. 3. Shows the momentum-corrected (averaged zig-zagging) gradient descent steps toward the minimum of the same function shown in Fig A.2 [74].

In the momentum method, the first couple of iterations will provide a crude moving average over the past gradients because we do not have enough values yet to average over; the solution is to use what is called the bias-corrected version as follows [74]

$$\mathrm{x}^{k+1} = \mathrm{x}^{k} - \alpha_{k+1}\mathrm{Z}_{k} \tag{A.11}$$

$$\mathrm{Z}_{k} = \beta_{k}\mathrm{Z}_{k-1} + (1-\beta_{k}\,)\nabla_{f}(\mathrm{x}^{k}))/(1-\beta_{k}^{k})$$

Notice that with large values of k, β to the power of k will be close to zero, thus not changing the values of Z_k at all.

Appendix B: Compressive sensing problem

The orthogonal matching pursuit (OMP) is used to solve the Compressive sensing problem which is given as follows [76]

$$\mathrm{y}_{mx1} = \mathbf{A}_{mxn}\,\mathrm{x}_{nx1}$$

where x is compressively sensed by the compressive sensing matrix $\mathbf{A}$, and m is much smaller than n, $m \ll n$.

Algorithm B.1 illustrates the OMP for recovery in compressive sensing. OMP starts by finding a column of **A** along which the measurements y has the maximum projection. It then appends the selected column vector to the **Λ** matrix. After that, the signal vector x is updated and calculated using the least squares solution. After the first iteration, the algorithm searches for the column of **A** with maximum correlation with the residual r and repeat the same process as the first iteration. The process continues until a stopping criterion is met or the number of iterations reaches a limit. Finally the sparse signal vector x is returned.

Algorithm B. 1: Orthogonal matching pursuit (OMP) algorithm for compressive sensing recovery [76]

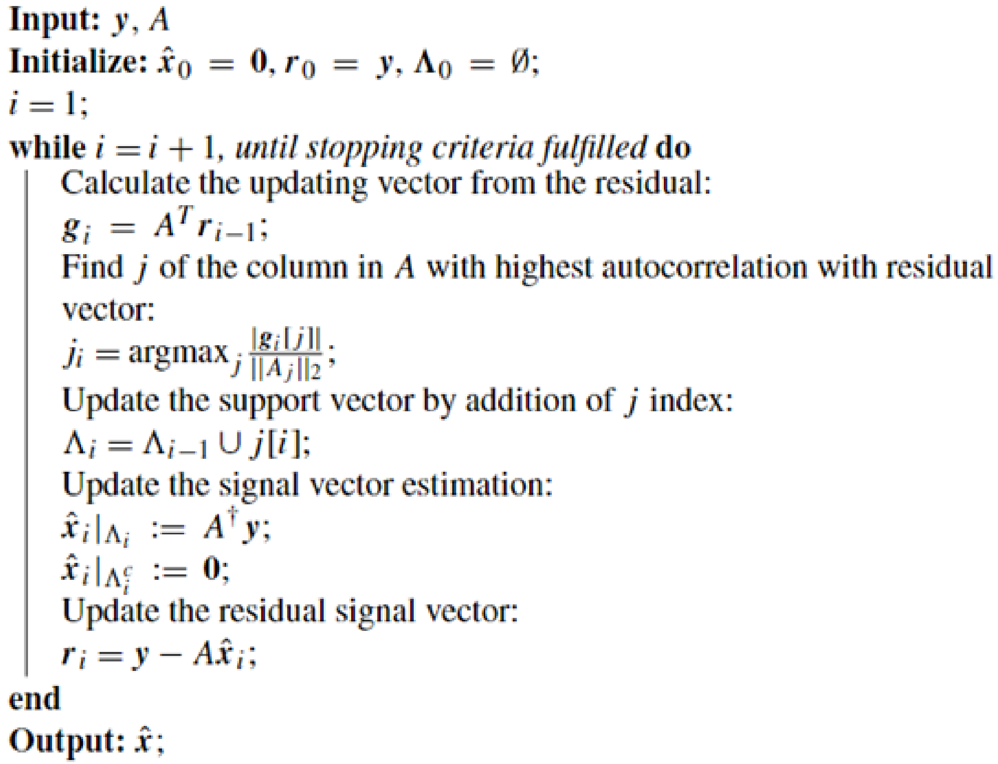

```
**Input:** $y, A$
**Initialize:** $\hat{x}_0 = \mathbf{0}, r_0 = y, \Lambda_0 = \emptyset$;
$i = 1$;
**while** $i = i + 1$, *until stopping criteria fulfilled* **do**
    Calculate the updating vector from the residual:
    $g_i = A^T r_{i-1}$;
    Find $j$ of the column in $A$ with highest autocorrelation with residual
    vector:
    $j_i = \text{argmax}_j \frac{|g_i[j]|}{||A_j||_2}$;
    Update the support vector by addition of $j$ index:
    $\Lambda_i = \Lambda_{i-1} \cup j[i]$;
    Update the signal vector estimation:
    $\hat{x}_i|_{\Lambda_i} := A^\dagger y$;
    $\hat{x}_i|_{\Lambda_i^c} := \mathbf{0}$;
    Update the residual signal vector:
    $r_i = y - A\hat{x}_i$;
**end**
**Output:** $\hat{x}$;
```

References

[1] Y. S. Cho, J. Kim, W. Y. Yang, and C. G. Kang, MIMO-OFDM wireless communications with MATLAB. John Wiley & Sons, 2010.

[2] L. Lu, G. Y. Li, A. L. Swindlehurst, A. Ashikhmin, and R. Zhang, “An overview of massive MIMO: Benefits and challenges,” IEEE J. Sel. Top. Signal Process., vol. 8, no. 5, pp. 742–758, 2014.

[3] E. G. Larsson, O. Edfors, F. Tufvesson, and T. L. Marzetta, “Massive MIMO for next generation wireless systems,” IEEE Commun. Mag., vol. 52, no. 2, pp. 186–195, 2014.

[4] T. E. Bogale and L. B. Le, “Massive MIMO and mmWave for 5G wireless HetNet: Potential benefits and challenges,” IEEE Veh. Technol. Mag., vol. 11, no. 1, pp. 64–75, 2016.

[5] T. S. Rappaport et al., “Millimeter wave mobile communications for 5G cellular: It will work!,” IEEE Access, vol. 1, pp. 335–349, 2013.

[6] J. G. Andrews, T. Bai, M. N. Kulkarni, A. Alkhateeb, A. K. Gupta, and R. W. Heath, “Modeling and analyzing millimeter wave cellular systems,” IEEE Trans. Commun., vol. 65, no. 1, pp. 403–430, 2016.

[7] G. R. MacCartney, M. K. Samimi, and T. S. Rappaport, “Exploiting directionality for millimeter-wave wireless system improvement,” in 2015 IEEE international conference on communications (ICC), 2015, pp. 2416–2422.

[8] O. El Ayach, S. Rajagopal, S. Abu-Surra, Z. Pi, and R. W. Heath, “Spatially sparse precoding in millimeter wave MIMO systems,” IEEE Trans. Wirel. Commun., vol. 13, no. 3, pp. 1499–1513, 2014.

[9] A. Alkhateeb, O. El Ayach, G. Leus, and R. W. Heath, “Channel estimation and hybrid precoding for millimeter wave cellular systems,” IEEE J. Sel. Top. Signal Process., vol. 8, no. 5, pp. 831–846, 2014.

[10] W. Ahmad, H. Zhang, Y. Chen, and N. Iqbal, “Full Digital Transmit Beamforming with Low RF Complexity for Large-scale mmWave MIMO system,” in ICC 2020-2020 IEEE International Conference on Communications (ICC), 2020, pp. 1–6.

[11] W. Roh et al., “Millimeter-wave beamforming as an enabling technology for 5G cellular communications: Theoretical feasibility and prototype results,” IEEE Commun. Mag., vol. 52, no. 2, pp. 106–113, 2014.

[12] J. Nsenga, A. Bourdoux, and F. Horlin, “Mixed analog/digital beamforming for 60 GHz MIMO frequency selective channels,” in 2010 IEEE International Conference on Communications, 2010, pp. 1–6.

[13] F. Gholam, J. Vía, and I. Santamaria, “Beamforming design for simplified analog antenna combining architectures,” IEEE Trans. Veh. Technol., vol. 60, no. 5, pp. 2373–2378, 2011.

[14] Z. Pi, “Optimal transmitter beamforming with per-antenna power constraints,” in 2012 IEEE International Conference on Communications (ICC), 2012, pp. 3779–3784.

[15] X. Zhang, A. F. Molisch, and S.-Y. Kung, “Variable-phase-shift-based RF-baseband codesign for MIMO antenna selection,” IEEE Trans. Signal Process., vol. 53, no. 11, pp. 4091–4103, 2005.

[16] V. Venkateswaran and A.-J. van der Veen, “Analog beamforming in MIMO communications with phase shift networks and online channel estimation,” IEEE Trans. Signal Process., vol. 58, no. 8, pp. 4131–4143, 2010.

[17] L. Fan, S. Jin, C.-K. Wen, and H. Zhang, “Uplink achievable rate for massive MIMO systems with low-resolution ADC,” IEEE Commun. Lett., vol. 19, no. 12, pp. 2186–2189, 2015.

[18] Q. Hou, R. Wang, E. Liu, and D. Yan, “Hybrid precoding design for MIMO system with one-bit ADC receivers,” IEEE Access, vol. 6, pp. 48478–48488, 2018.

[19] J. Mo, A. Alkhateeb, S. Abu-Surra, and R. W. Heath, “Hybrid architectures with few-bit ADC receivers: Achievable rates and energy-rate tradeoffs,” IEEE Trans. Wirel. Commun., vol. 16, no. 4, pp. 2274–2287, 2017.

[20] J. A. Tropp, A. C. Gilbert, and M. J. Strauss, “Algorithms for simultaneous sparse approximation. Part I: Greedy pursuit,” Signal Process., vol. 86, no. 3, pp. 572–588, 2006.

[21] K. Engan, S. O. Aase, and J. H. Husoy, “Method of optimal directions for frame design,” in 1999 IEEE International Conference on Acoustics, Speech, and Signal Processing. Proceedings. ICASSP99 (Cat. No. 99CH36258), 1999, vol. 5, pp. 2443–2446.

[22] C. Rusu, R. Méndez-Rial, N. González-Prelcicy, and R. W. Heath, “Low complexity hybrid sparse precoding and combining in millimeter wave MIMO systems,” in 2015 IEEE International Conference on Communications (ICC), 2015, pp. 1340–1345.

[23] M. Kim and Y. H. Lee, “MSE-based hybrid RF/baseband processing for millimeter-wave communication systems in MIMO interference channels,” IEEE Trans. Veh. Technol., vol. 64, no. 6, pp. 2714–2720, 2014.

[24] J. Singh and S. Ramakrishna, “On the feasibility of codebook-based beamforming in millimeter wave systems with multiple antenna arrays,” IEEE Trans. Wirel. Commun., vol. 14, no. 5, pp. 2670–2683, 2015.

[25] C.-E. Chen, “An iterative hybrid transceiver design algorithm for millimeter wave MIMO systems,” IEEE Wirel. Commun. Lett., vol. 4, no. 3, pp. 285–288, 2015.

[26] R. Mendez-Rial, C. Rusu, N. González-Prelcic, and R. W. Heath, “Dictionary-free hybrid precoders and combiners for mmWave MIMO systems,” in 2015 IEEE 16th International Workshop on Signal Processing Advances in Wireless Communications (SPAWC), 2015, pp. 151–155.

[27] W. Ni, X. Dong, and W.-S. Lu, “Near-optimal hybrid processing for massive MIMO systems via matrix decomposition,” IEEE Trans. Signal Process., vol. 65, no. 15, pp. 3922–3933, 2017.

[28] C. Rusu, R. Mendez-Rial, N. Gonzalez-Prelcic, and R. W. Heath, “Low complexity hybrid precoding strategies for millimeter wave communication systems,” IEEE Trans. Wirel. Commun., vol. 15, no. 12, pp. 8380–8393, 2016.

[29] X. Yu, J.-C. Shen, J. Zhang, and K. B. Letaief, “Alternating minimization algorithms for hybrid precoding in millimeter wave MIMO systems,” IEEE J. Sel. Top. Signal Process., vol. 10, no. 3, pp. 485–500, 2016.

[30] F. Sohrabi and W. Yu, “Hybrid digital and analog beamforming design for large-scale antenna arrays,” IEEE J. Sel. Top. Signal Process., vol. 10, no. 3, pp. 501–513, 2016.

[31] J.-C. Chen, “Gradient projection-based alternating minimization algorithm for designing hybrid beamforming in millimeter-wave MIMO systems,” IEEE Commun. Lett., vol. 23, no. 1, pp. 112–115, 2018.

[32] J. Jin, Y. R. Zheng, W. Chen, and C. Xiao, “Hybrid precoding for millimeter wave MIMO systems: A matrix factorization approach,” IEEE Trans. Wirel. Commun., vol. 17, no. 5, pp. 3327–3339, 2018.

[33] R. Zhang, W. Zou, Y. Wang, and M. Cui, “Hybrid precoder and combiner design for single-user mmWave MIMO systems,” IEEE Access, vol. 7, pp. 63818–63828, 2019.

[34] A. Alkhateeb, G. Leus, and R. W. Heath, “Limited feedback hybrid precoding for multi-user millimeter wave systems,” IEEE Trans. Wirel. Commun., vol. 14, no. 11, pp. 6481–6494, 2015.

[35] W. Ni and X. Dong, “Hybrid block diagonalization for massive multiuser MIMO systems,” IEEE Trans. Commun., vol. 64, no. 1, pp. 201–211, 2015.

[36] D. H. Nguyen, L. B. Le, T. Le-Ngoc, and R. W. Heath, “Hybrid MMSE precoding and combining designs for mmWave multiuser systems,” IEEE Access, vol. 5, pp. 19167–19181, 2017.

[37] R. A. Stirling-Gallacher and M. S. Rahman, “Linear MU-MIMO pre-coding algorithms for a millimeter wave communication system using hybrid beam-forming,” in 2014 IEEE International Conference on Communications (ICC), 2014, pp. 5449–5454.

[38] S. Han, I. Chih-Lin, Z. Xu, and C. Rowell, “Large-scale antenna systems with hybrid analog and digital beamforming for millimeter wave 5G,” IEEE Commun. Mag., vol. 53, no. 1, pp. 186–194, 2015.

[39] J. Du, W. Xu, H. Shen, X. Dong, and C. Zhao, “Hybrid precoding architecture for massive multiuser MIMO with dissipation: Sub-connected or fully connected structures?,” IEEE Trans. Wirel. Commun., vol. 17, no. 8, pp. 5465–5479, 2018.

[40] X. Gao, L. Dai, S. Han, I. Chih-Lin, and R. W. Heath, “Energy-efficient hybrid analog and digital precoding for mmWave MIMO systems with large antenna arrays,” IEEE J. Sel. Areas Commun., vol. 34, no. 4, pp. 998–1009, 2016.

[41] R. Magueta, D. Castanheira, A. Silva, R. Dinis, and A. Gameiro, “Hybrid multi-user equalizer for massive MIMO millimeter-wave dynamic subconnected architecture,” IEEE Access, vol. 7, pp. 79017–79029, 2019.

[42] S. Park, A. Alkhateeb, and R. W. Heath, “Dynamic subarrays for hybrid precoding in wideband mmWave MIMO systems,” IEEE Trans. Wirel. Commun., vol. 16, no. 5, pp. 2907–2920, 2017.

[43] D. Castanheira, P. Lopes, A. Silva, and A. Gameiro, “Hybrid beamforming designs for massive MIMO millimeter-wave heterogeneous systems,” IEEE Access, vol. 5, pp. 21806–21817, 2017.

[44] A. Adhikary, J. Nam, J.-Y. Ahn, and G. Caire, “Joint spatial division and multiplexing—The large-scale array regime,” IEEE Trans. Inf. Theory, vol. 59, no. 10, pp. 6441–6463, 2013.

[45] A. F. Molisch et al., “Hybrid beamforming for massive MIMO: A survey,” IEEE Commun. Mag., vol. 55, no. 9, pp. 134–141, 2017.

[46] M. Alouzi, F. Chan, and C. D’Amours, “Low Complexity Hybrid Precoding and Combining for Millimeter Wave Systems,” IEEE Access, vol. 9, pp. 95911–95924, 2021.

[47] M. Alouzi, F. Chan, and C. D’Amours, “Sphere decoding for millimeter wave massive MIMO,” in 2019 IEEE 90th Vehicular Technology Conference (VTC2019-Fall), 2019, pp. 1–6.

[48] M. Alouzi, F. Chan, and C. D’Amours, “Semidefinite Relaxation for Millimeter Wave Massive MIMO Detection,” in 2020 11th IEEE Annual Information Technology, Electronics and Mobile Communication Conference (IEMCON), 2020, pp. 0734–0739.

[49] M. Alouzi, F Al-kamali, F. Chan, and C. D’Amours, “Direct Conversion of Hybrid Precoding and Combining from Full Array Architecture to Subarray Architecture for mmWave MIMO Systems,” IEEE Access, vol. 11, pp. 35457-35468, 2023.

[50] M. Alouzi, F. Chan, and C. D'Amours, "Low Complexity Hybrid Precoding and Combining with Momentum Gradient Descent and Newton's Method for Millimeter Wave Systems," submitted to IEEE Access.

[51] M. A. Khalighi, K. Raoof, and G. Jourdain, "Capacity of wireless communication systems employing antenna arrays, a tutorial study," Wirel. Pers. Commun., vol. 23, no. 3, pp. 321–352, 2002.

[52] M. Viswanathan, "Characterizing a MIMO channel–Channel State Information (CSI) and Condition number." GaussianWaves, 2014.

[53] A. Wiesel, Y. C. Eldar, and S. Shamai, "Semidefinite relaxation for detection of 16-QAM signaling in MIMO channels," IEEE Signal Process. Lett., vol. 12, no. 9, pp. 653–656, 2005.

[54] Y. Yang, C. Zhao, P. Zhou, and W. Xu, "MIMO detection of 16-QAM signaling based on semidefinite relaxation," IEEE Signal Process. Lett., vol. 14, no. 11, pp. 797–800, 2007.

[55] N. Souto, M. Ribeiro, and P. Sebastião, "Semidefinite relaxations for MIMO transmissions with high-order QAM constellations," IEEE Signal Process. Lett., vol. 23, no. 7, pp. 984–988, 2016.

[56] J. F. Sturm, "Using SeDuMi 1.02, a MATLAB toolbox for optimization over symmetric cones," Optim. Methods Softw., vol. 11, no. 1–4, pp. 625–653, 1999.

[57] B. Hassibi and H. Vikalo, "On the sphere-decoding algorithm I. Expected complexity," IEEE Trans. Signal Process., vol. 53, no. 8, pp. 2806–2818, 2005.

[58] A. K. Sah and A. K. Chaturvedi, "An MMP-based approach for detection in large MIMO systems using sphere decoding," IEEE Wirel. Commun. Lett., vol. 6, no. 2, pp. 158–161, 2016.

[59] M. Karthikeyan and D. Saraswady, "Sphere decoding using threshold based Schnorr-Euchner enumeration in MIMO system," in 2014 International Conference on Recent Trends in Information Technology, 2014, pp. 1–4.

[60] S. Mrinalee, H. P. Garg, G. Mathur, and R. P. Yadav, "Improved radius selection in sphere decoder for MIMO System," in 2014 International Conference on Computing for Sustainable Global Development (INDIACom), 2014, pp. 161–165.

[61] G. J. Foschini and M. J. Gans, "On limits of wireless communications in a fading environment when using multiple antennas," Wirel. Pers. Commun., vol. 6, no. 3, pp. 311–335, 1998.

[62] T. L. Marzetta, "Noncooperative cellular wireless with unlimited numbers of base station antennas," IEEE Trans. Wirel. Commun., vol. 9, no. 11, pp. 3590–3600, 2010.

[63] K. Hosseini, J. Hoydis, S. Ten Brink, and M. Debbah, "Massive MIMO and small cells: How to densify heterogeneous networks," in 2013 IEEE international conference on communications (ICC), 2013, pp. 5442–5447.

[64] H. Q. Ngo, Massive MIMO: Fundamentals and system designs, vol. 1642. Linköping University Electronic Press, 2015.

[65] F. A. de Figueiredo, J. P. Miranda, F. L. Figueiredo, and F. A. Cardoso, "Uplink performance evaluation of massive MU-MIMO systems," ArXiv Prepr. ArXiv150302192, 2015.

[66] R. W. Heath, N. Gonzalez-Prelcic, S. Rangan, W. Roh, and A. M. Sayeed, "An overview of signal processing techniques for millimeter wave MIMO systems," IEEE J. Sel. Top. Signal Process., vol. 10, no. 3, pp. 436–453, 2016.

[67] J. Lee, J. Liang, H.-K. Kwon, and M.-D. Kim, "Site-specific path loss characteristics with directional antenna measurements at 28 GHz in urban street grid environments," in 2015 IEEE 26th Annual International Symposium on Personal, Indoor, and Mobile Radio Communications (PIMRC), 2015, pp. 186–190.

[68] S. Sun et al., "Propagation path loss models for 5G urban micro-and macro-cellular scenarios," in 2016 IEEE 83rd Vehicular Technology Conference (VTC Spring), 2016, pp. 1–6.

[69] G. R. MacCartney, M. K. Samimi, and T. S. Rappaport, "Omnidirectional path loss models in New York City at 28 GHz and 73 GHz," in 2014 IEEE 25th Annual International Symposium on Personal, Indoor, and Mobile Radio Communication (PIMRC), 2014, pp. 227–231.

[70] A. L. Swindlehurst, E. Ayanoglu, P. Heydari, and F. Capolino, "Millimeter-wave massive MIMO: The next wireless revolution?," IEEE Commun. Mag., vol. 52, no. 9, pp. 56–62, 2014.

[71] Y. Niu, Y. Li, D. Jin, L. Su, and A. V. Vasilakos, "A survey of millimeter wave communications (mmWave) for 5G: opportunities and challenges," Wirel. Netw., vol. 21, no. 8, pp. 2657–2676, 2015.

[72] S. Gimenez et al., "Performance evaluation of analog beamforming with hardware impairments for mmW massive MIMO communication in an urban scenario," Sensors, vol. 16, no. 10, p. 1555, 2016.

[73] S. Mumtaz, J. Rodriguez, and L. Dai, MmWave massive MIMO: a paradigm for 5G. Academic Press, 2016.

[74] J. Watt, R. Borhani, and A. K. Katsaggelos, "Machine learning refined," 2019.

[75] A. Burkov, The hundred-page machine learning book, vol. 1. Andriy Burkov Canada, 2019.

[76] M. Khosravy, N. Gupta, N. Patel, and C. A. Duque, “Recovery in compressive sensing: a review,” Compressive Sens. Healthc., pp. 25–42, 2020.

[77] S. Park and A. Alkhateeb, “Dynamic subarrays for hybrid precoding in wideband mmWave MIMO systems,” IEEE Transactions on Wireless Communications, vol. 16, no. 5, pp. 2907–2920, 2017.

[78] F. Al-Kamali and C. D’amours, "Low-Complexity Hybrid Precoding for Subarray Architecture mmWave MIMO Systems," in IEEE Access, vol. 10, pp. 74921-74930, 2022.

[79] S. He, C. Qi, Y. Wu and Y. Huang, "Energy-Efficient Transceiver Design for Hybrid Sub-Array Architecture MIMO Systems," in IEEE Access, vol. 4, pp. 9895-9905, 2016.

[80] Z. Zhang, X. Wu, and D. Liu, “Joint precoding and combining design for hybrid beamforming systems with subconnected structure,” IEEE Syst. J., vol. 14, no. 1, pp. 184–195, Mar. 2020

[81] Z. Ni, J. A. Zhang, K. Yang, F. Gao and J. An, "Low-Complexity Subarray-Based RF Precoding for Wideband Multiuser Millimeter Wave Systems," in IEEE Transactions on Vehicular Technology, vol. 69, no. 7, pp. 8028-8033, July 2020.

[82] L. Yan, C. Han, and J. Yuan, “A Dynamic Array of Sub-Array Architecture for Hybrid Precoding in the Millimeter Wave and Terahertz Bands,” in Proc. of IEEE ICC workshops., May. 2019.

[83] J. Jiang, Y. Yuan and L. Zhen, "Multi-User Hybrid Precoding for Dynamic Subarrays in mmWave Massive MIMO Systems," in IEEE Access, vol. 7, pp. 101718-101728, 2019.

[84] K. B. Dsouza, K. N. R. S. V. Prasad and V. K. Bhargava, "Hybrid Precoding With Partially Connected Structure for Millimeter Wave Massive MIMO OFDM: A Parallel Framework and Feasibility Analysis," in IEEE Transactions on Wireless Communications, vol. 17, no. 12, pp. 8108-8122, Dec. 2018.

[85] W. Huang, Z. Lu, Y. Huang and L. Yang, "Hybrid Precoding for Single Carrier Wideband Multi-Subarray Millimeter Wave Systems," in *IEEE Wireless Communications Letters*, vol. 8, no. 2, pp. 484-487, April 2019.

[86] Z. Ni, J. A. Zhang, K. Yang, F. Gao and J. An, "Low-Complexity Subarray-Based RF Precoding for Wideband Multiuser Millimeter Wave Systems," in IEEE Transactions on Vehicular Technology, vol. 69, no. 7, pp. 8028-8033, July 2020.

[87] P. H. Schönemann, “A generalized solution of the orthogonal Procrustes problem,” Psychometrika, vol. 31, no. 1, pp. 1–10, Mar. 1966